THESIS FOR THE DEGREE OF LICENTIATE OF PHILOSOPHY

A quantum-chemical study to the magnetic characteristics of methanol and its applications in astronomy

BOY LANKHAAR

CHALMERS
UNIVERSITY OF TECHNOLOGY

DEPARTMENT OF SPACE, EARTH AND ENVIRONMENT
CHALMERS UNIVERSITY OF TECHNOLOGY
GOTHENBURG, SWEDEN 2018

A quantum-chemical study to the magnetic characteristics of methanol and its applications in astronomy
BOY LANKHAAR

Division of Astronomy & Plasma Physics
Department of Space, Earth and Environment
Chalmers University of Technology
SE–412 96 Gothenburg, Sweden
Phone: +46 (0)31–772 10 00

Contact information:
Boy Lankhaar
Chalmers University of Technology
Onsala Space Observatory
SE–439 92 Råö, Sweden

Phone: +46 (0)31–772 55 42
Email: boy.lankhaar@chalmers.se

Printed by Chalmers Reproservice
Chalmers University of Technology
Gothenburg, Sweden 2018

A quantum-chemical study to the magnetic characteristics of methanol and its applications in astronomy

BOY LANKHAAR
Department of Space, Earth and Environment
Chalmers University of Technology

ABSTRACT

Magnetic fields play an important role during star formation. Direct magnetic field strength observations have proven specifically challenging in the dynamic protostellar phase. Because of their occurrence in the densest parts of star forming regions, masers, through polarization observations, are the main source of magnetic field strength and morphology measurements around protostars. Of all maser species, methanol is one of the strongest and most abundant tracers of gas around high-mass protostellar disks and in outflows. However, because experimental determination of the magnetic characteristics of methanol has remained unsuccessful, a magnetic field strength analysis of these regions could hitherto not be performed. In this thesis, we present quantum-chemical calculations of the magnetic characteristics of methanol. We present the parameters characterizing the internal magnetic interactions: the hyperfine structure, as well as the parameters characterizing the interaction of methanol with an external magnetic field. We use these parameters in re-analyzing methanol maser polarization observations. With these calculations, we can confirm the presence of dynamically important magnetic fields around protostars.

Keywords: magnetic field - stars: formation - stars: massive - masers - polarization

RESEARCH CONTRIBUTIONS

This thesis is based on the work comprised of the following contributions:

I Lankhaar, B., Groenenboom, G.C., van der Avoird, 2016. Hyperfine interactions and internal rotation in methanol. *Journal of Chemical Physics* 145, 244301, 2016. doi: 10.1063/1.4972004

II Lankhaar, B., Vlemmings, W.H.T., Surcis, G., van Langevelde, H.J., Groenenboom, G.C., van der Avoid, A., 2018. Characterization of methanol as a magnetic field tracer in star-forming regions. *Nature Astronomy* 2, 145–150. https://doi.org/10.1038/s41550-017-0341-8

The author contributed also to the following publications (not appended):

I. Dall'Olio, D., Vlemmings, W.H.T., Surcis, G., Beuther, H., Lankhaar, B., Persson, M.V., Richards, A.M.S., Varenius, E., 2017. Methanol masers reveal the magnetic field of the high-mass protostar IRAS 18089-1732. *Astronomy and Astrophysics* 607, A111. doi: 10.1051/0004-6361/201731297

II. Vlemmings, W.H.T., Khouri, T., O'Gorman, E., de Beck, E., Humphreys, E., Lankhaar, B., Maercker, M., Olofsson, H., Ramstedt, S., Tafoya, D., Takigawa, A., 2017. The shock-heated atmosphere of an asymptotic giant branch star resolved by ALMA. *Nature Astronomy* 1, 848-853. doi: 10.1038/s41550-017-0288-9

ACKNOWLEDGMENTS

This thesis is the summary of two years of work in science. In this time, I have and have had a lot to be thankful for.
First of all, I should thank my supervisor, Wouter Vlemmings, for giving me the opportunity to work in the amazing field of astronomy. I guess it has been a leap of faith to employ and supervise somebody with a scientific background so different from your own. But our discussions and collaboration have sure been educational and fruitful to me. I have a great respect for your strong grip on astrophysics and your ability to recognize the physicality behind complex mathematical equations. Besides my current supervisor, I am still endebted a lot to my previous supervisors, Ad van der Avoird and Gerrit Groenenboom. When I was still a master-student, you have shown and taught me how to be critical in ways I couldn't have conceived myself. Our continuing collaboration is of great value to me.
I would also like to thank all the people working at the Onsala Space Observatory that make it the great place it is to work at. An honourable mention here for the PhD students; togheter, we lighten the burden put on anyone moving to a strange and new country.
Then, I would like to thank my friends and family, that provide and participate in a range of brilliantly entertaining activities that have nothing to do with the content of this thesis, and, more importantly, give copious support when needed, which has been very relevant to the content of this thesis. Finally, my thanks and love to Yasmin, who is always there for me and puts up with my moodyness that once in a while finds its roots in this work.

CONTENTS

Chapter 1

INTRODUCTION

In this thesis, we will examine the polarization of masers, and in particular, methanol masers. We will discuss a number of subjects, from the molecular scale to the scale of star-formation. This thesis is divided in two parts. The first part consists of six introductory chapters, that will include all of the necessary knowledge to appreciate the appended papers, which form the second part. The introductory chapters are organized as follows.

We will start off with an introductory note to the maser-device and its development, to afterwards move on to the astrophysical maser. We will give a small introduction to the underlying physics of the polarization of the maser, which is tightly bound to spectral splitting due to the Zeeman effect. The polarization of methanol masers can prove a valuable tool in mapping magnetic fields around high-mass star forming regions. It is therefore that the introduction continues with a brief summary of high-mass star formation, its challanges, and the conflicting theories within this subject, as well as the role methanol maser polarization observations can play in formulating constraints for the theory of massive star formation.

The underlying molecular physics is paramount into explaining not only methanol masers' polarization (Zeeman effect), but also the mechanism behind the masing of different specific transitions. In Chapter 2, we will discuss the molecular physics of methanol. We will start the discussion with methanols torsion-rotation structure. We will introduce a formalism that describes the motion of the constituents (electrons and nucleii) of a rotor with one site of internal rotation, like methanol. The kinetic energy of the torsion-rotation motions and their movement through the torsional potential will yield the torsion-rotation Hamiltonian. In the section that follows, we will use the derived expressions for the (charged) particles motions into deriving their resulting magnetic moments. The interaction of these magnetic moments with the nuclear spins of methanols protons, together with the mutual interactions of the nuclear spins

of the protons, will consitute the hyperfine structure. The magnetic moments interaction with an external magnetic field are the Zeeman effects, which will be discussed in the third section of this chapter. We finish the chapter with a short section on the molecular physics behind the methanol masers. We will give some intuitive arguments, based on methanols collisional and radiative rates, as to why we observe some transitions as masers. It is important to note that for methanol, generally, a distinction is made between two classes of masers that have a different excitation mechanism. We will discuss these two classes of masers individually.

When we have introduced the molecular physics of methanol, we are ready to set up the theory of maser polarization by a magnetic field. We introduce a radiation field that couples two states in an ensemble and a phenomenological expression for the maser pumping, to the earlier found expressions for methanols energy structure. We show how the state-populations evolve in time in this system. This evolution will be synchronous with the evolution of the radiation field, due to its interaction with the molecular ensemble. The state-population evolution and the radiation evolution will constitute the maser equations. We will show how the evolution of polarized radiation naturally arises in a molecular ensemble that is permeated by a magnetic field. We continue this chapter with a discussion of mechanisms that will polarize state-populations partially. Such introduced polarization in the state-populations will greatly enhance the polarization of the maser-radiation. Because such mechanisms only require very weak magnetic fields to introduce polarization in the maser, they are called alternative polarization mechanisms. We will end this chapter with a discussion of the possibility of these alternative polarizaiton mechanisms arising for methanol masers.

After having discussed methanols molecular physics, and the theory of maser polarization, we are ready to discuss methanol maser observations. We will briefly go through some of the important single dish methanol maser observations and we will summarize some of the results of interferometric observations of methanol masers, where tighter constraints can be placed on the spatial positions of these masers. Afterwards, we will summarize the methanol maser polarization observations that have been carried out up to this point, and that thus will be re-interpreted in this work.

In the outlook, we will outline some of the future projects that will build on the presented work. We derive a formalism that can easily relate hyperfine-resolved rate-coefficients, collisional and radiative, to torsion-rotation rate-coefficients. We comment on the applicability of such a model in numerically modeling hyperfine-specific maser excitation. Another project is on SiO maser polarization observations towards AGB-stars. SiO masers are suspected to have a far greater influence from alternative polarization mechanisms, and do therefore require more advanced modeling, compared to methanol maser polarization.

We give an outlook to the upcoming observations and more advanced numerical modeling of SiO masers.
In the second part of this thesis, the papers that present the results of this thesis are appended. We give a specific introduction to these publications and place them in the context of the introductory subjects discussed above in Chapter 6.

1.1 Maser

A maser (Microwave Amplified Stimulated Emission of Radiation) is a device or occurrence that facilitates the amplification of radiation by stimulated emission. Masers can be engineered, but also occur naturally in astrophysical environments. In this thesis, we are interested in the astrophysical maser, but we will briefly go through the basic physics behind the general maser.
The theory of masers starts with a quantum mechanical description of matter and radiation. In formulating a quantum theory of radiation, Einstein used the quantum mechanical description of matter, like molecules. Matter is found in certain discrete states, $Z_1,\ Z_2, ...,\ Z_n, ...$, with according energies $\epsilon_1,\ \epsilon_2, ...,\ \epsilon_n, ...$ Now, let Z_n and Z_m be two states, for which $\epsilon_m > \epsilon_n$. To radiatively transfer from one state to the other, Einstein postulated three processes that describe the interaction of light with matter: (i) spontaneous emission, (ii) absorption and (iii) stimulated emission.

(i) *Let a molecule be able to pass spontaneously from the state Z_m to the state Z_n with the emission of radiant energy $\epsilon_m - \epsilon_n$ of frequency ν. Let the probability dW for this to happen in the time dt be(1)*

$$dW = A_{m\to n}dt. \tag{1.1}$$

(ii) *Under the action of the radiation density ρ of the frequency ν a molecule in state Z_n can go over to state Z_m absorbing the radiation energy $\epsilon_m - \epsilon_n$ in accordance with the probability law(1)*

$$dW = B_{n\to m}\rho dt. \tag{1.2}$$

(iii) *In the same way, let the transition $Z_m \to Z_n$ under the action of the radiation also be possible, whereby the radiation energy $\epsilon_m - \epsilon_n$ is emitted according to the probability law(1)*

$$dW = B_{m\to n}\rho dt. \tag{1.3}$$

Nowadays, we call the coefficients $A_{m\to n}$, $B_{m\to n}$ and $B_{n\to m}$, the Einstein coefficients for spontaneous and stimulated emission and the Einstein coefficient for absorption. These processes were first postulated as to occur between a Planck resonator and a radiation field. Later, via a quantum mechanical treatment of

matter and a classical treatment of radiation, it could be proven that the processes of stimulated emission and absorption occur within the electronic dipole approximation(2). The process of spontaneous emission can be shown to occur within the dipole approximation, if one treats the radiation field quantum mechanically(2).
Einsteins theory succesfully showed that by considering these three processes, Planck's radiation law could be (re-)derived. He showed, using the momentum that the photon carries, and the conservation of momentum laws, that the emitted photon by stimulated emission, has the same direction as the stimulating incoming photon.
Now, to appreciate the special conditions required for a maser to occur, we will use the radiative processes, in describing the rate of change of the intensity of the radiation field, I, traveling through a medium

$$\frac{dI}{ds} = A_{m\to n}\rho_m + (B_{m\to n}\rho_m - B_{n\to m}\rho_n)I, \tag{1.4}$$

where ρ_m and ρ_n are the state-populations. If we consider the populations as in thermal equilibrium, and we use the relationship between $B_{m\to n}$ and $B_{n\to m}$ obtained from the limit of very strong radiation, we obtain Planck's radiation law. However, as long as the population ρ_m exceeds ρ_n, we recognize that the radiation intensity will be rising exponentially. In this case, the process of stimulated emission will always be stronger than absorption. This results in a netto 'feed' to the radiation field. Because such a relation between the populations is the opposite from what is expected in thermal equilibrium, we call this population inversion.
An artificially created mechanism for population inversion between two states of ammonia, led to the first maser(3). An elaborate mechanism, making use of a gradually changing electric field, adiabatically causes the population inversion. Incoming radiation at the frequency of the inverted transition, is thus amplified exponentially through the maser device, leading to amplified radiation that is narrow, and has extremely low noise levels(4).
In contrast to the, artificial, experimental masers, in astrophysical environments, the population inversion of molecular states is induced naturally. Pumping of specific levels followed by a de-excitation cascade, can lead to inverted populations of states that allow for a radiative coupling between them. The population inversion has to be maintained along the path where the maser radiation is building up. And to ensure the radiative coupling to be sustained, there can be no large velocity gradient in the maser medium. In a long dense column where these conditions are satisfied, the radiation intensity will build up and the process of stimulated emission will take over as the biggest feed for the radiation field.
The radiation stops rising in intensity when the population inversion is nulli-

fied. This can be due to changing astronomical conditions that do not support the process of population inversion anymore, a loss in velocity coherence, so that the maser radiation is decoupled from the molecular maser transition, or saturation of the maser. In the latter case, the radiative coupling between the maser states becomes so strong, that the population inversion is nullified, and there is no netto feed to the maser radiation anymore.
Because of the exponential build-up of maser radiation, the maser signal will be mainly comprised of maser-rays that have the longest coherent path-length. The consequence of the maser-rays with the longest build-up paths dominating the signal, will mean that a large part of the region where the radiation originates is barely represented in the signal. This effect is called maser beaming. It will cause only a fraction of the source to be effectively visible, so that the maser appears a lot smaller than it actually is.
Astrophysical masers are inherently bound to the extraordinary conditions they arise in. Their appearance is an indication of the dynamics of the regions they are embedded in. Astrophysical masers occur in different molecules and in a large range of frequencies. A wide range of transitions of a molecule can display maser emission, and for each transition to be masing, special conditions are needed. The observation of a particular maser transition can thus be used to constrain the traced regions conditions. In this thesis, we will be interested in the magnetic field of masers regions. A direct consequence of the magnetic field masers occur in, is that the maser-signal will be partially polarized.

Maser polarization

When the radiation of a maser builds up in a medium that is permeated by an (orderly) magnetic field of a few μG or stronger, the maser-radiation will be partially polarized. The, otherwise degenerate, magnetic substates of a particular molecular energy-level will split up (Zeeman splitting), and will have their total angular momentum projected on the magnetic field axis. On a microscopic level, three transitions are possible: $\Delta m = 0, \pm 1$ (π and $\sigma^{\pm}$), accompanied by a photon with the same helicity. In the presence of a magnetic field, these transitions are spectrally decoupled because of the Zeeman splitting (Figure 1.1), so they will propagate to a different extent along the spectral window. The $\sigma^{\pm}$-transitions will be adversely shifted away from the (original) centre of the line. The π-transitions will not be affected by the Zeeman effect (only in broadening, which is negligible with respect to the width of the line). The spectral decoupling of these transitions is reflected in the polarization of the total signal. This polarization will only be a small fraction of the total signal, because the spectral decoupling of the transitions is only partial, and the differently polarized lines will overlap because the Zeeman shifts are far smaller than the maser line-width. Right-circularly polarized radiation (RCP) comes from the

σ^+-transitions and the left-circularly polarized radiation (LCP) comes from the σ^--transitions. The Stokes V-spectrum, that is the RCP-radiation minus the LCP-radiation, will be an S-shaped signal because of the adverse Zeeman shifts of the $\sigma^\pm$-lines. The Stokes Q and U spectra, reflecting the signals linear polarization, will be centered at the centre of the line. The linear polarization is observed as having a direction in the plane of the sky; and it can be shown that polarization of a maser signal by a magnetic field, produces a polarization angle either perpendicular or parallel to the projected direction of the magnetic field on the plane of the sky.
By analyzing the polarization of a maser-signal, one can therefore probe the magnetic field of the traced region. Linear polarization gives the magnetic field morphology, whereas the strength of the Zeeman-effect, proportional to the magnetic field, is traced by the circular polarization. The latter proportionality factor—and thus, key to the magnetic field strength of the traced region—is dependent on the Zeeman-parameters of the molecular transition: so called g-factors.
A large part of this thesis will be dedicated to the Zeeman parameters of the different methanol transitions. Methanol is a complex molecule, that consequently has several contributing Zeeman-effects. Previously, before publication of the results presented in this thesis, the Zeeman-parameters of methanol have remained unknown, and proper interpretation of the large dataset of methanol maser polarization observations (Chapter 4) has not been possible.
Methanol masers occur in the densest parts of high-mass star forming regions, and are one of the strongest and most abundant tracers of gas around high-mass protostellar disks and outflows. Information on magnetic field strength and morphology will prove very useful in constraining conflicting theories of high-mass star formation. In the following section we will briefly go through the theory of high-mass star formation.

1.2 High-mass star forming regions

Among stars we can very roughly distinct two classes. High-mass and low mass stars. High-mass stars have the critical mass to allow for nuclear fusion of elements heavier than He, and have therefore a completely different stellar evolution compared to low-mass stars. The difference in stellar evolution is also reflected in the formation of high-mass stars compared to low-mass stars. The biggest differences being

- From about 10 $M_\odot$, the Kelvin-Helmholtz timescale of the star is less than the accretion time. A consequence is that the star will be in its main-sequence while it is still accreting mass.

- The infalling accreting mass releases a part of its kinetic energy as a feedback. This feedback will be stronger with increasing accretion. From about $10\ M_{\odot}$, the radiative feedback becomes so strong, that the radiation pressure on spherically infalling mass would halt spherical accretion. Mechanical feedback in the form of outward shocks also contributes to ramming back material.

- The cores where massive stars should be formed in, are large enough to allow turbulent motion to dominate the gas-dynamics.

So, a different mechanism of star-formation is in play concerning high-mass star formation. Because of time-scale of high-mass star-formation is very short, orders of magnitude shorter than low-mass star-formation, and the star-formation occurs inside an opaque region, detailed observations of these regions are difficult, and thus only scarce constraints on high-mass star-formation theories can be formulated. Together with the large variability between the sub-stages of the stellar evolution, and the rapid and forceful dynamics involved in the formation process, the formation of high-mass stars is still poorly understood.
We will discuss the two main classes of massive star formation theory, that form the main (and, conflicting) hypotheses of massive star-formation, Core Accretion and Competitive Accretion(5).

Core Accretion Scaling up the theory of low-mass star formation(6) to higher masses, that from observations are known to occur in larger and denser molecular cores, the non-thermal forces of the turbulent motion and magnetic field, become increasingly important. These forces stabilize the core, leading to increasing accretion times. And are balanced out by the larger signal speeds and very high pressure and density of high-mass star forming regions(7). Out of a supersonic molecular core, forms a single massive star. The typical timescale of the formation using such a model will be about 10^5 years(8).
Infalling mass will contain angular momentum because of the initial rotation of the core. The accretion will orient itself in an accretion disk. Having accretion via an accretion disk, as opposed to spherically symmetric Bondi-Hoyle accretion, reduces the radiation pressure on the accreting mass(5). The accretion disk will allow for accretion to overcome radiation pressure up to $100\ M_{\odot}$. The accretion disk has a molecular outflow associated with it; carrying away angular momentum, as well as a part of the infalling mass(5).
Accretion disks and outflows should be ubiquitous in high-mass star forming regions, but observations have not unequivocally shown the ubiquitous presence of accretion disk around high-mass protostars(5). There is strong evidence for methanol masers occurring in accretion disks (see Chapter 4). The strength of these methanol masers, and partial polarization of these signals, makes them

one of the few tracers of the magnetic field. But the sample of these methanol maser (polarization) measurements is still small.
Another problem for this model is that regionally in the star-forming clump, instabilities can occur. This should lead to the fragmentation of the star-forming cloud to form of a manifold of low-mass stars. It is suggested that feedback from surrounding lower-mass protostars can stabilize the clump, and prevent fragmentation(9). Otherwise, a relatively strong magnetic field of $\sim$mG could provide the support needed to prevent clump fragmentation(10; 11). Again, methanol maser magnetic field measurements can shed light on this problem.

Competitive Accretion Young stellar objects are embedded in a large envelope of gas. As a star is moving through the gas it attracts and accretes mass. All of the young stars in the envelope do this, and thus compete with each other for the gas as they move through the cluster(12).
Within a certain radius of a star, mass is attracted to it. This accretion radius, initially, for gas-dominated stellar clusters, is defined by the tidal-lobe forces. When the stars in the envelope accrete more mass, more than the unbound gas in the envelope, they start to dominate the gravitational potential, and accretion occurs via Bondi-Hoyle accretion(12).
Thus two phases are distinguished in the general evolution of the star-forming envelope. In the first phase, where gas dominates the mass and tidal forces dominate the accretion, lower mass stars are formed, and the heaviest of these, have the advantage in the following phase, where Bondi-Hoyle accretion dominates. In this last phase, the heaviest stars will be formed(12; 13).
The accretion rate, however, is much smaller for Competitive Accretion in comparison to Core Accretion. In fact, it should not be possible to form massive stars at the slow timescales of Competitive accretion. This problem is worsened when magnetic field start to be included in simulations. Also, Bondi-Hoyle accretion is not possible for protostellar masses $> 10\ M_{\odot}$. Accretion disks do occur, but are a lot smaller than the Core Accretion counterparts and have chaotically varying orientations. Even though such accretion disk do reduce radiation pressure, the associated outflows impede a part of the accretion(5).

Magnetic fields play a vital role in the accretion of mass on the protostar in both scenarios of Star Formation(5). However, strong observational constraints have not been formulated for a wide range of conditions. Methanol masers occur in the densest parts of high-mass star forming regions, and are one of the strongest and most abundant tracers of gas around high-mass protostellar disks and outflows. Polarization observations of this maser specie will provide information on the magnetic field strength in these regions. To properly interpret the maser polarization observations of methanol, one needs to model on the Zeeman-parameters of the involved transitions. This modeling is introduced in

the next chapter.

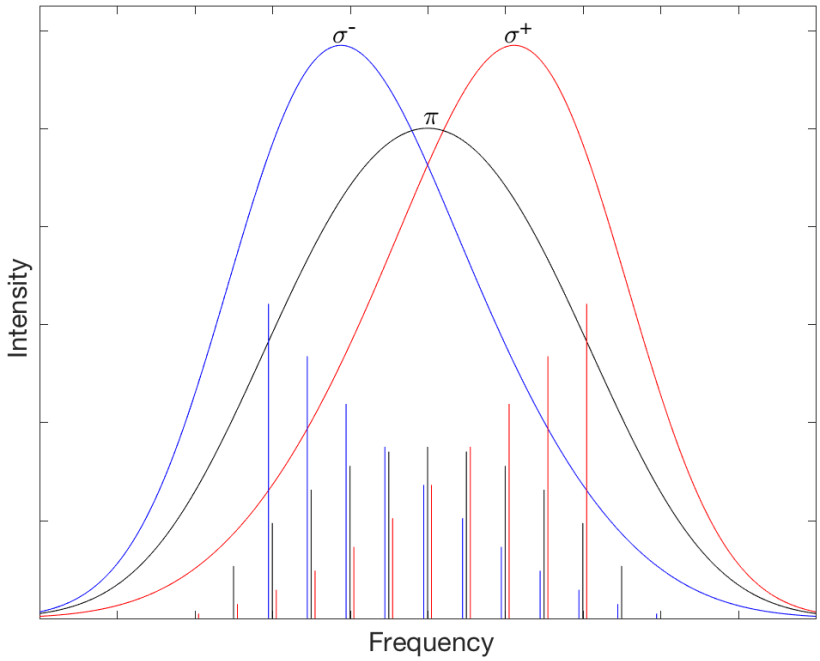

Fig. 1.1: Spectral decoupling of the different type of transitions ($\sigma^{\pm}$ and π). We have plotted the σ^{+}- (red), σ^{-}- (blue) and π- (black) -transitions within a $j = 5 \rightarrow j' = 6$-transition, with a certain Zeeman splitting, that is smaller than the (Gaussian) broadening of the line. Straight lines in the figure demarcate the individual $m \rightarrow m'$-transitions and their length is relative to their intensity. The different $\sigma^{\pm}$ and π-transitions are spectrally decoupled, depending on the strength of the Zeeman effect. $\sigma^{\pm}$-transitions show an asymmetric spectrum ($\sigma^{+} + \sigma^{-}$ would be symmetric).

Chapter 2

MOLECULAR PHYSICS OF METHANOL

2.1 The energy-spectrum of methanol

All the relevant maser species of methanol (table 4.1) are in the ground vibrational state, and are transitions between torsion-rotation states. The ground electronic state is a closed-shell state, meaning that it has no unpaired molecules, and thus no orbital or spin-angular momentum. In the pursuit of methanol's Zeeman effect, we thus have to consider the non-paramagnetic Zeeman effects. These non-paramagnetic Zeeman effects come from the molecules motion, as well as from the nuclear spins of the protons. A charged particle in motion has a particular current which induces a magnetic moment. The nuclear spins have an intrinsic magnetic moment. These Zeeman effects scale with the nuclear magneton, $\mu_N \approx 0.47$ kHz/G, 1816 times weaker then for paramagnetic molecules.
But before we will discuss methanol's Zeeman effect, we will discuss the spectrum of the molecule at zero magnetic field. This will involve a discussion on methanols torsion-rotation structure, followed by a discussion on methanols hyperfine structure. When the hyperfine structure and torsion-rotation structure have been discussed, we will move on to methanols Zeeman effect.
The following theory has already been derived and presented in Paper I and II, but for the sake of completeness of this thesis, we will give a short summary of these theories in the following.

2.1.1 Torsion-rotation structure

Since we consider methanol in its ground vibrational state, we will assume all particles to be situated at some vibrationally averaged position. The only motion present then, is the rotational motion, torsional motion and a translational motion. The translational motion is decoupled from the other motions and will

only present itself in a spectrum as a doppler shift. The torsional motion occurs at the CO bond, where the the methyl group, the rotating "top", can internally rotate with respect to the OH group, the "frame" (see Fig. 2.1). The torsional motion is described by the internal rotation angle, γ. The overall rotation of the entire molecule is described as the rotational motion, and is described by the three Euler angles $\chi\theta\phi$. Rotational and torsional motions are coupled via the so-called coriolis coupling(14). The kinetic energy of the torsion-rotation motion is (Paper I)

$$2T = \boldsymbol{\omega}^T \boldsymbol{I} \boldsymbol{\omega} + \dot{\gamma} \boldsymbol{\lambda}^T \boldsymbol{I}^{\text{top}} \boldsymbol{\omega} + \dot{\gamma} \boldsymbol{\omega}^T \boldsymbol{I}^{\text{top}} \boldsymbol{\lambda} + I_\gamma \dot{\gamma}^2, \tag{2.1}$$

where $\dot{\gamma}$ is the time-derivative of the internal rotation angle, the angular velocity $\boldsymbol{\omega}$ is related to the time-derivatives of the Euler angles. $\boldsymbol{\lambda}$ is the unit vector around which the internal rotation takes place. The inertiatensors

$$\begin{aligned} \boldsymbol{I} &= \sum_i^{\text{all}} m_i \left(\boldsymbol{r}_i^{\text{MF}} \cdot \boldsymbol{r}_i^{\text{MF}} \mathbf{1} - \boldsymbol{r}_i^{\text{MF}} \otimes \boldsymbol{r}_i^{\text{MF}} \right) \\ \boldsymbol{I}^{\text{top}} &= \sum_i^{\text{top}} m_i \left(\boldsymbol{r}_i^{\text{MF}} \cdot \boldsymbol{r}_i^{\text{MF}} \mathbf{1} - \boldsymbol{r}_i^{\text{MF}} \otimes \boldsymbol{r}_i^{\text{MF}} \right) \\ I_\gamma &= \boldsymbol{\lambda}^T \boldsymbol{I}^{\text{top}} \boldsymbol{\lambda} \end{aligned} \tag{2.2}$$

are computed in the molecular frame, MF, as defined in Paper I. The position of consituent i, is $\boldsymbol{r}_i^{MF}$ and its mass is m_i. The inertiatensor of the rotating top has a sum over all particles in the top.
For a convenient transition to a quantum-mechanical formalism, that will become important later, we will choose to write the kinetic energy in terms of angular momentum operators (Paper I)

$$\begin{aligned} \boldsymbol{J} &= \frac{\partial T}{\partial \boldsymbol{\omega}} = \boldsymbol{I}\boldsymbol{\omega} + \boldsymbol{I}^{\text{top}} \boldsymbol{\lambda} \dot{\gamma} \\ p_\gamma &= \frac{\partial T}{\partial \dot{\gamma}} = \boldsymbol{\omega} \cdot \boldsymbol{I}^{\text{top}} \boldsymbol{\lambda} + I_\gamma \dot{\gamma}. \end{aligned} \tag{2.3}$$

so that the kinetic energy of the torsion-rotational motion becomes (Paper I)

$$T = \frac{1}{2} \boldsymbol{J} \cdot \boldsymbol{I}^{-1} \boldsymbol{J} + F \left(p_\gamma - \boldsymbol{\rho} \cdot \boldsymbol{J} \right)^2, \tag{2.4}$$

where

$$F = \frac{1}{2} \left(I_\gamma - \boldsymbol{\rho}^T \boldsymbol{I} \boldsymbol{\rho} \right)^{-1} \qquad \text{and} \qquad \boldsymbol{\rho} = \boldsymbol{I}^{-1} \boldsymbol{I}^{\text{top}} \boldsymbol{\lambda}. \tag{2.5}$$

The quantum-mechanical equivalent, $\hat{T}$, is given in Ref. (14), and is obtained by replacing $\boldsymbol{J} \rightarrow \hat{\boldsymbol{J}}$, where $\hat{\boldsymbol{J}}$ is the angular momentum operator fulfilling the usual commuation relations(16), and replacing $p_\gamma \rightarrow \hat{p}_\gamma = (\hbar/i)\partial/\partial\gamma$.

Unlike the rotational motion, the torsional motion is through a potential field (see Fig. 2.1). The internal rotation of the methyl-group is hindered by the OH-group. The resulting potential, $V(\gamma)$, is added to the torsion-rotation kinetic energy to yield the Hamiltonian of the torsion-rotational motion:

$$\hat{H}_{\text{rot. tors.}} = \hat{T} + \hat{V}(\gamma). \tag{2.6}$$

The diagonalization of the torsion-rotation Hamiltonian is done for two orthogonal bases of torsional functions—of A- and E-symmetry. The eigenvalues and eigenfunctions of the diagonalized torsion-rotation Hamiltonian are the energies and wave functions of the torsion-rotation states(17). The torsion-rotation wave functions contain information on the molecular states motion, that will be used in formulating a model on the hyperfine structure, which will be introduced in the next section.

2.1.2 Hyperfine structure

The protons in methanol are the only nuclei that have in their most abundant isotope a non-zero nuclear spin. The nuclear spin of the protons is $\frac{1}{2}$ and thus exhibit no measurable quadrupole interaction. The nuclear spins of the protons carry a magnetic moment that is proportional to the nuclear magneton and the proton g-factor $g_p \approx 5.558$. These magnetic moments interact among each other, as the magnetic dipole-dipole interaction (Paper I)

$$\hat{H}^{\text{SS}} = \sum_{K>L} \hat{\boldsymbol{I}}_K \cdot \boldsymbol{D}_{KL}(\gamma) \hat{\boldsymbol{I}}_L, \tag{2.7}$$

where the sum is over all protons, and $\boldsymbol{D}_{KL}(\gamma)$ is the internal-rotation angle-dependent dipole-dipole tensor, that describes the coupling of the nuclear spin-angular momenta of protons K and L. This dipole-dipole tensor can be computed from the molecular geometry(18).
The motion of the consituents of methanol, which are charged, induce a magnetic field, that will also interact with the proton magnetic moments. This interaction is called the spin-rotation interaction. Because methanol also exerts a torsional motion, the resulting magnetic field from this motion will give an additional coupling to the proton magnetic moments, that is called the spin-torsion interaction. The total spin-rotation interaction for methanol, which is the sum of the spin-rotation and spin-torsion interactions, can be written as (Paper I)

$$\hat{H}^{\text{SR}} + \hat{H}^{\text{ST}} = -\sum_K \left[\hat{\boldsymbol{I}}_K \cdot \boldsymbol{M}_K(\gamma) \hat{\boldsymbol{J}} + \hat{\boldsymbol{I}}_K \cdot \boldsymbol{d}'_K(\gamma) f \left(\hat{p}_\gamma - \boldsymbol{\rho} \cdot \hat{\boldsymbol{J}} \right) \right]. \tag{2.8}$$

with the dimensionless constant

$$f = 2FI_\gamma = (1 - \boldsymbol{\rho} \cdot \boldsymbol{\lambda})^{-1}, \tag{2.9}$$

and where the spin-rotation tensor,

$$\boldsymbol{M}_K(\gamma) = \sum_i \frac{Z_i e g_K \mu_N}{c} r_{Ki}^{-3} \left[\left(\boldsymbol{r}_{Ki}^{\mathrm{MF}} \cdot \boldsymbol{r}_{Ki}^{\mathrm{MF}} \right) \mathbf{1} - \boldsymbol{r}_{Ki}^{\mathrm{MF}} \otimes \boldsymbol{r}_{Ki}^{\mathrm{MF}} \right] \boldsymbol{I}^{-1}, \tag{2.10}$$

and spin-torsion coupling tensor,

$$\begin{aligned} \boldsymbol{d}_K(\gamma) &= \sum_i^{\mathrm{top}} \frac{Z_i e g_K \mu_N}{c} r_{Ki}^{-3} \left[\left(\boldsymbol{r}_{Ki}^{\mathrm{TF}} \cdot \boldsymbol{r}_{Ki}^{\mathrm{TF}} \right) \mathbf{1} - \boldsymbol{r}_{Ki}^{\mathrm{TF}} \otimes \boldsymbol{r}_{Ki}^{\mathrm{TF}} \right] \boldsymbol{\lambda} I_\gamma^{-1}, \text{ and} \\ \boldsymbol{d}'_K(\gamma) &= \boldsymbol{d}_K(\gamma) - \boldsymbol{M}_K(\gamma) \boldsymbol{\lambda}, \end{aligned} \tag{2.11}$$

are functions of the internal rotation angle, γ. The positions are given in the top-frame, TF (see Paper I for a discussion on the different frames), and the constants e, Z_i, c, g_K and mu_N are the elementary charge, the charge of particle i, the speed of light, the g-factor of nucleus K and the nuclear magneton. The spin-rotation and spin-torsion tensors are unique for each proton, although there do exist symmetry relations for the tensors of the methyl-protons (Paper I). The spin-rotation tensors can be computed by quantum-chemical methods(19), but the spin-torsion tensors cannot.
The dipole-dipole interactions and the total spin-rotation interactions form the hyperfine interactions

$$\hat{H}_{\mathrm{hyperfine}} = \hat{H}^{\mathrm{SS}} + \hat{H}^{\mathrm{SR}} + \hat{H}^{\mathrm{ST}}. \tag{2.12}$$

Matrix elements of this Hamiltonian can be obtained in a angular momentum basis, where the rotational angular momentum is coupled to the proton spin-angular momenta to a total hyperfine angular momentum, F (see Paper I). Here, special attention has to be given to the symmetry of the rotational, nuclear spin, and total wave functions (Paper I). As mentioned, the spin-rotation and dipole-diople tensors can be calculated by quantum-chemical methods, but the spin-torsion coupling tensor cannot. In Paper I, it are the spin-torsion tensors that are fitted to the experimental spectra(18; 20), while the rest of the ab-intio computed tensors are kept constant. We use this model on the hyperfine struture in, later, computing the Zeeman interactions of methanol.
Paper I also contains a discussion on the Thomas precession interaction, that has been taken into account in by previous models on methanols hyperfine structure(21; 18; 20), but in an incorrect manner. By considering the motion of the protons through a potential field, Paper I shows the correct way to consider Thomas precession correction of the spin-rotation and spin-torsion interaction, and shows that it is actually negligable.
The magnetic moments interacting between each other, can also interact with an external magnetic field, which constitutes the Zeeman interactions. From this, it is clear that this Zeeman effect is highly dependent on the internal hyperfine

structure. In the next section, we will introduce an external magnetic field to compute methanols Zeeman effect.

2.1.3 Methanol in a magnetic field

We have already seen, that the moving charged particles in methanol, induce a magnetic field. Associated with this magnetic field is also a magnetic moment (Paper II)

$$\boldsymbol{m} = \frac{1}{2}\sum_i Q_i(\boldsymbol{r}_i \times \boldsymbol{v}_i), \tag{2.13}$$

where Q_i is the charge of particle i and $\boldsymbol{v}_i$ is its velocity. The resulting magnetic moment will couple to an external magnetic field to give the interaction $H = -\boldsymbol{B}\cdot\boldsymbol{m}$. From the discussion on methanols torsion-rotation motion, we know that the motion of the charged particles can be divided into a rotational and a torsional motion. We use this, to divide the velocity term, $\boldsymbol{v}_i$, in a torsional and rotational, to obtain the rotational and torsional Zeeman interactions (Paper II)

$$\hat{H}^{\mathrm{BR}} + \hat{H}^{\mathrm{BT}} = -\frac{\mu_N}{\hbar}\boldsymbol{B}\cdot\boldsymbol{g}(\gamma)\hat{\boldsymbol{J}} + \frac{\mu_N}{\hbar}f\boldsymbol{B}\cdot\boldsymbol{b}'(\gamma)\left(\hat{p}_\gamma - \boldsymbol{\rho}\cdot\hat{\boldsymbol{J}}\right), \tag{2.14}$$

where we have the coupling-tensors, the rotational g-tensor (Paper II)

$$\boldsymbol{g}(\gamma) = \frac{\hbar}{\mu_N}\sum_i \frac{Q_i}{2}\left[(\boldsymbol{r}_i^{\mathrm{MF}}\cdot\boldsymbol{r}_i^{\mathrm{MF}})\mathbf{1} - \boldsymbol{r}_i^{\mathrm{MF}}\otimes\boldsymbol{r}_i^{\mathrm{MF}}\right]\boldsymbol{I}^{-1} \tag{2.15}$$

that describes the coupling of the overall rotation to the magnetic field, and the torsional b-vector (Paper II)

$$\begin{aligned}\boldsymbol{b}(\gamma) &= \frac{\hbar}{\mu_N}\sum_i^{\mathrm{top}} \frac{Q_i}{2}[(\boldsymbol{r}_i^{\mathrm{TF}}\cdot\boldsymbol{r}_i^{\mathrm{TF}})\mathbf{1} - \boldsymbol{r}_i^{\mathrm{TF}}\otimes\boldsymbol{r}_i^{\mathrm{TF}}]\boldsymbol{\lambda}I_\gamma^{-1}\\ \boldsymbol{b}'(\gamma) &= \boldsymbol{b}(\gamma) - \boldsymbol{g}(\gamma)\boldsymbol{\lambda}.\end{aligned} \tag{2.16}$$

that describes the coupling of the torsional motion to the magnetic field. Do note, that the torsional and rotational motion are not uncoupled.
The magnetic momets resulting from the proton-spins we have already introduced. When they couple to an external magnetic field, this leads to the interaction (Paper II)

$$\hat{H}^{\mathrm{BS}} = -\frac{\mu_N}{\hbar}g_p\sum_K \boldsymbol{B}\cdot\hat{\boldsymbol{I}}, \tag{2.17}$$

where μ_N stands for the nuclear magneton.

The total Zeeman interaction, is a sum of the rotational, torsional and nuclear spin Zeeman interactions (Paper II)

$$\hat{H}_{\text{Zeeman}} = \hat{H}^{\text{BR}} + \hat{H}^{\text{BT}} + \hat{H}^{\text{BS}} \tag{2.18}$$

and can be computed in the same basis as we used for the hyperfine interactions. Do note, that the total hyperfine quantum number, F, is not a good quantum number anymore, as the Zeeman Hamiltonian mixes F and $F \pm 1$ states. The projection of the total angular momentum on the space-fixed z-axis, M_F, remains the only good quantum number.
Paper II details the calculation of methanols Zeeman effect. The rotational g-factor can be computed with quantum-chemical methods(19), but this cannot be done for the torsional b-vector. Instead, an estimate is made by using available experimental data on similar molecules(22; 23).
The results of the calculations to methanols Zeeman effect are given in Paper II. The Zeeman effect is found, as can be expected, to differ strongly within the different hyperfine states. Also, it is found to be non-linear already for regimes of low magnetic field. A discussion on the latter phenomenon can be be found in the supplementary material of Paper II. The results of Paper II can be easily summarized as tables containing the Landé of all strong hyperfine transitions within the different methanol maser-lines. Such summarizing results are also given in the supplementary material of Paper II.

2.2 Molecular physics behind the methanol maser

Methanol molecules are mainly formed on grain-surfaces(24). As a shock travels through the dusty accretion disk around the high-massive protostar, it releases the methanol molecules locked up in cavities in the dust. The enhanced concentration of methanol is subsequently excited (collisionally, class I, radiatively, class II) to higher (torsional, class II) states, from where it relaxes accordingly, radiatively, or by (inelastic) collisions with mostly H_2. The selective excitation and relaxation of and to specific torsion-rotation states, will lead to population inversion of some transitions. The type of excitation, radiative or collisional, will lead to population inversion in different transitions. Here, we will discuss the mechanisms for population inversion of methanol in its two separate classes of masers.
Class I. The maser excitation of the collisionally pumped Class I masers can be qualitatively understood by considering some propensity arguments for the collisional excitation. The Class I methanol masers are mainly found as the E-type $J_{-1} - (J-1)_0$ torsion-rotation transitions and the $J_2 - J_1$. Because of the torsional kinetics, the $K = -1$ levels lie generally lower than the $K = 0$ levels. In fact, the two lowest E-type energy-levels are the 1_{-1} and 2_{-1} levels. It follows

that before a pumping event, these levels have the highest population. From collisional observations(25) and modeling(26), we see a strong propensity for $|\Delta J|= 1$ and $\Delta K = 0$ transitions. So naturally, from the enhanced initial $K = -1$-populations, and the propensity for $\Delta K = 0$ collisional transitions, the higher J, $K = -1$ states are naturally inverted. Also, for para-hydrogen, $|\Delta K|= 3$ are favorable with respect to other $\Delta K \neq 0$ collisional transitions, because of the three-fold symmetry of the methyl group. The higher propensity of $|\Delta K|= 3$ collisions facilitates the population inversion of the $K = 2$-states with respect to the $K = 1$ states, leading to the masing of the $J_2 - J_1$-lines.

Similar arguments can be made to explain the masing of different A-type masers. Only in A-symmetry methanol, the lowest energy states are predominantly $K = 0$ states. Collisional excitation thus leads to overpopulation of the higher J, $K = 0$ states and leads to masing of, e.g., the $7_0 - 6_1$ A^+ (44 GHz) and the $8_0 - 7_1$ A^+ (95 GHz) lines.

Class II. The Class II methanol maser is not as easily understood as the Class I maser. It occurs towards HII regions, from where UV-radiation is rescattered by dust particles at IR frequencies. The IR radiation is strong enough to facilitate torsional transitions, which have the selection rule: $|\Delta K|= 1$. Promotion to, and emission from, the first torsionally excited state yields thus, $\Delta K = 0,\ \pm 2$. An overpopulated level at $K = 0$, would therefore lead, if excitation occurs via the first excited torsional state, to overpopulated levels at $K = \pm 2$ and $K = 0$. This scheme supports, e.g., the simultaneous detection of the masers $9_2 - 10_1$ A^+ and $6_2 - 5_1$ $A^{\pm}$, while absorption is detected for $10_1 - 9_2$ A^- and $11_1 - 10_2$ A^+(27). But, this simple scheme is not sophisticated enough to explain masing of the E-type Class II transitions, nor can it explain the strongest $5_1 - 6_0$ A^+ maser at 6.7 GHz.

It is not until the introduction of more advanced numerical models, that a better understanding of Class II methanol masers can be obtained. To model these masers properly, one needs to involve at least the first two torsionally excited states, including transitions between them and the torsional ground state(28). Also, one needs to account for relaxational pathways via collisions with H_2. With the inclusion of the drastically improved collisional rate coefficients of methanol with He(29) and (para-)H_2(30), the latest modeling of Class II methanol masers comes from Ref. (31). The excitation conditions of the Class II masers can be accurately modelled in these models, but it is increasingly dependent on the collisional rate-coefficients at larger densities. It are these regions that we are mostly interested in, when studying maser polarization.

For these cases of higher excitation densities, Class II methanol maser theories should be revisited, and also include the recent extension of collisional rate coefficients between methanol and H_2, that also include the ortho-variant of molecular hydrogen(26). The propensities of $\Delta K \neq 0$ transitions are qual-

itatively different from para-H_2, and rate-coefficients are significantly higher when ortho-H_2 is the perturber(26). This result will have the biggest impact on the high-density excited Class II methanol masers, i.e., the masers observed for their polarization.

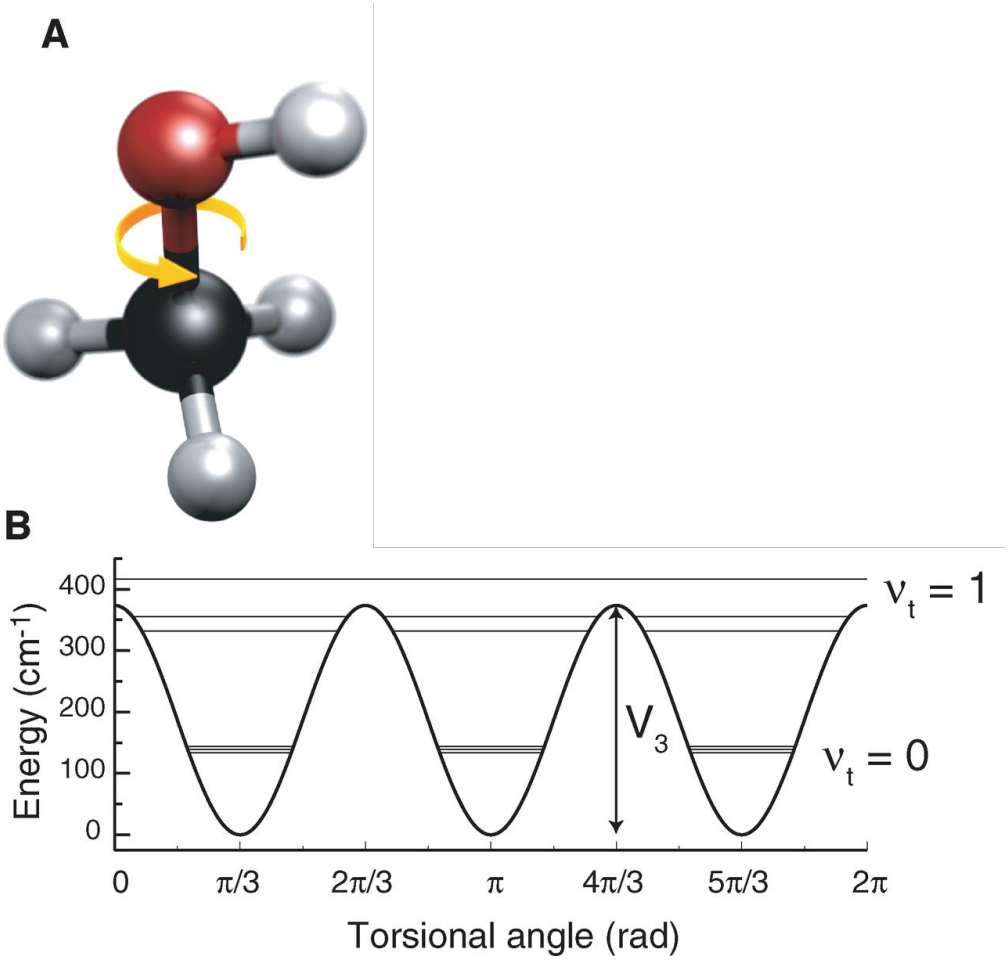

Fig. 2.1: Variation of the potential energy of methanol with the relative rotation, γ, of the OH group with respect to the methyl group about the molecular axis. Figure taken from Ref. (15).

Chapter 3

MASER POLARIZATION THEORY

3.1 Maser polarization by magnetic fields

The theory presented here is based Ref. (32), and the extension for numerical modeling by Refs. (33; 34; 35). The work, reported in Refs. (36; 37; 38; 39), that proposes a different model of the maser polarization, will not be mentioned. The latter work has been criticized heavily(40; 41; 42).
In our models, the maser-molecules are permeated by a magnetic field. This lifts the degeneracy of the magnetic substates. The consequential spectral decoupling of the photon-transitions with different helicity will cause a polarization of the radiation. That is why, in building this model, we have to consider all the magnetic substates in the maser-transitions, as well as all the modes of polarization in the radiation (the four Stokes parameters).
Setting up the theory of maser radiation propagation falls in two parts, because the propagation of the radiation will be synchronous with the evolution of the state-populations of the molecular ensemble. So, on the one hand, we will present a model on the propagation of the state-populations under the influence of a (polarized) radiation field, and on the other hand, we will present a model on the propagation of the radiation field, that is dependent on the state-populations.

3.1.1 Evolution of the density operator

Following Ref. (34), the ensemble of the masing molecules can be expressed in terms of the density operator. If we limit ourselves to a two (rotational or hyperfine) state system[1]. The two states are coupled by the radiation field and

[1] Because we speak about a two-state system, specfically referring to them being hyperfine or rotational levels, we are in fact speaking about two states that have magnetic sublevels, dependent on their total angular momentum.

we have the Hamiltonian

$$\hat{H} = \begin{pmatrix} \hat{H}^{(1)} & \hat{V}^{(12)} \\ \hat{V}^{(21)} & \hat{H}^{(2)} \end{pmatrix}, \tag{3.1}$$

where $\hat{H}^{(1)} = \hat{H}_0^{(1)} + \hat{H}_{\text{Zeeman}}^{(1)}$ is the Hamiltonian of the upper state '1', and consists of the zero-field Hamiltonian (see section 2.1.1 and 2.1.2) and the Zeeman Hamiltonian (see section 2.1.3). In case that the Zeeman-interaction is way bigger than $V^{(12)}$, the principal axis lies along the magnetic field. The two states are coupled by a radiation field, represented by the electric field vector E. The coupling term is represented by

$$\hat{V} = -E \cdot \hat{d} = \frac{1}{2} \sum_m E_m d_{-m}, \tag{3.2}$$

where $\hat{d} = -q\hat{r}$, is the dipole operator.
We take into account the excitation of both levels, by including a phenomenological term for the pumping of the maser: $\hat{\Lambda}$, and the decay of the states by $\hat{\Gamma}$. The Liouville-von Neumann equation is extended with these terms and we have have the time evolution of the density operator as(32; 34)

$$\dot{\hat{\rho}} = -\frac{i}{\hbar}(\hat{H}\hat{\rho} - \hat{\rho}\hat{H}) - \hat{\Gamma}\hat{\rho} + \hat{\Lambda}. \tag{3.3}$$

We make a similar decomposition for the density operator as for the Hamiltonian and notate

$$\hat{\rho} = \begin{pmatrix} \hat{\rho}_1 & \hat{\rho}_{12} \\ \hat{\rho}_{21} & \hat{\rho}_2 \end{pmatrix}. \tag{3.4}$$

The evolution of the decomposed density operators is then

$$\dot{\hat{\rho}}_1 = -\frac{i}{\hbar}\left([\hat{H}_1, \hat{\rho}_1] + \hat{V}_{12}\hat{\rho}_{21} - \hat{\rho}_{12}\hat{V}_{21}\right) - \hat{\Gamma}_1\hat{\rho}_1 + \hat{\Lambda}_1 \tag{3.5a}$$

$$\dot{\hat{\rho}}_2 = -\frac{i}{\hbar}\left([\hat{H}_2, \hat{\rho}_2] + \hat{V}_{21}\hat{\rho}_{12} - \hat{\rho}_{21}\hat{V}_{12}\right) - \hat{\Gamma}_2\hat{\rho}_2 + \hat{\Lambda}_2 \tag{3.5b}$$

$$\dot{\hat{\rho}}_{12} = -\frac{i}{\hbar}\left(\hat{H}_1\hat{\rho}_{12} - \hat{\rho}_{12}\hat{H}_2 + \hat{V}_{12}\hat{\rho}_2 - \hat{\rho}_1\hat{V}_{12}\right) - \hat{\Gamma}_1\hat{\rho}_{12}. \tag{3.5c}$$

Let us start by finding an expression for the elements in $\hat{\rho}_{12}$. First of all, these elements have a time-dependence, so that we have to solve Eq. (3.5c) as a differential equation. We use Eq. (3.2) for the perturbation operator, and transform the time-dependent electric field as

$$E_m(t) = \frac{1}{\sqrt{2}} \int d\omega \; E_m(\omega) e^{-i\omega(t - s/c)}, \tag{3.6}$$

then, we follow the procedure as explained in Ref. (34), to obtain expressions for the coupling density matrix elements:

$$\rho_{ab} = -\frac{i}{\hbar}\int_{-\infty}^{t} dt' \left(\sum_{b'} V_{ab'}\rho_{b'b} - \sum_{a'}\rho_{aa'}V_{a'b}\right) e^{-(\Gamma+i\omega_{ab})(t-t')}$$

$$\simeq -\frac{i}{2\sqrt{2\pi}\hbar}\sum_{p}\left(\sum_{b'} d^{ab'}_{-p}\rho_{b'b} - \sum_{a'}\rho_{aa'}d^{a'b}_{-p}\right)\int d\omega\ \gamma^{ab}_{+}E_p(\omega)e^{-i\omega(t-s/c)}, \tag{3.7}$$

where $\rho_{aa'}$ is an element from $\hat{\rho}_1$ and $a,\ a'$ run over all magnetic substates of the upper state, likewise $\rho_{bb'}$ is an element from $\hat{\rho}_2$ and $b,\ b'$ run over all magnetic substates of the lower state. Also, ρ_{ab} is an element of $\hat{\rho}_{12}$, and

$$\gamma^{ab}_{+} = \frac{1}{\Gamma + i\left[\omega_{ab} - \omega(1-\frac{v}{c})\right]}. \tag{3.8}$$

Later on, we will use Eq. (3.7) in describing the polarization of the medium, but let us first continue with the expression for the state-populations. We will assume that the response of the state-populations to the radiation field is rapid, so that

$$\frac{d\hat{\rho}_1}{dt} = \frac{d\hat{\rho}_2}{dt} = 0 \tag{3.9}$$

and we work under the assumption of a stationary system, so that the time-average

$$\langle E_m(\omega)E^*_{m'}(\omega')\rangle = 2\pi F_{mm'}\delta(\omega-\omega'), \tag{3.10}$$

where $F_{mm'}$ can be related to the Stokes-parameters

$$I(\omega) = \frac{c}{8\pi}\left(F_{--} + F_{++}\right), \tag{3.11a}$$

$$V(\omega) = \frac{c}{8\pi}\left(F_{--} - F_{++}\right), \tag{3.11b}$$

$$Q(\omega) - iU(\omega) = -\frac{c}{4\pi}F_{-+}. \tag{3.11c}$$

Following Ref. (34), we then have, for the upper state-populations

$$0 = -(\Gamma + i\omega_{aa'})\rho_{aa'}(v) + \phi(v)\lambda_{aa'} + \frac{\pi}{c\hbar^2}\left[\sum_{bb'}\rho_{bb'}(v)\left(\langle\gamma^{a'b'}_{-}\zeta^{a'b,ab'}\rangle_\omega + \langle\gamma^{ab}_{+}\zeta^{a'b,ab'}\rangle_\omega\right)\right.$$

$$\left. - \sum_{ba''}\rho_{a''a'}(v)\,\langle\gamma^{a'b}_{-}(\zeta^{ab,a''b})^*\rangle_\omega - \sum_{ba''}\rho_{aa''}(v)\,\langle\gamma^{ab}_{+}(\zeta^{a'b,a''b})^*\rangle_\omega\right], \tag{3.12}$$

where we have used some simplified notations

$$\zeta^{ij,kl} = I(\omega)\delta^{ij,kl}_{I} - Q(\omega)\delta^{ij,kl}_{Q} - iU(\omega)\delta^{ij,kl}_{U} + V(\omega)\delta^{ij,kl}_{V} \tag{3.13}$$

and

$$\delta_I^{ij,kl} = (d_+^{ij})^* d_+^{kl} + (d_-^{ij})^* d_-^{kl} \tag{3.14}$$
$$\delta_Q^{ij,kl} = (d_+^{ij})^* d_-^{kl} + (d_-^{ij})^* d_+^{kl} \tag{3.15}$$
$$\delta_U^{ij,kl} = (d_+^{ij})^* d_-^{kl} - (d_-^{ij})^* d_+^{kl} \tag{3.16}$$
$$\delta_V^{ij,kl} = (d_+^{ij})^* d_+^{kl} - (d_-^{ij})^* d_-^{kl} \tag{3.17}$$

and we have use a simplified notation for the integral

$$\langle \gamma_\pm^{ij} \zeta^{kl,mn} \rangle_\omega = \int d\omega \; \gamma_\pm^{ij}(\omega, v) \zeta^{kl,mn}(\omega), \tag{3.18}$$

and the dipole matrix elements are

$$d_\pm^{ab} = \pm d_{M=1}^{ab} \frac{1 \pm \cos\theta}{2} + i d_{M=0}^{ab} \frac{\sin\theta}{\sqrt{2}} \mp d_{M=-1}^{ab} \frac{1 \mp \cos\theta}{2}. \tag{3.19}$$

The lower state-populations follow from a similar derivation. A lot of complexity lies in the equations for the state-populations. It might therefore be insightful to disect the different parts of Eq. (3.12). On the whole, the first part of Eq. (3.12)

$$(-\Gamma + i\omega_{aa'})\rho_{aa'}(v),$$

represents the spontaneous decay of the $\rho_{aa'}(v)$ population; and for the non-diagonal elements, a shift in frequency is also given by $i\omega_{aa'}$. The pumping is represented by

$$\phi(v)\lambda_{aa'}$$

and is dependent on the molecules velocity, v. We have a velocity-distribution of molecules in the ensemble, dependent on the temperature: $\phi(v)$. The pumping is given by $\lambda_{aa'}$, usually zero for $a \neq a'$. The part after these two terms, are concerned with the radiative coupling of the two states. The part

$$\frac{\pi}{c\hbar^2} \sum_{bb'} \rho_{bb'}(v) \left(\langle \gamma_-^{a'b'} \zeta^{a'b,ab'} \rangle_\omega + \langle \gamma_+^{ab} \zeta^{a'b,ab'} \rangle_\omega \right)$$

represents the absorption of radiation, exciting molecules from the lower to the upper state. It is dependent on both the radiation field and the dipole coupling between the two states. The radiation field is represented by the Stokes paramaters, and the coupling of this radiation field between two states via the δ-operators—make note that the coupling is dependent on the angle that the magnetic field makes with the radiation field. The remaining terms

$$-\frac{\pi}{c\hbar^2} \left[\sum_{ba''} \rho_{a''a'}(v) \langle \gamma_-^{a'b} (\zeta^{ab,a''b})^* \rangle_\omega + \sum_{ba''} \rho_{aa''}(v) \langle \gamma_+^{ab} (\zeta^{a'b,a''b})^* \rangle_\omega \right]$$

describe the stimulated emission, having a lot of resemblence to the absorption term.

3.1.2 Evolution of the radiation field

The transverse part of the electric field and polarization can be decomposed into their circularly polarized components by

$$E(z,t) = Re\left(E^{+}(z,t)\hat{e}_{+} + E^{-}(z,t)\hat{e}_{-}\right), \qquad P(z,t) = Re\left(P^{+}(z,t)\hat{e}_{+} + P^{-}(z,t)\hat{e}_{-}\right), \tag{3.20}$$

where

$$E^{\pm}(z,t) = \mathcal{E}^{\pm}(z,t)e^{-i(\omega(t-z/c)+\phi^{\pm}(z,t))}, \qquad P^{\pm}(z,t) = \mathcal{P}^{\pm}(z,t)e^{-i(\omega(t-z/c)+\phi^{\pm}(z,t))} \tag{3.21}$$

where ω is the frequency of the radiation. Where the amplitude $\mathcal{E}^{\pm}$ is real, but $\mathcal{P}^{\pm}$ is complex. We can assume $\partial\mathcal{E}^{\pm}/\partial t << \omega|\mathcal{E}^{\pm}|$ $\partial\mathcal{E}^{\pm}/\partial z << k|\mathcal{E}^{\pm}|$ $\partial\phi^{\pm}/\partial t << \omega$ $\partial\phi^{\pm}/\partial z << k$, so that we can describe the propagation of the electric field as proportional to the polarization of the medium:

$$\left(\frac{1}{c}\frac{\partial}{\partial t} + \frac{\partial}{\partial s}\right)\mathcal{E}_p(s,t) = \frac{2\pi i\omega}{c}\mathcal{P}_p(s,t) \tag{3.22}$$

so that

$$\left(\frac{1}{c}\frac{\partial}{\partial t} + \frac{\partial}{\partial s}\right)[\mathcal{E}_p(\mathcal{E}_{p'})^*] = \frac{2\pi i\omega}{c}[\mathcal{P}_p(\mathcal{E}_{p'})^* - (\mathcal{P}_p)^*\mathcal{E}_{p'}]. \tag{3.23}$$

Before we go on to reformulating the above equation for the propagation of light, we will use our expression for the tensorial coupling density matrix elements to obtain the frequency-dependent electric susceptibility-tensor, $\chi_{mm'}$. The susceptibility describes the polarization-response of the medium to the electric field(34)

$$P_m(s,t) = \frac{1}{\sqrt{2\pi}}\sum_{m'}\int d\omega\ \chi_{mm'}(\omega)E_{m'}(\omega)e^{-i\omega(t-s/c)}. \tag{3.24}$$

We can use the relation between the electric susceptibility-tensor, the polarization field and the electric field, to rewrite the expression for the propagation of radiation that we found in Eq. (3.23). We will treat the transfer of polarized maser radiation in a similar manner as Ref. (34), where propagation of maser radiation is described in terms of the frequency-dependent Stokes parameters $I(\omega)$, $Q(\omega)$, $V(\omega)$ and $U(\omega)$ as

$$\frac{d}{ds}\begin{pmatrix} I(\omega) \\ Q(\omega) \\ U(\omega) \\ V(\omega) \end{pmatrix} = \begin{pmatrix} A & B & F & C \\ B & A & E & G \\ F & -E & A & D \\ C & -G & -D & A \end{pmatrix}\begin{pmatrix} I(\omega) \\ Q(\omega) \\ U(\omega) \\ V(\omega) \end{pmatrix}, \tag{3.25}$$

where the frequency-dependent propagation elements can be described in terms of the susceptibilities(34)

$$A(\omega) = \frac{-2\pi\omega}{c}\left(\mathrm{Im}\left[\chi_{++}\right] + \mathrm{Im}\left[\chi_{--}\right]\right), \tag{3.26a}$$

$$B(\omega) = \frac{2\pi\omega}{c}\left(\mathrm{Im}\left[\chi_{+-}\right] + \mathrm{Im}\left[\chi_{-+}\right]\right), \tag{3.26b}$$

$$C(\omega) = \frac{2\pi\omega}{c}\left(\mathrm{Im}\left[\chi_{++}\right] - \mathrm{Im}\left[\chi_{--}\right]\right), \tag{3.26c}$$

$$D(\omega) = \frac{-2\pi\omega}{c}\left(\mathrm{Re}\left[\chi_{+-}\right] + \mathrm{Re}\left[\chi_{+-}\right]\right), \tag{3.26d}$$

$$E(\omega) = \frac{-2\pi\omega}{c}\left(\mathrm{Re}\left[\chi_{++}\right] + \mathrm{Re}\left[\chi_{--}\right]\right), \tag{3.26e}$$

$$F(\omega) = \frac{-2\pi\omega}{c}\left(\mathrm{Re}\left[\chi_{+-}\right] - \mathrm{Re}\left[\chi_{-+}\right]\right), \tag{3.26f}$$

$$G(\omega) = \frac{2\pi\omega}{c}\left(\mathrm{Im}\left[\chi_{+-}\right] - \mathrm{Im}\left[\chi_{-+}\right]\right). \tag{3.26g}$$

The electric susceptibility-tensor can be related to the state populations, because the polarization of the medium, P_m, can be expressed as(34)

$$P_m(s,t) \simeq 2\sum_{ab}\int dv \rho_{ab} d_m^{ab}. \tag{3.27}$$

We use the expression from Eq. (3.24) and equate them to Eq. (3.27), while using Eq. (3.7) for the populations, so that we can express the electric susceptibility tensor-elements in terms of the state populations. Consequently filling this in

in Eq. 3.26 yields

$$A(\omega) = \frac{-\pi\omega}{c}\sum_{ab}\int dv \left[\sum_{b'}\langle\rho_{b'b}(\gamma_+^{ab}+\gamma_-^{ab'})\rangle\,\delta_I^{ab,ab'} - \sum_{a'}\langle\rho_{aa'}(\gamma_+^{ab}+\gamma_-^{ab'})\rangle\,\delta_I^{ab,a'b}\right], \tag{3.28a}$$

$$B(\omega) = \frac{\pi\omega}{c}\sum_{ab}\int dv \left[\sum_{b'}\langle\rho_{b'b}(\gamma_+^{ab}+\gamma_-^{ab'})\rangle\,\delta_Q^{ab,ab'} - \sum_{a'}\langle\rho_{aa'}(\gamma_+^{ab}+\gamma_-^{ab'})\rangle\,\delta_Q^{ab,a'b}\right], \tag{3.28b}$$

$$C(\omega) = \frac{-\pi\omega}{c}\sum_{ab}\int dv \left[\sum_{b'}\langle\rho_{b'b}(\gamma_+^{ab}+\gamma_-^{ab'})\rangle\,\delta_V^{ab,ab'} - \sum_{a'}\langle\rho_{aa'}(\gamma_+^{ab}+\gamma_-^{ab'})\rangle\,\delta_V^{ab,a'b}\right], \tag{3.28c}$$

$$D(\omega) = \frac{-i\pi\omega}{c}\sum_{ab}\int dv \left[\sum_{b'}\langle\rho_{b'b}(\gamma_+^{ab}-\gamma_-^{ab'})\rangle\,\delta_Q^{ab,ab'} - \sum_{a'}\langle\rho_{aa'}(\gamma_+^{ab}-\gamma_-^{ab'})\rangle\,\delta_Q^{ab,a'b}\right], \tag{3.28d}$$

$$E(\omega) = \frac{i\pi\omega}{c}\sum_{ab}\int dv \left[\sum_{b'}\langle\rho_{b'b}(\gamma_+^{ab}-\gamma_-^{ab'})\rangle\,\delta_V^{ab,ab'} - \sum_{a'}\langle\rho_{aa'}(\gamma_+^{ab}-\gamma_-^{ab'})\rangle\,\delta_V^{ab,a'b}\right], \tag{3.28e}$$

$$F(\omega) = \frac{i\pi\omega}{c}\sum_{ab}\int dv \left[\sum_{b'}\langle\rho_{b'b}(\gamma_+^{ab}+\gamma_-^{ab'})\rangle\,\delta_U^{ab,ab'} - \sum_{a'}\langle\rho_{aa'}(\gamma_+^{ab}+\gamma_-^{ab'})\rangle\,\delta_U^{ab,a'b}\right], \tag{3.28f}$$

$$G(\omega) = \frac{-\pi\omega}{c}\sum_{ab}\int dv \left[\sum_{b'}\langle\rho_{b'b}(\gamma_+^{ab}+\gamma_-^{ab'})\rangle\,\delta_U^{ab,ab'} - \sum_{a'}\langle\rho_{aa'}(\gamma_+^{ab}-\gamma_-^{ab'})\rangle\,\delta_U^{ab,a'b}\right]. \tag{3.28g}$$

The tight relation between the molecular states and the feed to the radiation field is reflected also in these equations, as again, the radiative coupling between the two states is represented by the δ-operators.

Numerical simulation of maser-polarization propagation can be made using this formalism, by (i) self-consistenly computing the state-populations for a given radiation-field, with the use of Eq. (3.12) and (ii) computing the propagation coefficients, using Eq. (3.28) and subsequently propagating the radiation field using Eq. (3.25). The initial radiation field may be black-body radiation, and the initial guess for the state-populations $\sim \Lambda/\Gamma$. Numerical simulations have been carried out and reported in a number of publications(34; 43; 35). The advantage of these numerical simulations is that any rate of stimulated emission of the maser can be investigated—not only the unsaturated and saturated

regimes. The formalism can be expanded to also include multiple hyperfine transitions within a rotational line(35).
This section has been concerned with the theory of polarization of maser radiation by a magnetic field. In the following, we will discuss the polarization of maser radiation by alternative mechanism.

3.2 Alternative polarization mechanisms

There is the possibility that the polarization of the maser is induced by a mechanism that requires no magnetic field, or, a very small one. We will discuss some of the plausible mechanisms that can induce polarization in the maser radiation, and afterwards, comment on the possibility of methanol maser radiation having an induced or enhanced polarization by some of these alternative polarization mechanisms.

3.2.1 Co-propagating maser-rays

It can happen that two building-up maser-rays intersect. If these maser-rays are appreciably saturated, they will introduce a growth of a certain polarization in one-and-another, because a preferred direction is now present in the propagation of the maser(44). Numerical simulations(45) show that, indeed, linear polarization arises as the result of the competition between intersecting rays of saturated masers. But this polarization mechanism cannot explain masers with a polarization higher than $1/3$, nor can it explain circular polarization, without invoking the presence of a magnetic field that spectrally decouples the different types of transitions.

3.2.2 Anisotropic pumping

The excitation of the maser is not necessarily isotropic. Directional, external fields (like a magnetic field) can orient the masing species, provided the interaction with the external field is at least of the same magnitude as the molecules coupling to the maser radiation field. Suppose that a central stellar object emits the pumping radiation, and a magnetic field defines the preferred direction of the maser-molecule. The pumping radiation will have a certain direction compared to the preferred direction of the molecule, i.e. it will be anisotropic. This anisotropy enhances the linear polarization in the masing transitions significantly up to 100%, and it will also enhance the circular polarization greatly(46; 33; 47). One should note that, as long as $g\Omega >> R, \Gamma$, the linear polarization will be directed either parallel, or perpendicular to the projected direction of the magnetic field as seen by the observer, but in the presence of anisotropic

pumping, the polarization flip at the magic angle ($\sim 54.7^o$), as expected from the theory of Ref. (32), gets shifted, depending on the type of anisotropy.
Already small fractions of anisotropy in the pumping, drastically increase the polarization, both linear and circular, of the emission(35). This means, also for a combined radiative and collisional pumping mechanism, the anisotropic nature of the radiative pumping will be strongly reflected in the signal. Incoming polarized radiation, will also increase the maser-polarization drastically(35).

3.2.3 Dichroic unsaturated masers

A more recent attempt in trying to explain high degrees of linear polarization, investigates dichroic unsaturated masers(48). Dichroic in this sense, means a population inversion in the state-polarizations, rather than the average populations, and thus a polarized masing. For a non-appreciable magnetic environment, they find that the anisotropic radiation from a central stellar object, introduces a polarization in the state-populations. This polarization is assumed to remain stable, as collisional de-polarization is assumed to be negligible because of the low densities. Radiative decay of the excited states will lead to the polarized population inversion, that causes a linear polarization for unsaturated masers, that is directed tangentially to the central star(48).

3.2.4 Anisotropic resonant scattering

Radiation can be linearly polarized by, for instance, the Goldreich-Kylafis effect(49; 50), or from a maser-polarization effect. The radiation can be scattered in a foreground cloud, that is permeated by a magnetic field, which causes anisotropy in the scattering. By scattering the radiation, via resonant scattering, the linearly polarized radiation(51)

$$|\psi\rangle = \alpha_0 |n_{||}\rangle + \beta_0 |n_\perp\rangle \,, \tag{3.29}$$

will, after the scattering event, be rotated to

$$|\psi'\rangle = \alpha_0 e^{i\phi} |n_{||}\rangle + \beta_0 |n_\perp\rangle \,, \tag{3.30}$$

where the re-scattered radiation has a circularly polarized component.
Resonant scattering is the process of scattering of a photon, by excitation of a particle from state $|a\rangle$ to a virtual state $|b\rangle$, to be subsequently demoted again to $|a\rangle$, re-emitting the photon that was initially absorbed. In contrast to absorption or (stimulated) emission, this is a process that affects the state-population only in second-order—and leaves the total population (rank-0 population) invariant, but not the state-polarizations. The scattering amplitude can be expressed as

$$S_{a\to a',\ell} = -i\frac{T}{L^3}\frac{1}{2\epsilon_0\hbar}\sqrt{\frac{nn'}{\omega'\omega}}\sum_b \frac{\omega_{ba'}\omega_{ba}\,\langle a'|\hat{d}\cdot\epsilon_\ell|b\rangle\,\langle b|\hat{d}\cdot\epsilon_\ell|a\rangle}{\omega_{ba}-\omega-i\gamma_{ba}}, \tag{3.31}$$

for a scattering reaction from state a to a'. The incident and scattered photon number and frequency are n, n', ω and ω', ω_{ba} is the energy difference between state b and a, divided by the reduced Planck constant: $\hbar$. The quantities T and L^3 are the interaction time and the fiducial volume of the quantization of the radiation field. The induced phase-shift from a resonant scattering event is described by

$$\phi = Im\left(S_{a\rightarrow a',||} - S_{a\rightarrow a',\perp}\right). \tag{3.32}$$

Because of the Zeeman splitting, the states are not degenerate, and have slightly different resonance frequencies between each other. This will naturally yield an antisymmetric, S-formed, shape of the scattering angle $\phi(\omega)$-function, provided incoming linearly polarization is symmetric. Using these principles, the circular polarization fraction of the CO-lines(51; 52) and SiO maser lines(53), can be explained, already at very low magnetic fields.

Some problems for this theory might arise because of its simplified approach to the consideration of molecular states. In the numerical calculations, the inelastic resonant scattering routes are neglected, and the problem is effectively reduced to a $J = 0 - 1 - 0$ scattering event. This will greatly enhance the polarization fraction, which can also be seen in the polarization trends for SiO masers—low J-transitions are more polarized. To accurately asses the impact of the assumption in the framework of the resonant anisotropic theory, simulations have to be done in a rigorous manner, not neglecting any channel.

The resonant scattering effect comes up under second-order perturbation theory, and affects the populations of the two states. If one follows the theory as presented in section 3.1, the populations are computed variationally, within the approximation of steady state, and should therefore also account for second order effects. In fact, second-order population shifts can ben derived from the outset of the maser-polarization theory. The approximations used in section 3.1 do not affect the second-order populations in a way that the effects of resonant anisotropic scattering as described above are overlooked.

3.3 Alternative maser polarization and methanol

Co-propagating maser rays It cannot be ruled out that some of the methanol masers that we observe, have arisen in a maser-region where other maser rays were co-propagating. In these case, enhanced polarization should be apparent. However, if this effect was appreciable in many cases, stronger degrees, up on to 33%, of, mainly, linear polarization would have to be observed in the methanol maser signals. Such degrees have hitherto not been observed. Moreover, in the sample of methanol maser observations, the polarization fractions have been rather low, and strong outliers have yet to be discovered. So, these

co-propagating maser rays are either not present, or have a negligable effect on methanol maser polarization.

Anisotropic pumping Considering anisotropic pumping, it is interesting to compare the cases of radiative pumping for SiO masers and class II methanol masers. In SiO masers, the pumping-radiation comes directly from the stellar object, and thus from one certain direction. For molecular states that are aligned with the magnetic field, this causes anisotropy in the pumping. This is in contrast with class II methanol masers, that are pumped by stellar radiation that is re-scattered by dust. Thus, the pumping radiation for class II methanol masers is isotropic. These mechanisms are reflected in the maser polarization, as SiO masers are often found to be highly polarized in contrast to methanol class II masers, where only a small fraction of the radiation is polarized.
Class I methanol masers are pumped collisionaly. A collision is isotropic because the quantization axis of the collision is not influenced by the magnetic field, as the Zeeman interactions in the collisional partners are negligible with respect to the collision energies. It is though a possibility that radiative relaxation after the collisional pumping event, has a preferred direction because of strongly angularly varying optical depths around the maser-region. However, this seems unlikely as the methanol-lines are optically thin in the shocked outflow-regions these masers occur in.

Di-chroic unsaturated masers For methanol, as discussed above, the pumping radiation is not anisotropic in its nature. Also, methanol maser polarization observations rarely include unsaturated masers. This mechanism can be ruled out to explain methanol maser polarization.

Anisotropic resonant scattering Anisotropic resonant scattering requires a foreground cloud of methanol molecules between the observer and the maser area to re-scatter, already linearly polarized radiation, to circularly polarized radation. Linear polarization of the methanol maser should be induced either by an alternative polarization mechanism, which we have seen, is unlikely for methanol, or by polarization of a magnetic field. In the latter case, polarization through magnetic fields already induces circular polarization; which renders this theory irrelevant for methanol masers, because it does not consider this case. Also, 75% of the methanol masers for a statistically complete sample was found to be circularly polarized(54). For such a large fraction of the observations, the presence of a foreground cloud is unlikely to occur.

Chapter 4

METHANOL MASER OBSERVATIONS

Single dish The first methanol maser was discovered in Orion-KL at the $J_2 - J_1$ E transitions around 25 GHz(55; 56). It was not until 13 years later that two new methanol masers, $9_2 - 10_1$ A^+ at 23 GHz and $2_1 - 3_0$ E at 20 GHz, towards a compact HII-region at W3(OH) were detected(57; 58). These were followed by discoveries of the masers $4_{-1} - 3_0$ E, $7_0 - 6_1 A^+$ at 36 GHz and 44 GHz(59) and the very strong $2_0 - 3_{-1}$ E maser at 12.2 GHz(60). The most widespread and strongest methanol maser line, the $5_1 - 6_0$ A^+ transition at 6.7 GHz, was detected in 1991(61). It was found to occur exclusively at the sites of massive star formation(62; 17; 63). The ubiquitousness, strength, and stability of this maser makes it the most well-studied masers. According to the established maser-timeline of the massive star-formation evolution, for the 6.7 GHz methanol maser, the traced sample of high-mass star forming regions will most likely trace the late stages of the class II methanol maser times(64; 65; 66) .

Table 4.1 lists all of the hitherto detected polarized methanol maser-transitions. As can be read from the table, a distinction between two classes of masers can be made—two sets of transitions, that do not occur as a maser together, and are found in different regions(60; 67). Class I masers and Class II masers. Class I masers can be easily understood as collisionally pumped (see section 2.2), and are therefore believed to occur in the shocked regions of a molecular outflow. However, the pumping mechanism of Class II masers is a lot more complex. It was not until more advanced numerical modeling that the pumping mechanism of Class II methanol masers could be understood(28; 31). Class II masers are pumped through infrared radiative excitation of higher torsionally states (section 2.2). The infrared radiation is likely coming from surrounding dust that re-emits stellar UV-radiation at infrared wavelengths. Class II masers are found towards HII regions, and occur together with OH-masers.

Single dish observations can only discern association between maser-transitions on a spectral level. Position association can only be done to a level of very low

resolution. Although this proved enough to distinct the two classes of methanol masers, an analysis with higher angular resolution could discern how closely associated in position maser-transitions within a class are, and how they are positioned with respect to the protostar. They would provide a clearer picture of the environments these masers occur in. These type of high-resolution observations can be done by using interferometric techniques.

Interferometry Early VLBI observations of the class II 6.7 GHz and 12.2 GHz masers towards high-mass star forming regions revealed that a large fraction of them occur in a linear structure around the central star, with a velocity structure that suggests they are situated in an accretion disk around the forming (proto-)star(80; 81). More complex structures suggest the masers to occur behind a shock front, or the masers originating from the interaction between collimated biconical outflows with the surrounding medium(82; 83).
An even better image of the occurring masers can be obtained by probing the gas kinematics of the condensation in which the maser is formed. From multiple epoch observations, one can follow the motion of the maser cloudlet in the plane of the sky. Combined with the spectral velocity of the maser cloudlet, tracing the velocity along the line-of-sight, this entails enough information to construct the three-dimensional proper motion vector. These observations lead to further support of the 6.7 GHz masers occurring in an ordered structure around the protostar(84; 85; 86; 87; 88). However, these investigations have only been done for a limited number of sources ($\sim$10). A number of structures around the protostar have been observed by maser-proper motion analyses. Apart from an accreting disk, where the masers trace infalling gas, also a dusty torus has been observed where the infall has been halted(89).
Interferometric observations of class I masers place them on the outer parts of the molecular outflow of the central young stellar object(90; 91). It is the shocked, swept-up material in these regions, that provide the necessary conditions for the class I methanol masers to form(92). High resolution VLBI imaging of the 44 GHz methanol maser suggest that the masers have compact components with the sizes of a few tens of AU(93). No proper motion analysis of this class of methanol masers have been executed. More thorough surveys of the 36 GHz and 44 GHz class I methanol masers(92), provide an alternative association as the outflow-shocks, namely the shocks coming from an expanding HII region. In general, less specific conditions are required for the formation of class I masers with respect to the class II masers. They can be found towards lower and intermediate mass stars(94), as well as in regions of supernova remnants(95).
Magnetic fields, as outlined in Chapter 3 of this thesis, will partially polarize the maser radiation coming from methanol. For the stronger masers, this polarization can be observed, which will indicate the magnetic field. Several of these measurements have already been done, which is outlined in the following sec-

tion.

Methanol maser polarization observations Early observations of the class II 12.2 GHz methanol maser revealed that these masers are partially polarized(75). For the five strongest sources in their sample, Ref. (75) reports three sources to be polarized under 3% and the two other sources to be polarized up to 10%. Also, a tentative observation of circular polarization was made(75). The first full polarization observations of the class II 6.7 GHz maser were reported to have high linear polarization fractions, up to 10%, and relatively low circular polarization fractions up to 1.5%.(68). Later, observation of 24 bright 6.7 GHz maser sources revealed 17 of them to be circularly polarized(69). The circular polarization is ascribed as to be due to the Zeeman effect. These measurements were expanded to a statistically complete sample where 75% of the sources appear to be circularly polarized(54). Ref. (79) investigated the polarization properties of 5, both class I and class II, methanol maser lines between 84 GHz and 157 GHz. They find significant linear polarization for all sources, and present tentative detections of the circular polarization of some of the masers.
By using the techniques of VLBI, the full polarization of individual maser spots could be determined. This was first done for W3(OH)(96), and the polarization vectors of the masers indicated an ordered magnetic field, that is also dynamically important. The sample of high-mass star-forming regions investigated for their magnetic field through methanol 6.7 GHz maser-polarization has been expanded since(70; 71; 72; 73; 74). All of these observations seem to reinforce the hypothesis of the presence of an orderly and strong magnetic field during the early stages of star-formation.
EVLA observations have also revealed the presence of strong circular polarization in the 36 GHz and 44 GHz class I methanol masers.
The interpretation of these measurements has been limited to the linear polarization, indicating only the projected magnetic field direction at the maser region. The interpretation of the circular maser-polarization for the magnetic field strength, has remained tentative due to lack of data on the Zeeman-parameters of methanol. This means that the inference of a dynamically important magnetic field remains subject to confirmation.

Table 4.1

Transition	Frequency (MHz)	Class	Polarization	Ref.
$5_1 \rightarrow 6_0\ A^+$	6668.5192(8)	II	C/L	(68; 69; 70; 71; 72; 73; 54; 74)
$2_0 \rightarrow 3_{-1}\ E$	12178.597(4)	II	(C)/L	(75)
$4_{-1} \rightarrow 3_0\ E$	36169.24(10)	I	C/L	(76)
$7_0 \rightarrow 6_1\ A^+$	44069.49(10)	I	C/L	(77; 78)
$5_{-1} \rightarrow 4_0\ E$	84521.169(10)	I	L	(79)
$8_0 \rightarrow 7_1\ A^+$	95169.44(10)	I	L	(79; 78)
$3_1 \rightarrow 4_0\ A^+$	107013.85(10)	II	L	(79)
$6_{-1} \rightarrow 5_0\ E$	132890.790	I	(C)/L	(79)
$6_0 \rightarrow 6_{-1}\ E$	157048.62(10)	II	L	(79)

Chapter 5

OUTLOOK

5.1 Hyperfine-resolved pumping

One of the results presented in this thesis is that the Landé g-factors of the different hyperfine components of each methanol torsion-rotation transition vary over a large range of values. It is therefore important to know the populations of the individual hyperfine levels of the torsion-rotation states involved in the methanol maser action. This maser action is preceded by collisional and radiative (de-)excitation of higher torsion-rotation levels. In paper II, we derive a formalism to estimate relative hyperfine-state-specific collisional and radiational (de-)excitation rate coefficients from the torsion-rotation rate coefficients. We have started a collaboration to model methanol's maser excitation, using the hyperfine resolved rate coefficients computed from the theory presented in Paper II. By including hyperfine effects, the dimensionality of the problem is multiplied by 8 with respect to the usual modeling, only accounting for torsion-rotation levels. To model class II methanol masers, one needs to involve the radiative transitions between the levels of the first three torsional states(31). To also include hyperfine-levels in these models, would not be computationally feasible. The modeling of class I masers however, is generally computationally easier, and they can be accurately modelled without involving higher torsional states(97). One of the lower lying class I maser transitions that also is observed as being magnetically polarized, is the $4_{-1} - 3_0\ E$ torsion-rotation transition at 36 GHz. Preliminary calculations reveal that this maser can be accurately modelled by including only the first 60 torsion-rotation levels(98). In the near future, we will model the excitation of this maser-line with a hyperfine resolved level structure and transitions. By studying the relative propensities of the pumping specific to the individual hyperfine levels of the torsion-rotation states in the maser-line, we hope to investigate quantitatively the effects of hyperfine preferred pumping.

5.2 SiO maser observations in AGB stars

Around O-rich AGB-stars we find SiO masers. The pulsation of the AGB-star pumps a lot of mechanical energy in the atmosphere, that is already weakly bound by gravity because of the size of the core and stellar envelope ($\sim$a.u.). Far out into the atmosphere, at lower temperatures, dust grains can condense. The low gravitational binding, the mechanical energy from the pulsations, and the radiation pressure on dust grains results in a strong, but slow, wind that makes the star lose a large part of its mass.

This mass-loss mechanism is essentially spherically symmetric. However, this cannot be unified with the very asymmetric Planetary Nebulae (PNe) that form a large part of the ensemble of observed PNe. One of the theories that might explain the observed asymmetries is a magnetic field. The magnetic field could be created by a dynamo mechanism, that results in a magnetic field that launches a collimated outflow jet(99). Water masers have been observed that trace such outflows(100), and were confirmed to trace a poloidal magnetic field, strong enough to shape the outflow jet(96). SiO masers have also been observed as tracing an orderly magnetic field(101). Combined polarization and trajectory analysis suggest the magnetic field traced by these masers to be of dynamical importance(102; 103). An alternative explanation for asymmetries in PNe, could be given by interaction of the AGB star with a binary companion(104).

SiO masers occur in ring-like structure at $2-4$ stellar radii around the central star(105). Their unique position and structure, and occurrence just before the dust shell, that catches the radiative pressure to drive the wind, makes them a potentially very useable probe to explain the transition from the AGB-phase to the asymmetric PNe phase. By SiO maser polarization observations, one can determine the magnetic field morphology and strength in a unique position around the central star.

Single dish observations Initial SiO polarization observations in evolved stars were carried out reported in Ref. (106). For these observations of the $v=1$ $J=2-1$ transition in full polarization mode towards a small sample of evolved stars, linear polarization was detected consistently and at about $15-30\%$ of the total intensity. Circular polarization was not only tentatively detected towards one source. It was not until the SiO $v=1,\ J=1-0$ maser transition was observed towards a sample of evolved stars, that a significant circular polarization fraction could be detected in the maser emission(107). From these observations, for some sources, a magnetic field as high as 100 G was inferred. More recent single dish $v=1$, $J=2-1$ full-polarization line observations towards 57 evolved stars reveal varying fractional linear (0-70%) and circular (0-43%) polarization(103).

Interferometric observations The VLBI intensity measurements of SiO masers revealed a ring like structure around the host stellar object(105). The polarization of these SiO masers, $v = 1,\ J = 1 - 0$, in high angular resolution was first investigated with the VLBA for TX Cam(101; 102; 108), and the observations are summarized in Figure 5.1. The general polarization morphology is broadly tangential over significant portions of the inner part of the shell boundary—polarization angles show an ordered magnetic field, that is most likely radial. The fractional linear polarization is mostly found to be around 25%, but polarizations approaching 100% were measured for some components. Circular polarization as high as $30 - 40\%$ has been measured, but the median circular polarization fraction is about $3 - 5\%$. Observations of other AGB stars have revealed that the tangentially oriented polarization vectors are predominant in the SiO maser rings of several stars. This leads to the conclusion that a radial magnetic field is present for these stars(109; 110). However, it is absolutely not a general observations that the polarization vectors are tangential(109; 110), and more often, a less clear ordening in the polarization vectors is observed. Also, it is shown, that over the course of the observation epochs, linear polarization fractions strongly vary.

Numerical modeling of maser polarization Generally, SiO maser observations are interpreted using the idealized theories of Goldreich, Keeley and Kwan(32) and Elitzur(39). There are many possibilities of perturbation of the idealized conditions, but these are generally only qualitatively included in the analysis. Watson and coworkers(34; 47; 33; 111) have investigated departures of idealized maser-polarization conditions numerically in many cases. However, their results are only qualitatively accounted for in the interpretation of maser-polarization observations. It would be of high interest to build a numerical model that can incorporate and accommodate the relevant departures from ideal polarization of maser sources, so that a more stringent and quantitative estimation can be made on the environments where the polarized masers form.

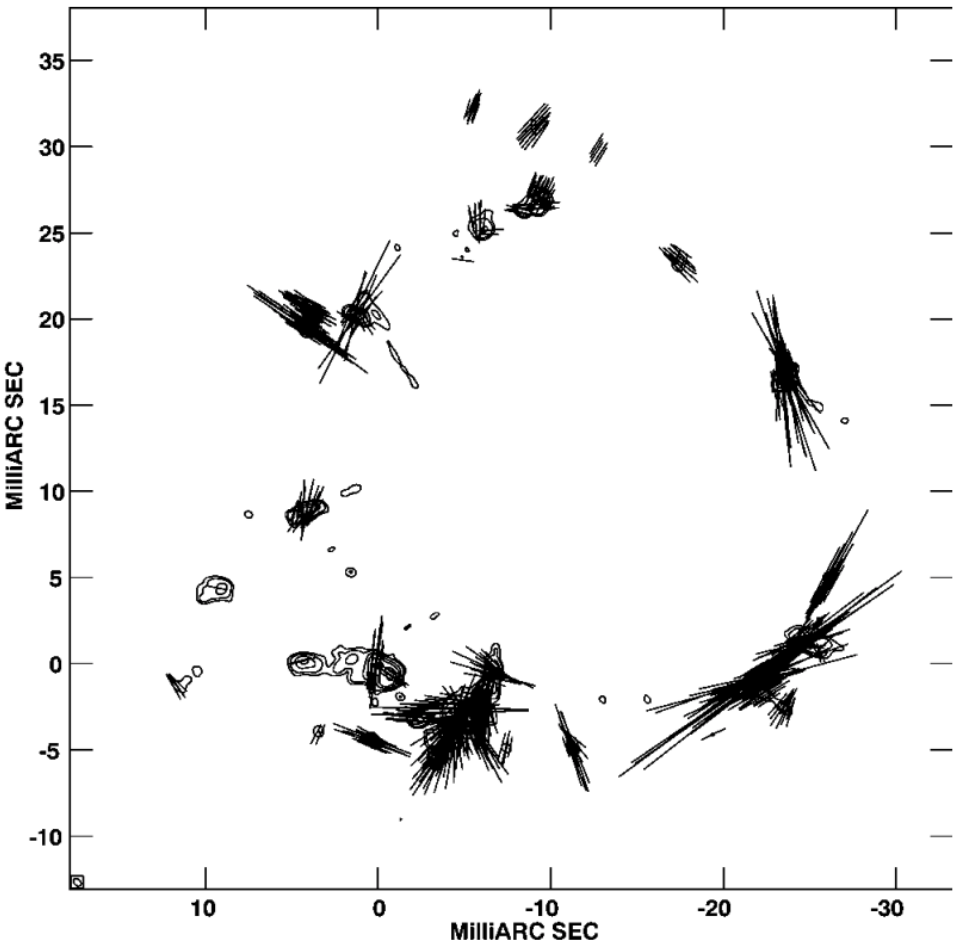

Fig. 5.1: The VLBI map of the polarization of the SiO $v = 1$ $J = 1 - 0$ maser emission, overlayed on the total intensity map of the SiO $v = 1$ $J = 1 - 0$ maser emission toward the Mira variable TX Cam. Figure taken from Ref. (101).

Chapter 6

INTRODUCTION TO PAPERS

In the introduction, it is stressed a number of times, that, although there exist a sizable sample of methanol maser polarization observations, and that these measurements hold information on the magnetic field strength and morphology, that is important in developing a theory of massive star formation, the interpretation of these measurements has remained impossible because of the absence of information on methanols interaction with a weak magnetic field—the Zeeman parameters. This thesis present two papers that are concerned with methanols magnetic interactions and present the Zeeman parameters of methanol.

Hyperfine interactions and internal rotation in methanol Methanols internal magnetic interactions—the hyperfine interactions—are one order of magnitude greater than the Zeeman interactions at fields of about ~ 10 mG. A big contribution to methanols Zeeman effect comes from the nuclear spins—having a structure defined by the hyperfine structure. This means that in order to make a model on methanols Zeemen interactions, we must first consider its hyperfine structure. There has been some experimental laboratory observations of methanols hyperfine structure(21; 20), but a feasable interpretation remained elusive. In this paper, we show that the formalism used for the interpretation, accounted for Thomas-precession interactions, that are actually negligable. Also, we show that the formalism makes use of a torsional operator that is not unifiable with the torsional operator of the model on methanols torsion-rotation structure. We use our improved model, and a strategy, where not the known (from quantum-chemical simulations) dipole-dipole and spin-rotation tensors are fitted to the experimental data, but only the unknown spin-torsion tensor are fitted to the experimental data. We present a fit of the data, and confirm that, indeed, the electronic contributions to the spin-torsion tensors, as expected, are adverse to the nuclear contributions to the spin-torsion tensors.

Characterization of methanol as a magnetic field tracer in star-forming regions In order to compute the Zeeman parameters of methanol, the interactions with an external magnetic field have to be added to the model on methanols hyperfine structure. The interactions of an external magnetic field with methanols protons, as well as the interaction with its rotation, can be computed quantum chemically, and are presented in this paper. Conversely, the interaction of an external magnetic field with methanols torsion, is estimated from previous experiments to similar molecules and a Mulliken population analysis. We present the mathematical formalism to properly compute the Zeeman parameters of each hyperfine transition of any torsion-rotation line. Because the individual hyperfine transition lie so close to each other within each torsion-rotation line, we cannot discern which hyperfine transition is preferably masing. To tackle this problem, we present a number of ways hyperfine-preferred pumping of the maser is possible, and from these mechanisms, qualitatively deduce which hyperfine transition is dominant in the maser action. With this, we can interpret the large sample of circular-polarization observations of methanol masers, and estimate the magnetic field strength in methanol maser regions, to be dynamically important.

BIBLIOGRAPHY

[1] A. Einstein, "Zur quantentheorie der strahlung," *Phys. Z.*, vol. 18, pp. 121–128, 1917.

[2] R. Loudon, *The quantum theory of light*. OUP Oxford, 2000.

[3] J. P. Gordon, H. J. Zeiger, and C. H. Townes, "Molecular microwave oscillator and new hyperfine structure in the microwave spectrum of n h 3," *Phys. Rev.*, vol. 95, no. 1, p. 282, 1954.

[4] J. P. Gordon, H. J. Zeiger, and C. H. Townes, "The maserânew type of microwave amplifier, frequency standard, and spectrometer," *Phys. Rev.*, vol. 99, no. 4, p. 1264, 1955.

[5] J. C. Tan, M. T. Beltrán, P. Caselli, F. Fontani, A. Fuente, M. R. Krumholz, C. F. McKee, and A. Stolte, "Massive star formation," *Protostars and Planets VI*, pp. 149–172, 2014.

[6] F. H. Shu, "Self-similar collapse of isothermal spheres and star formation," *Astrophys. J.*, vol. 214, pp. 488–497, 1977.

[7] C. F. McKee and J. C. Tan, "The formation of massive stars from turbulent cores," *Astrophys. J.*, vol. 585, no. 2, p. 850, 2003.

[8] C. F. McKee and J. C. Tan, "Massive star formation in 100,000 years from turbulent and pressurized molecular clouds," *Nature*, vol. 416, no. 6876, pp. 59–61, 2002.

[9] M. R. Krumholz and C. F. McKee, "A minimum column density of 1 g cm-2 for massive star formation," *Nature*, vol. 451, no. 7182, pp. 1082–1084, 2008.

[10] M. W. Kunz and T. C. Mouschovias, "The nonisothermal stage of magnetic star formation. i. formulation of the problem and method of solution," *Astrophys. J.*, vol. 693, no. 2, p. 1895, 2009.

[11] J. C. Tan, S. Kong, M. J. Butler, P. Caselli, and F. Fontani, "The dynamics of massive starless cores with alma," *Astrophys. J.*, vol. 779, no. 2, p. 96, 2013.

[12] I. Bonnell, M. Bate, C. Clarke, and J. Pringle, "Competitive accretion in embedded stellar clusters," *Monthly Notices of the Royal Astronomical Society*, vol. 323, no. 4, pp. 785–794, 2001.

[13] I. A. Bonnell and M. R. Bate, "Star formation through gravitational collapse and competitive accretion," *Monthly Notices of the Royal Astronomical Society*, vol. 370, no. 1, pp. 488–494, 2006.

[14] J. Hougen, I. Kleiner, and M. Godefroid, "Selection rules and intensity calculations for a Cs asymmetric top molecule containing a methyl group internal rotor," *J. Mol. Spectrosc.*, vol. 163, no. 2, pp. 559 – 586, 1994.

[15] P. Jansen, L.-H. Xu, I. Kleiner, W. Ubachs, and H. L. Bethlem, "Methanol as a sensitive probe for spatial and temporal variations of the proton-to-electron mass ratio," *Phys. Rev. Lett.*, vol. 106, p. 100801, 2011.

[16] D. M. Brink and G. R. Satchler, *Angular Momentum*. Oxford: Clarendon, third ed., 1993.

[17] L.-H. Xu, J. Fisher, R. M. Lees, H. Y. Shi, J. T. Hougen, J. C. Pearson, B. J. Drouin, G. A. Blake, and R. Braakman, "Torsion-rotation global analysis of the first three torsional states (v_t = 0, 1, 2) and terahertz database for methanol," *J. Mol. Spectr.*, vol. 251, pp. 305–313, 2008.

[18] J. Heuvel and A. Dymanus, "Hyperfine structure in internal rotor molecules," *J. Mol. Spectrosc.*, vol. 47, no. 3, pp. 363 – 387, 1973.

[19] J. Stanton, J. Gauss, H. M.E., and P. Szalay, "CFOUR, Coupled-Cluster techniques for Computational Chemistry." http://www.cfour.de.

[20] L. Coudert, C. Gutlé, T. Huet, J.-U. Grabow, and S. Levshakov, "Spin-torsion effects in the hyperfine structure of methanol," *J. Chem. Phys.*, vol. 143, no. 4, p. 044304, 2015.

[21] J. Heuvel and A. Dymanus, "Hyperfine structure of CH_3OH," *J. Mol. Spectrosc.*, vol. 45, no. 2, pp. 282 – 292, 1973.

[22] L. Engelbrecht, D. Sutter, and H. Dreizier, "Zeeman effect of molecules with low methyl barriers. I. Nitromethane," *Z. Naturforsch. A*, vol. 28, no. 5, pp. 709–713, 1973.

[23] L. Engelbrecht, *Der Rotations-Zeemaneffekt bei Molekülen mit schwach behinderter interner Rotation*. PhD thesis, University of Kiel, 1975.

[24] E. Herbst and E. F. Van Dishoeck, "Complex organic interstellar molecules," *Annual Review of Astronomy and Astrophysics*, vol. 47, pp. 427–480, 2009.

[25] R. Lees and S. Haque, "Microwave double resonance study of collision induced population transfer between levels of interstellar methanol lines," *Canadian Journal of Physics*, vol. 52, no. 22, pp. 2250–2271, 1974.

[26] D. Rabli and D. Flower, "The rotational excitation of methanol by molecular hydrogen," *Mon. Not. R. Astronom. Soc.*, vol. 406, no. 1, pp. 95–101, 2010.

[27] K. Menten, C. Walmsley, C. Henkel, T. Wilson, L. Snyder, J. Hollis, and F. Lovas, "Torsionally excited methanol in hot molecular cloud cores," *Astron. Astrophys.*, vol. 169, pp. 271–280, 1986.

[28] A. Sobolev and S. Deguchi, "Pumping of class 2 methanol masers. 1: The 20-3-1e transition," *Astron. Astrophys.*, vol. 291, pp. 569–576, 1994.

[29] J. Pottage, D. Flower, and S. L. Davis, "The torsional excitation of methanol by helium," *Journal of Physics B: Atomic, Molecular and Optical Physics*, vol. 37, no. 1, p. 165, 2003.

[30] J. Pottage, D. Flower, and S. L. Davis, "The rotational excitation of methanol by para-hydrogen," *Mon. Not. R. Astronom. Soc.*, vol. 352, no. 1, pp. 39–43, 2004.

[31] D. Cragg, A. Sobolev, and P. Godfrey, "Models of class II methanol masers based on improved molecular data," *Mon. Not. R. Astron. Soc.*, vol. 360, no. 2, pp. 533–545, 2005.

[32] P. Goldreich, D. A. Keeley, and J. Y. Kwan, "Astrophysical masers. 11. polarization properties," *Astrophys. J.*, vol. 179, pp. 111–134, 1973.

[33] L. Western and W. Watson, "Linear polarization of astronomical masers and magnetic fields," *Astrophys. J.*, vol. 285, pp. 158–173, 1984.

[34] S. Deguchi and W. D. Watson, "Linearly polarized radiation from astrophysical masers due to magnetic fields when the rate for stimulated emission exceeds the Zeeman frequency," *Astrophys. J.*, vol. 354, pp. 649–659, 1990.

[35] G. E. Nedoluha and W. D. Watson, "Intensity-dependent circular polarization and circumstellar magnetic fields from the observation of sio masers," *Astrophys. J.*, vol. 423, pp. 394–411, 1994.

[36] M. Elitzur, "Polarization of astronomical maser radiation," *The Astrophysical Journal*, vol. 370, pp. 407–418, 1991.

[37] M. Elitzur, "Polarization of astronomical maser radiation. ii. polarization modes and unsaturated growth," *Astrophys. J.*, vol. 416, p. 256, 1993.

[38] M. Elitzur, "Polarization of astronomical maser radiation. iii. arbitrary zeeman splitting and anisotropic pumping," *arXiv preprint astro-ph/9508007*, 1995.

[39] M. Elitzur, "Polarization of astronomical maser radiation. iv. circular polarization profiles," *Astrophys. J.*, vol. 504, no. 1, p. 390, 1998.

[40] W. D. Watson, "Basic theory for polarized, astrophysical maser radiation in a magnetic field," *Astrophys. J.*, vol. 424, pp. L37–L39, 1994.

[41] M. Gray, "A comparison of models of polarized maser emission," *Mon. Not. R. Astronom. Soc.*, vol. 343, no. 2, pp. L33–L35, 2003.

[42] D.-V. TRUNG, "On the theory of astronomical masersâii. polarization of maser radiation," *Mon. Not. R. Astronom. Soc.*, vol. 399, no. 3, pp. 1495–1505, 2009.

[43] G. E. Nedoluha and W. D. Watson, "Spectral line profiles and luminosities of astrophysical water masers," *Astrophys. J.*, vol. 367, pp. L63–L67, 1991.

[44] L. Western and W. Watson, "Transfer of polarized radiation in astronomical masers," *Astrophys. J.*, vol. 268, pp. 849–859, 1983.

[45] L. Western and W. Watson, "Geometrical effects on the emission properties of astronomical masers-linear polarization and apparent sizes," *Astrophys. J.*, vol. 274, pp. 195–209, 1983.

[46] L. Western and W. Watson, "Linear polarization of astronomical masers by anisotropic pumping and its enhancement due to geometry," *Astrophys. J.*, vol. 275, pp. 195–200, 1983.

[47] G. E. Nedoluha and W. D. Watson, "Linearly polarized radiation from astrophysical masers due to magnetic fields of intermediate strength," *Astrophys. J.*, vol. 354, pp. 660–675, 1990.

[48] A. A. Ramos, E. L. DeglâInnocenti, and J. T. Bueno, "Dichroic masers due to radiation anisotropy and the influence of the hanle effect on the circumstellar sio polarization," *Astrophys. J.*, vol. 625, no. 2, pp. 985–995, 2005.

[49] P. Goldreich and N. D. Kylafis, "On mapping the magnetic field direction in molecular clouds by polarization measurements," *Astrophys. J.*, vol. 243, pp. L75–L78, 1981.

[50] P. Goldreich and N. D. Kylafis, "Linear polarization of radio frequency lines in molecular clouds and circumstellar envelopes," *Astrophys. J.*, vol. 253, pp. 606–621, 1982.

[51] M. Houde, T. Hezareh, S. Jones, and F. Rajabi, "Non-zeeman circular polarization of molecular rotational spectral lines," *Astrophys. J.*, vol. 764, no. 1, p. 24, 2013.

[52] T. Hezareh, H. Wiesemeyer, M. Houde, A. Gusdorf, and G. Siringo, "Non-zeeman circular polarization of co rotational lines in snr ic 443," *Astron. Astrophys.*, vol. 558, p. A45, 2013.

[53] M. Houde, "Non-zeeman circular polarization of molecular maser spectral lines," *Astrophys. J.*, vol. 795, no. 1, p. 27, 2014.

[54] Vlemmings, W. H. T., Torres, R. M., and Dodson, R., "Zeeman splitting of 6.7Â GHz methanol masers," *Astron. Astroph.*, vol. 529, p. A95, 2011.

[55] A. Barrett, P. Schwartz, and J. Waters, "Detection of methyl alcohol in orion at a wavelength of˜ 1 centimeter," *Astrophys. J.*, vol. 168, p. L101, 1971.

[56] D. N. Matsakis, M. Wright, C. Townes, W. Welch, A. Cheung, and J. Askne, "An interferometric and multitransitional study of the orion methanol masers," *Astrophys. J.*, vol. 236, pp. 481–491, 1980.

[57] T. Wilson, C. Walmsley, P. Jewell, and L. Snyder, "Detection of a new type of methanol maser," *Astron. Astrophys.*, vol. 134, pp. L7–L10, 1984.

[58] T. Wilson, C. Walmsley, K. Menten, and W. Hermsen, "The discovery of a new masering transition of interstellar methanol," *Astronomy and Astrophysics*, vol. 147, pp. L19–L22, 1985.

[59] M. Morimoto, T. Kanzawa, and M. Ohishi, "New maser lines of methanol," *Astrophys. J.*, vol. 288, pp. L11–L15, 1985.

[60] W. Batrla, H. Matthews, K. Menten, and C. Walmsley, "Detection of strong methanol masers towards galactic h ii regions," *Nature*, vol. 326, no. 6108, pp. 49–51, 1987.

[61] K. M. Menten, "The discovery of a new, very strong, and widespread interstellar methanol maser line," *Astrophys. J.*, vol. 380, pp. L75–L78, 1991.

[62] V. Minier, S. Ellingsen, R. Norris, and R. Booth, "The protostellar mass limit for 6.7 ghz methanol masers-i. a low-mass yso survey," *Astron. Astrophys.*, vol. 403, no. 3, pp. 1095–1100, 2003.

[63] S. Breen, S. Ellingsen, Y. Contreras, J. Green, J. Caswell, J. Stevens, J. Dawson, and M. Voronkov, "Confirmation of the exclusive association between 6.7-ghz methanol masers and high-mass star formation regions," *Mon. Not. R. Astron. Soc.*, vol. 435, no. 1, pp. 524–530, 2013.

[64] S. P. Ellingsen, "A glimpse-based search for 6.7-ghz methanol masers and the lifetime of their spectral features," *Mon. Not. R. Astron. Soc.*, vol. 377, no. 2, pp. 571–583, 2007.

[65] S. Breen, S. Ellingsen, J. Caswell, and B. Lewis, "12.2-ghz methanol masers towards 1.2-mm dust clumps: quantifying high-mass star formation evolutionary schemes," *Mon. Not. R. Astron. Soc.*, vol. 401, no. 4, pp. 2219–2244, 2010.

[66] S. Ellingsen, S. Breen, A. Sobolev, M. Voronkov, J. Caswell, and N. Lo, "37 ghz methanol masers: Horsemen of the apocalypse for the class ii methanol maser phase?," *Astrophys. J.*, vol. 742, no. 2, p. 109, 2011.

[67] K. Menten, "Methanol masers and submillimeter wavelengthwater masers in star-forming regions," in *Atoms, Ions and Molecules: New Results in Spectral Line Astrophysics*, vol. 16, p. 119, 1991.

[68] S. Ellingsen, "Polarization properties of 6.7 ghz methanol masers in ngc6334f," in *Symposium-International Astronomical Union*, vol. 206, pp. 151–154, Cambridge University Press, 2002.

[69] W. H. T. Vlemmings, "A new probe of magnetic fields during high-mass star formation," *Astron. Astroph.*, vol. 484, no. 3, pp. 773–781, 2008.

[70] G. Surcis, W. Vlemmings, R. Dodson, and H. Van Langevelde, "Methanol masers probing the ordered magnetic field of w75n," *Astron. Astrophys.*, vol. 506, no. 2, pp. 757–761, 2009.

[71] G. Surcis, W. Vlemmings, S. Curiel, B. H. Kramer, J. Torrelles, and A. Sarma, "The structure of the magnetic field in the massive star-forming region w75n," *Astron. Astrophys.*, vol. 527, p. A48, 2011.

[72] G. Surcis, W. H. T. Vlemmings, H. J. van Langevelde, and B. Hutawarakorn Kramer, "EVN observations of 6.7 GHz methanol maser polarization in massive star-forming regions," *Astron. Astrophys.*, vol. 541, p. A47, May 2012.

[73] W. Vlemmings, G. Surcis, K. Torstensson, and H. Van Langevelde, "Magnetic field regulated infall on the disc around the massive protostar Cepheus A HW2," *Mon. Not. R. Astron. Soc.*, vol. 404, no. 1, pp. 134–143, 2010.

[74] D. Dall'Olio, W. H. T. Vlemmings, G. Surcis, H. Beuther, B. Lankhaar, M. V. Persson, A. M. S. Richards, and E. Varenius, "Methanol masers reveal the magnetic field of the high-mass protostar IRAS 18089-1732," *ArXiv e-prints*, Aug. 2017.

[75] B.-C. Koo, D. R. Williams, C. Heiles, and D. C. Backer, "A survey of 12.2 ghz methanol masers and their polarization properties," *Astrophys. J.*, vol. 326, pp. 931–940, 1988.

[76] A. Sarma and E. Momjian, "Detection of the Zeeman effect in the 36 GHz Class I CH_3OH maser line with the EVLA," *Astrophys. J. Lett.*, vol. 705, no. 2, p. L176, 2009.

[77] A. Sarma and E. Momjian, "Discovery of the Zeeman effect in the 44 GHz Class I methanol (CH_3OH) maser line," *Astrophys. J. Lett.*, vol. 730, no. 1, p. L5, 2011.

[78] J.-h. Kang, D.-Y. Byun, K.-T. Kim, J. Kim, A.-R. Lyo, and W. Vlemmings, "Linear polarization of class i methanol masers in massive star-forming regions," *Astrophys. J. Supp. S.*, vol. 227, no. 2, p. 17, 2016.

[79] H. Wiesemeyer, C. Thum, and C. Walmsley, "The polarization of mm methanol masers," *Astron. Astrophys.*, vol. 428, no. 2, pp. 479–495, 2004.

[80] R. Norris, W. McCutcheon, J. Caswell, K. Wellington, J. Reynolds, R. Peng, and M. Kesteven, "Milliarcsecond maps of 12 ghz methanol masers," *Nature*, vol. 335, no. 6186, p. 149, 1988.

[81] R. Norris, J. Whiteoak, J. Caswell, and M. Wieringa, "Synthesis images of 6.7-ghz methanol masers," in *Astrophysical Masers*, pp. 203–206, Springer, 1993.

[82] V. Minier, R. Booth, and J. Conway, "Vlbi observations of 6.7 and 12.2 ghz methanol masers toward high mass star-forming regions. i. observational results: protostellar disks or outflows?," *Astron. Astrophys.*, vol. 362, pp. 1093–1108, 2000.

[83] A. Bartkiewicz, M. Szymczak, and H. Van Langevelde, "Ring shaped 6.7 ghz methanol maser emission around a young high-mass star," *Astron. Astrophys.*, vol. 442, no. 3, pp. L61–L64, 2005.

[84] A. Sanna, L. Moscadelli, R. Cesaroni, A. Tarchi, R. Furuya, and C. Goddi, "Vlbi study of maser kinematics in high-mass star-forming regions-i. g16. 59–0.05," *Astron. Astrophys.*, vol. 517, p. A71, 2010.

[85] L. Moscadelli, R. Cesaroni, M. Rioja, R. Dodson, and M. Reid, "Methanol and water masers in iras 20126+ 4104: the distance, the disk, and the jet," *Astron. Astrophys.*, vol. 526, p. A66, 2011.

[86] C. Goddi, L. Moscadelli, and A. Sanna, "Infall and outflow within 400 au from a high-mass protostar-3d velocity fields from methanol and water masers in aflg 5142," *Astron. Astrophys.*, vol. 535, p. L8, 2011.

[87] K. Sugiyama, K. Fujisawa, K. Hachisuka, Y. Yonekura, K. Motogi, S. Sawada-Satoh, N. Matsumoto, D. Hirano, K. Hayashi, H. Kobayashi, *et al.*, "Observations of 6.7 ghz methanol masers with east-asian vlbi network. ii. internal proper motion measurement in g006. 79- 00.25," *Pub. Astron. Soc. Jap.*, vol. 68, no. 5, 2016.

[88] A. Sanna, L. Moscadelli, G. Surcis, H. van Langevelde, K. Torstensson, and A. Sobolev, "Planar infall of ch3oh gas around cepheus a hw2," *Astron. Astrophys.*, vol. 603, p. A94, 2017.

[89] C. Goddi, L. Moscadelli, and A. Sanna, "3d velocity fields from methanol and water masers in an intermediate-mass protostar," *Proceedings of the International Astronomical Union*, vol. 8, no. S287, pp. 401–406, 2012.

[90] R. Plambeck and K. Menten, "95 ghz methanol masers near dr 21 and dr 21 (oh)," *Astrophys. J.*, vol. 364, pp. 555–560, 1990.

[91] S. Kurtz, P. Hofner, and C. V. Alvarez, "A catalog of ch3oh 70-61 a+ maser sources in massive star-forming regions," *Astrophys. J. Supp. S.*, vol. 155, no. 1, p. 149, 2004.

[92] M. Voronkov, J. Caswell, S. Ellingsen, J. Green, and S. Breen, "Southern class i methanol masers at 36 and 44 ghz," *Mon. Not. R. Astron. Soc.*, vol. 439, no. 3, pp. 2584–2617, 2014.

[93] N. Matsumoto, T. Hirota, K. Sugiyama, K.-T. Kim, M. Kim, D.-Y. Byun, T. Jung, J. O. Chibueze, M. Honma, O. Kameya, *et al.*, "The first very long baseline interferometry image of a 44 ghz methanol maser with the kvn and vera array (kava)," *Astrophysical J. L.*, vol. 789, no. 1, p. L1, 2014.

[94] S. Kalenskii, L. E. Johansson, P. Bergman, S. Kurtz, P. Hofner, C. Walmsley, and V. Slysh, "Search for class i methanol masers in low-mass star formation regions," *Mon. Not. R. Astronom. Soc.*, vol. 405, no. 1, pp. 613–620, 2010.

[95] Y. Pihlström, L. Sjouwerman, D. Frail, M. Claussen, R. Mesler, and B. McEwen, "Detection of class i methanol (ch3oh) maser candidates in supernova remnants," *Astronom. J.*, vol. 147, no. 4, p. 73, 2014.

[96] W. H. Vlemmings, P. J. Diamond, and H. Imai, "A magnetically collimated jet from an evolved star," *Nature*, vol. 440, no. 7080, pp. 58–60, 2006.

[97] E. C. Sutton, A. Sobolev, S. Salii, A. Malyshev, A. Ostrovskii, and I. Zinchenko, "Methanol in w3 (h2o) and surrounding regions," *Astrophys. J.*, vol. 609, no. 1, p. 231, 2004.

[98] A. Sobolev. personal communication.

[99] E. G. Blackman, A. Frank, J. A. Markiel, J. H. Thomas, and H. M. Van Horn, "Dynamos in asymptotic-giant-branch stars as the origin of magnetic fields shaping planetary nebulae," *Nature*, vol. 409, no. 6819, pp. 485–487, 2001.

[100] H. Imai, K. Obara, P. J. Diamond, T. Omodaka, and T. Sasao, "A collimated jet of molecular gas from a star on the asymptotic giant branch," *Nature*, vol. 417, no. 6891, pp. 829–831, 2002.

[101] A. Kemball and P. Diamond, "Imaging the magnetic field in the atmosphere of tx camelopardalis," *Astrophys. J. Lett.*, vol. 481, no. 2, p. L111, 1997.

[102] A. J. Kemball, P. J. Diamond, I. Gonidakis, M. Mitra, K. Yim, K.-C. Pan, and H.-F. Chiang, "Multi-epoch imaging polarimetry of the sio masers in the extended atmosphere of the mira variable tx cam," *Astrophys. J.*, vol. 698, no. 2, p. 1721, 2009.

[103] F. Herpin, A. Baudry, C. Thum, D. Morris, and H. Wiesemeyer, "Full polarization study of sio masers at 86 ghz," *Astron. Astrophys.*, vol. 450, no. 2, pp. 667–680, 2006.

[104] B. Balick and A. Frank, "Shapes and shaping of planetary nebulae," *Annu. Rev. Astron. Astrophys.*, vol. 40, no. 1, pp. 439–486, 2002.

[105] P. Diamond, A. Kemball, W. Junor, A. Zensus, J. Benson, and V. Dhawan, "Observation of a ring structure in sio maser emission from late-type stars," *Astrophys. J.*, vol. 430, pp. L61–L64, 1994.

[106] T. Troland, C. Heiles, D. Johnson, and F. Clark, "Polarization properties of the 86.2 ghz v= 1, j= 2-1 sio maser," *Astrophys. J.*, vol. 232, pp. 143–157, 1979.

[107] R. Barvainis, G. McIntosh, and C. R. Predmore, "Evidence for strong magnetic fields in the inner envelopes of late-type stars," *Nature*, vol. 329, no. 6140, pp. 613–615, 1987.

[108] A. Kemball, P. Diamond, L. Richter, I. Gonidakis, and R. Xue, "Electric vector rotations of $\pi/2$ in polarized circumstellar sio maser emission," *Astrophys. J.*, vol. 743, no. 1, p. 69, 2011.

[109] W. Cotton, B. Mennesson, P. Diamond, G. Perrin, V. C. du Foresto, G. Chagnon, H. van Langevelde, S. Ridgway, R. Waters, W. Vlemmings, *et al.*, "Vlba observations of sio masers towards mira variable stars," *Astronomy & Astrophysics*, vol. 414, no. 1, pp. 275–288, 2004.

[110] W. Cotton, W. Vlemmings, B. Mennesson, G. Perrin, V. C. du Foresto, G. Chagnon, P. Diamond, H. van Langevelde, E. Bakker, S. Ridgway, *et al.*, "Further vlba observations of sio masers toward mira variable stars," *Astronomy & Astrophysics*, vol. 456, no. 1, pp. 339–350, 2006.

[111] D. Wiebe and W. Watson, "A non-zeeman interpretation for polarized maser radiation and the magnetic field at the atmospheres of late-type giants," *The Astrophysical Journal Letters*, vol. 503, no. 1, p. L71, 1998.

Hyperfine interactions and internal rotation in methanol

Boy Lankhaar, Gerrit C. Groenenboom, and Ad van der Avoird

Citation: J. Chem. Phys. **145**, 244301 (2016); doi: 10.1063/1.4972004
View online: http://dx.doi.org/10.1063/1.4972004
View Table of Contents: http://aip.scitation.org/toc/jcp/145/24
Published by the American Institute of Physics

Hyperfine interactions and internal rotation in methanol

Boy Lankhaar,[1,2] Gerrit C. Groenenboom,[1] and Ad van der Avoird[1,a)]
[1]*Theoretical Chemistry, Institute for Molecules and Materials, Radboud University, Heyendaalseweg 135, 6525 AJ Nijmegen, The Netherlands*
[2]*Department of Earth and Space Sciences, Chalmers University of Technology, Onsala Space Observatory, 439 92 Onsala, Sweden*

(Received 10 November 2016; accepted 28 November 2016; published online 22 December 2016)

We present a rigorous derivation of the nuclear spin-rotation and spin-torsion coupling terms in the hyperfine Hamiltonian for molecules with internal rotation. Our formulas differ from the expressions derived by Heuvel and Dymanus [J. Mol. Spectrosc. **47**, 363 (1973)], which these authors used and which were also applied recently by others to interpret experimental hyperfine spectra of such molecules. In the present work, our theoretical results are applied to methanol. We calculate the nuclear spin-spin magnetic dipole-dipole interactions and the nuclear contribution to the spin-torsion coupling vectors from the nuclear coordinates as functions of the internal rotation angle γ, compute the spin-rotation coupling tensors by *ab initio* electronic structure methods also as functions of γ, and obtain the missing parameters for the electronic contribution to the spin-torsion coupling from a fit to measured spectra. The resulting hyperfine Hamiltonian is then used to compute hyperfine transition frequencies and intensities for twelve torsion-rotation transitions in methanol. With the use of the *ab initio* calculated spin-rotation coupling parameters without any modification, and physically reasonable values for the spin-torsion coupling parameters from the fit, we find good agreement with all of the measured spectra. *Published by AIP Publishing.* [http://dx.doi.org/10.1063/1.4972004]

I. INTRODUCTION

Radiation emitted from star-forming regions by molecular masers such as water, OH, and methanol is used by radio-astronomers to extract information on magnetic fields in different sections of the accretion disk around the protostar.[1–3] The relevant molecular parameters to relate the observed Zeeman shifts between left and right circularly polarized radiation to the local magnetic field strength are well known for H_2O and OH, but not for methanol. Detailed knowledge of the hyperfine splitting of the torsion-rotation levels of methanol is required, but cannot be extracted from the available experimental data alone. Methanol has also been identified as the most sensitive molecule for a search of a varying proton-electron mass ratio on a cosmological time scale.[4] Observations of extragalactic methanol have led to a constraint on the variation of this ratio.[5–7] The line shapes in the observed spectra may be affected by underlying hyperfine structure, but this has not been included in the analysis. In the studies of galactic cold cores the lines are narrower, which makes hyperfine structure an essential ingredient to include in analyses.

The theoretical description of hyperfine coupling in molecules with internal rotation such as methanol has been addressed in some papers cited below. The present paper revisits the theory, derives a slightly but significantly different formalism, and applies it to determine the hyperfine structure of methanol in different torsion-rotation states. Just as the recent study on methanol by Coudert *et al.*,[8] we combine *ab initio* electronic structure calculations and fits to experimental data to obtain the relevant hyperfine coupling parameters.

The dominant hyperfine interactions in closed-shell molecules are the magnetic dipole-dipole coupling between the nuclei with spin $I > 0$, the electric quadrupole coupling for nuclei with spin $I \geq 1$, and the interaction of the nuclear spins with the magnetic field generated by overall rotation of the molecule, the so-called spin-rotation coupling. The theoretical description of all these interactions is well known. In molecules with internal rotation, such as methanol, also the internal rotation generates a magnetic field and an additional interaction term occurs: spin-torsion coupling. A theoretical description of spin-torsion coupling was given in 1972 by Heuvel and Dymanus[9,10] who also performed measurements on methanol[9,11] and applied their theory to extract the relevant coupling parameters from the experimental data. The symmetry properties of the torsion-rotation Hamiltonian including these hyperfine couplings were discussed by Hougen *et al.*[12] Further measurements on the hyperfine structure of methanol were reported in 2015 by Coudert *et al.*;[8] the interpretation of their experimental data was based on the theory of Ref. 10. The parameters fitted in Ref. 8 to the measured hyperfine spectra of methanol showed some peculiar features; however: (i) the dominant spin-rotation coupling parameter from the fit deviates much more from the value obtained by the advanced electronic structure calculations than could be expected on the basis of results for other molecules, and (ii) the dominant spin-torsion coupling parameter computed with a formula for the nuclear contribution from Ref. 10 was increased by a factor of 2 in the fit, instead of showing the expected reduction by the electronic contribution. These discrepancies could be due to some inconsistencies in the formulas of Ref. 10, especially regarding the way to apply the so-called Thomas precession correction.

a)A.vanderAvoird@theochem.ru.nl

Thomas precession is a purely kinematic effect that follows from the special theory of relativity, but does not vanish at small velocities. It is named after Thomas who showed[13] in 1927 that the correction factor associated with this precession is essential to obtain the correct mathematical expression for the spin-orbit coupling in atoms. For nuclear spin-rotation coupling in molecules, the precession is related to the acceleration of the nuclei in the molecule into curved paths by the electrostatic forces from the electrons and the other nuclei. Such a Thomas precession correction is included in the formulas of Heuvel and Dymanus,[10] but the correction factor in that paper, and also in the earlier paper on spin-rotation coupling by Gunther-Mohr, Townes, and van Vleck[14] is not correct.[15] It was given correctly in Ref. 16, but the precession correction was omitted entirely in the formula for spin-rotation coupling in Flygare's textbook.[17] The omission of the Thomas precession correction from his book is justified because he had derived[15] in 1964 that this correction completely vanishes when the nuclei in the molecule are in their equilibrium positions, where they do not experience any net force. When the molecule vibrates about its equilibrium geometry, the Thomas precession correction does not vanish, and it has actually been computed for several diatomic molecules[18,19] from a formula derived in Refs. 19 and 20. The amplitudes of vibration in these systems are small; however, and the Thomas precession correction has only a minute effect on the calculated spin-rotation coupling constants. For molecules with large amplitude internal motions, such as the torsional motion in methanol, one would think that it might be more substantial. Here, we derive a formula for the Thomas precession correction associated with the internal rotation in molecules and apply it to methanol.

Another combined experimental and theoretical study of the hyperfine structure in the torsion-rotation spectrum of methanol was performed by Belov *et al.*[21] They investigated transitions between torsion-rotation levels of *E* symmetry with angular momenta *J* ranging from 13 to 34 by Lamb-dip submillimeter-wave spectroscopy and found unexpectedly large doublet splittings in the spectra due to hyperfine coupling. These doublet splittings occur for several, but not for all transitions, and they were explained by a theoretical model involving torsionally mediated spin-rotation coupling with parameters fitted to the experimental data. In Sec. IV B we will briefly refer to these results in relation to our results obtained with the full hyperfine Hamiltonian for a rotational transition between the levels with $J = 8$ and 9.

The starting point in our study of methanol is its torsion-rotation states. They can be derived from the Hamiltonian given by Hougen *et al.*[22] It is based on the classical expression for the kinetic energy of a molecule with internal rotation about a single axis derived by Lin and Swalen.[23] Hougen *et al.* express this Hamiltonian in different coordinate systems and show that its eigenstates are most easily evaluated with the so-called rho-axis method (RAM). Their paper also includes a discussion of the symmetry properties of the Hamiltonian. A program, BELGI,[22] was developed to carry out the evaluation of the torsion-rotation levels. The parameters in the Hamiltonian were obtained by Xu *et al.*[24] from a global fit of these levels to a large data set of observed spectral transitions. To supplement this Hamiltonian with the correct expressions for hyperfine interactions, we briefly recapitulate and then extend its derivation, while paying special attention to the form of the operators representing spin-rotation and spin-torsion coupling. We also evaluated the nuclear spin magnetic dipole-dipole interactions and carried out electronic structure calculations with the program package CFOUR,[25] to obtain numerical values for the spin-rotation coupling tensors in methanol as functions of the internal rotation angle. Calculation of the spin-torsion coupling tensors is not implemented in this program, so we applied our formula for spin-torsion coupling to evaluate the nuclear contribution to these tensors and we estimate the electronic contributions from a fit of our calculated spectra to experimental data.[8,11] Furthermore, we computed the Thomas precession correction to the spin-rotation and spin-torsion tensors with the formula that we derived for molecules with internal rotation. Finally, we used our hyperfine Hamiltonian with the *ab initio* calculated and fitted parameters to compute the hyperfine levels for several rotational states of methanol, generated transition frequencies and intensities, and compared our results to the measured spectra.

II. THEORY

A. Hyperfine coupling

Methanol, CH_3OH, is an asymmetric rotor molecule, consisting of a symmetric rotor "top," the CH_3 group, attached to a "frame," the OH group. The internal rotation of the methyl group with respect to the hydroxyl group is hindered by a potential $V(\gamma)$ depending on the internal rotation angle γ with a threefold barrier of 374 cm^{-1}.[24] For the lowest energy levels, the internal rotation or torsion is classically forbidden, but occurs by quantum mechanical tunneling. The carbon and oxygen nuclei in their most abundant ^{12}C and ^{16}O forms have nuclear spin $I = 0$. The only nuclei involved in hyperfine coupling are the four hydrogen nuclei with spin $I = 1/2$. The hyperfine coupling Hamiltonian of a molecule with internal rotation is given by

$$H^{\text{hyper}} = H^{\text{DD}} + H^{\text{SR}} + H^{\text{ST}}, \tag{1}$$

where

$$H^{\text{DD}} = \sum_{K<L} \hat{\boldsymbol{I}}_K \cdot \boldsymbol{D}_{KL}(\gamma)\, \hat{\boldsymbol{I}}_L \tag{2}$$

describes the magnetic dipole-dipole coupling between the nuclei, H^{SR} is the nuclear spin-rotation coupling, and H^{ST} is the spin-torsion coupling. The nuclei are labeled with K and L, and $\hat{\boldsymbol{I}}_K$ are the nuclear spin operators. The form of the magnetic dipole-dipole coupling tensor $\boldsymbol{D}_{KL}$, a second rank irreducible tensor, is well known. It is also valid for molecules with internal rotation, where it depends on the angle γ.

The expressions for the spin-rotation and spin-torsion coupling terms in the Hamiltonian for a molecule with internal rotation

$$\begin{aligned} H^{\text{SR}} &= -\sum_K \hat{\boldsymbol{I}}_K \cdot \boldsymbol{M}_K(\gamma)\, \hat{\boldsymbol{J}} \\ &\quad + \sum_K 2F\, \hat{\boldsymbol{I}}_K \cdot \boldsymbol{M}_K(\gamma)\, \boldsymbol{I}^{\text{top}} \boldsymbol{\lambda} \left(\hat{p}_\gamma - \boldsymbol{\rho} \cdot \hat{\boldsymbol{J}}\right) \end{aligned} \tag{3}$$

and

$$H^{\text{ST}} = -\sum_K 2F\, \hat{\boldsymbol{I}}_K \cdot \boldsymbol{w}_K(\gamma) \left(\hat{p}_\gamma - \boldsymbol{\rho} \cdot \hat{\boldsymbol{J}}\right) \tag{4}$$

are derived in Appendix A. The spin-rotation coupling tensors are given by $\boldsymbol{M}_K(\gamma) = \boldsymbol{W}_K(\gamma)\,\boldsymbol{I}^{-1}$ and the tensors $\boldsymbol{W}_K(\gamma)$, as well as the spin-torsion coupling vectors $\boldsymbol{w}_K(\gamma)$ are also defined in Appendix A. The total inertia tensor $\boldsymbol{I}$ does not depend on γ because the rotating "top" with inertia tensor $\boldsymbol{I}^{\rm top}$ is a symmetric rotor. The unit vector $\boldsymbol{\lambda}$ is the direction of the internal rotation axis; the constant F and the constant vector $\boldsymbol{\rho} = \boldsymbol{I}^{-1}\boldsymbol{I}^{\rm top}\boldsymbol{\lambda}$ are defined in Eq. (A8). All tensor and vector components are given with respect to the principal axis frame MF of the whole molecule, in which the total inertia tensor $\boldsymbol{I}$ is diagonal. The operator $\hat{\boldsymbol{J}}$ represents the total rotational angular momentum, $\hat{p}_\gamma = (\hbar/i)\partial/\partial\gamma$ is the torsional angular momentum operator, and $\hbar$ is the reduced Planck constant.

The derivation in Appendix A starts by recalling the derivation of the torsion-rotation kinetic energy operator, since this operator is needed to obtain the correct expressions for the total angular momentum $\hat{\boldsymbol{J}}$ and the torsional angular momentum $\hat{p}_\gamma$. In the formulas in Eq. (A6) for their classical equivalents, one can observe that for molecules with internal rotation not only the overall angular velocity $\boldsymbol{\omega}$ appears in the total angular momentum $\boldsymbol{J}$ but also the torsional velocity $\dot{\gamma}$. Vice-versa, not only $\dot{\gamma}$ appears in the torsional angular momentum p_γ but also $\boldsymbol{\omega}$. By consequence, we find that the expression for the spin-rotation coupling Hamiltonian $H^{\rm SR}$ in Eq. (3) not only contains the usual terms $-\hat{\boldsymbol{I}}_K \cdot \boldsymbol{M}_K\,\hat{\boldsymbol{J}}$ but also the contributions that involve both the torsional and overall angular momenta $\hat{p}_\gamma$ and $\hat{\boldsymbol{J}}$. Vice-versa, the spin-torsion coupling Hamiltonian in Eq. (4) involves not only the angular momentum $\hat{p}_\gamma$ but also the rotational angular momentum $\hat{\boldsymbol{J}}$.

The additional terms in the spin-rotation Hamiltonian have a form that is similar to the spin-torsion Hamiltonian and can be absorbed into the latter by defining

$$\boldsymbol{w}'_K(\gamma) = \boldsymbol{w}_K(\gamma) - \boldsymbol{M}_K(\gamma)\boldsymbol{I}^{\rm top}\boldsymbol{\lambda}. \tag{5}$$

The total spin-rotation-torsion Hamiltonian then becomes

$$H^{\rm SR} + H^{\rm ST} = -\sum_K \left[\hat{\boldsymbol{I}}_K \cdot \boldsymbol{M}_K(\gamma)\,\hat{\boldsymbol{J}} + 2F\,\hat{\boldsymbol{I}}_K \cdot \boldsymbol{w}'_K(\gamma)\left(\hat{p}_\gamma - \boldsymbol{\rho}\cdot\hat{\boldsymbol{J}}\right)\right]. \tag{6}$$

In methanol the unit vector $\boldsymbol{\lambda}$ in the direction of the internal rotation axis is very nearly parallel to the principal axis a of the CH_3OH molecule and we find that

$$\boldsymbol{I}^{\rm top}\boldsymbol{\lambda} \approx I_\gamma \boldsymbol{\lambda}, \tag{7}$$

where $I_\gamma = \boldsymbol{\lambda}\cdot\boldsymbol{I}^{\rm top}\boldsymbol{\lambda}$ is the moment of inertia of the "top" rotating about the axis $\boldsymbol{\lambda}$. Equation (6) can then be rewritten as

$$H^{\rm SR} + H^{\rm ST} = -\sum_K \left[\hat{\boldsymbol{I}}_K \cdot \boldsymbol{M}_K(\gamma)\,\hat{\boldsymbol{J}} + f\,\hat{\boldsymbol{I}}_K \cdot \boldsymbol{d}'_K(\gamma)\left(\hat{p}_\gamma - \boldsymbol{\rho}\cdot\hat{\boldsymbol{J}}\right)\right] \tag{8}$$

with the dimensionless factor

$$f = 2F\,I_\gamma = (1 - \boldsymbol{\rho}\cdot\boldsymbol{\lambda})^{-1}. \tag{9}$$

By analogy with Eq. (5) we obtain

$$\boldsymbol{d}'_K(\gamma) = \boldsymbol{d}_K(\gamma) - \boldsymbol{M}_K(\gamma)\boldsymbol{\lambda} \tag{10}$$

with the spin-torsion coupling vector

$$\boldsymbol{d}_K(\gamma) = \boldsymbol{w}_K(\gamma) I_\gamma^{-1}. \tag{11}$$

The operators $\hat{\boldsymbol{I}}_K$ and $\hat{\boldsymbol{J}}$ operate on the spin and spatial coordinates of the nuclei, respectively, so they commute. Their Cartesian components are Hermitian operators and the Cartesian components of the tensors $\boldsymbol{M}_K$ and the vectors $\boldsymbol{w}'_K$ and $\boldsymbol{d}'_K$ are real-valued. Hence, the Hamiltonians in Eqs. (6) and (8) are Hermitian operators, even though the spin-rotation coupling tensors $\boldsymbol{M}_K$ are not symmetric. We recall that both the tensors $\boldsymbol{M}_K$ and the spin-torsion coupling vectors $\boldsymbol{d}_K$ depend on the internal rotation angle γ. Furthermore, we recall that the components of the rotational angular momentum operator $\hat{\boldsymbol{J}}$ with respect to the MF frame obey anomalous commutation relations.[26]

B. Thomas precession correction

In our derivations, we assume that both the "frame" and the "top" parts in a molecule with internal rotation are rigid and that the nuclei in each part are fixed at their equilibrium positions. A formula for the Thomas precession correction for diatomic molecules vibrating around their equilibrium structure has been derived in Refs. 19 and 20, by an extension of Flygare's derivation[15] showing that this correction vanishes for molecules at their equilibrium geometry. When the molecule is not at its equilibrium geometry, the Thomas precession correction is directly related to the forces on the nuclei.

The result for diatomic molecules in Refs. 19 and 20 can also be derived directly by starting from the textbook formula[27] for the Thomas precession correction to the energy of a particle K (in this case, a nucleus) with spin $\boldsymbol{I}_K$ moving in a magnetic field

$$U_T^{(K)} = \boldsymbol{I}_K \cdot \boldsymbol{\omega}_T^{(K)}. \tag{12}$$

The Thomas precession frequency depends on the acceleration $\boldsymbol{a}_K$ and velocity $\boldsymbol{v}_K$ of the particle and (for velocities much smaller than the speed of light c) is given by

$$\boldsymbol{\omega}_T^{(K)} = \frac{1}{2c^2}\boldsymbol{a}_K \times \boldsymbol{v}_K. \tag{13}$$

The acceleration of a nucleus in a molecule is determined by the net force $\boldsymbol{F}_K$ acting on it; it vanishes when the molecule is in its equilibrium geometry. When it is not, the forces on the nuclei in a diatomic molecule simply follow from the derivative of the intramolecular potential with respect to the internuclear distance. By relating the acceleration $\boldsymbol{a}_K$ in the above formula to this derivative, one easily obtains the result of Refs. 19 and 20.

In molecules with weakly hindered internal rotation one must consider large deviations from their equilibrium geometry. Methanol, for instance, shows a large amplitude internal rotation of the CH_3 "top" with respect to the OH "frame." In our MF system of axes the "frame" stays at rest, while the "top" rotates. The acceleration of the hydrogen nuclei in the "top" is given by

$$\boldsymbol{a}_K = \frac{\boldsymbol{F}_K}{m_K} = -\frac{1}{m_K|\boldsymbol{\sigma}_K|}\frac{dV(\gamma)}{d\gamma}\boldsymbol{s}_K, \tag{14}$$

where $|\boldsymbol{\sigma}_K|$ is the distance of nucleus K to the internal rotation axis, the torsional potential $V(\gamma)$ depends on the internal rotation angle γ, $\hat{\boldsymbol{\sigma}}_K$ is a unit vector in the direction of the vector $\boldsymbol{\sigma}_K$, and the unit vector $\boldsymbol{s}_K = \boldsymbol{\lambda} \times \hat{\boldsymbol{\sigma}}_K$ points in the direction of the motion of nucleus K. The velocity of a hydrogen nucleus K

in the rotating "top" depends on the internal rotation velocity $\dot{\gamma}$, as well as on the overall rotational velocity $\boldsymbol{\omega}$,

$$\boldsymbol{v}_K = \boldsymbol{\omega} \times \boldsymbol{r}_K + \dot{\gamma} \boldsymbol{\lambda} \times \boldsymbol{r}_K. \tag{15}$$

The $\dot{\gamma}$ term does not contribute to the Thomas precession as it points in the same direction as the acceleration $\boldsymbol{a}_K$. Substitution of these results into Eq. (13) yields

$$\begin{aligned} \boldsymbol{\omega}_T^{(K)} &= -\frac{1}{2m_K|\boldsymbol{\sigma}_K|c^2} \frac{dV(\gamma)}{d\gamma} \boldsymbol{s}_K \times (\boldsymbol{\omega} \times \boldsymbol{r}_K) \\ &= \frac{1}{2m_K|\boldsymbol{\sigma}_K|c^2} \frac{dV(\gamma)}{d\gamma} [\, (\boldsymbol{r}_K \cdot \boldsymbol{s}_K)\, \mathbf{1} - \boldsymbol{r}_K \otimes \boldsymbol{s}_K \,] \boldsymbol{\omega}. \end{aligned} \tag{16}$$

The symbol $\mathbf{1}$ represents the 3×3 unit matrix, while $\otimes$ stands for the tensor product of two vectors. The angular velocity $\boldsymbol{\omega}$ is related to the total angular momentum $\boldsymbol{J}$ and the torsional angular momentum p_γ by Eq. (A7), and the Thomas correction to the energy is given in operator form by

$$U_T^{(K)} = \hat{\boldsymbol{I}}_K \cdot \boldsymbol{Q}_K \hat{\boldsymbol{J}} - 2F \hat{\boldsymbol{I}}_K \cdot \boldsymbol{q}_K (\hat{p}_\gamma - \boldsymbol{\rho} \cdot \hat{\boldsymbol{J}}) \tag{17}$$

with

$$\boldsymbol{Q}_K = \frac{1}{2m_K|\boldsymbol{\sigma}_K|c^2} \frac{dV(\gamma)}{d\gamma} [\, (\boldsymbol{r}_K \cdot \boldsymbol{s}_K)\, \mathbf{1} - \boldsymbol{r}_K \otimes \boldsymbol{s}_K \,] \boldsymbol{I}^{-1} \tag{18}$$

and

$$\boldsymbol{q}_K = \frac{1}{2m_K|\boldsymbol{\sigma}_K|c^2} \frac{dV(\gamma)}{d\gamma} [\, (\boldsymbol{r}_K \cdot \boldsymbol{s}_K)\, \mathbf{1} - \boldsymbol{r}_K \otimes \boldsymbol{s}_K \,] \boldsymbol{\rho}. \tag{19}$$

The tensors $\boldsymbol{Q}_K$ and vectors $\boldsymbol{q}_K$ may be considered as the Thomas precession corrections to the spin-rotation coupling tensors $\boldsymbol{M}_K$ and spin-torsion coupling vectors $\boldsymbol{w}'_K$ in Eq. (6). For methanol, we obtained Eq. (8), and $\boldsymbol{q}_K I_\gamma^{-1}$ is the correction to $\boldsymbol{d}'_K$. Both $\boldsymbol{Q}_K$ and $\boldsymbol{q}_K$ depend on the torsion angle γ and they can be directly computed from the nuclear positions in the molecule and the derivative $dV/d\gamma$ of the known potential $V(\gamma)$.

C. Symmetry

For molecules with internal motions that have multiple equilibrium geometries, i.e., multiple equivalent minima on their potential surface, one must use the permutation-inversion (PI) group or molecular symmetry group,[28,29] rather than the point group of a single equilibrium structure. We label the CH_3 protons in methanol with 1, 2, 3 and the OH proton with 4. Internal rotation of the CH_3 group corresponds to the cyclic permutations (123) and (132). The permutation-inversion operation $(23)^*$, i.e., the interchange of protons 2 and 3 combined with inversion corresponds to reflection in the point group C_{3v} of the equilibrium structure. The PI group G_6 of internally rotating methanol, isomorphic to C_{3v}, is generated by (123) and $(23)^*$. It has two one-dimensional irreducible representations (irreps), A_1 and A_2, and a two-dimensional one, E. The application of G_6 to molecules with internal rotation similar to methanol has extensively been discussed by Hougen *et al.*[22] They show, in particular, how the generators (123) and $(23)^*$ act on the torsion-rotation wave functions $\psi_{J,K_a}^{v_\tau,\sigma}$,

$$\begin{aligned} (123)\psi_{J,K_a}^{v_\tau,\sigma} &= \exp(2\pi\sigma i/3)\psi_{J,K_a}^{v_\tau,\sigma} \\ (23)^*\psi_{J,K_a}^{v_\tau,\sigma} &= (-1)^{J-K_a}\psi_{J,-K_a}^{v_\tau,-\sigma}. \end{aligned} \tag{20}$$

The quantum number J is the total angular momentum, K_a is its projection on the a axis of the MF frame, v_τ is the torsional quantum number and σ is the torsional symmetry quantum number, adopting the values 0 and ±1. It follows from these equations that functions with $\sigma = 0$ transform according to the A_1 or A_2 irreps, and functions with $\sigma = \pm 1$ span the E irrep.

When investigating hyperfine splittings of the torsion-rotation levels, one must also include the nuclear spin wave functions of the four protons. This is most conveniently done by first coupling the spins I_1, I_2, I_3 of the equivalent protons in the CH_3 group. This yields one set of functions with total spin $I_{123} = 3/2$ with projections $M_I = 3/2,\ 1/2,\ 1/2,\ 3/2$, and two sets of functions with $I_{123} = 1/2$ and $M_I = 1/2,\ 1/2$. Since, inversion does not affect the nuclear spin functions, it follows from their behavior under the permutations (123) and (23) that the functions with $I_{123} = 3/2$ span the irrep A_1 of G_6, while the two sets of functions with $I_{123} = 1/2$ each carry the irrep E. Next, these functions are coupled with the nuclear spin $I_4 = 1/2$ of the OH proton, which yields functions $|(I_{123}, I_4)I\rangle$ of A_1 symmetry with total spin $I = 1$ and 2, and functions of E symmetry with total spin $I = 0$ and 1.

Since protons are fermions, the Pauli principle requires that the total torsion-rotation-spin wave functions are anti-symmetric under odd permutations and symmetric under even permutations. The Pauli principle does not impose any conditions on the inversion behavior of the wave function, so total wave functions of A_1 and A_2 symmetry in the group G_6 are both appropriate. One way to obtain such total wave functions is by taking the product of a nuclear spin wave function $|(I_{123} = 3/2, I_4)I\rangle$ of A_1 symmetry and a torsion-rotation wave function with $\sigma = 0$,

$$\left[\psi_{J,K_a}^{v_\tau,0} \pm (-1)^{J-K_a}\psi_{J,-K_a}^{v_\tau,0}\right]/\sqrt{2}, \tag{21}$$

that has A_1 or A_2 symmetry. Another way is by combining two nuclear spin wave functions $|(I_{123} = 1/2, I_4)I\rangle$ that together carry irrep E with torsion-rotation wave functions with $\sigma = \pm 1$ that also carry irrep E. If we set up a basis $\left\{\psi_1^E, \psi_2^E\right\} = \left\{\psi_{J,K_a}^{v_\tau,1},\ (-1)^{J-K_a}\psi_{J,-K_a}^{v_\tau,-1}\right\}$, the operations (123) and $(23)^*$ are represented by the irrep matrices

$$\boldsymbol{P}_{123}^E = \begin{pmatrix} e^{2\pi i/3} & 0 \\ 0 & e^{-2\pi i/3} \end{pmatrix} \quad \text{and} \quad \boldsymbol{P}_{23^*}^E = \begin{pmatrix} 0 & 1 \\ 1 & 0 \end{pmatrix}. \tag{22}$$

By taking appropriate linear combinations of the wave functions $|(I_{123} = 1/2, I_4)I\rangle$, one can construct nuclear spin wave functions $\left\{\phi_1^E, \phi_2^E\right\}$ that carry the same E irrep matrix $\boldsymbol{P}_{23^*}$ and a matrix complex conjugate to $\boldsymbol{P}_{123}$. Total wave functions of A_1 and A_2 symmetry obeying the Pauli principle are then obtained by taking

$$\Psi^{\text{tot}} = \left[\psi_1^E \phi_1^E \pm \psi_2^E \phi_2^E\right]/\sqrt{2}. \tag{23}$$

III. METHODS

A. Torsion-rotation structure

The internal-rotation Hamiltonian used to calculate the torsion-rotation levels and wave functions is defined by the rho axis method (RAM) described in Refs. 22 and 30–32. The z-axis of the RAM frame is parallel to the vector $\boldsymbol{\rho}$ defined in Eq. (A8), which has the advantage that only the term $2F\,\rho\hat{p}_\gamma\,\hat{J}_z$

in the Hamiltonian of Eq. (A9) couples the internal and overall rotation, so that all operators containing the torsional angular momentum $\hat{p}_\gamma$ are diagonal in the rotational quantum number K_a. The operator $\hat{J}_z$ with eigenvalues K_a is the projection of the total angular momentum $\hat{\boldsymbol{J}}$ on the z-axis of the RAM frame, ρ is the length of the vector $\boldsymbol{\rho}$, and F is defined in Eq. (A8). In methanol, the angle between the vector $\boldsymbol{\rho}$, i.e., the z-axis of the RAM frame, and the principal a axis is less than half a degree. We take this a axis as the z-axis of our principal axes frame MF and assume that the RAM frame coincides with our MF frame in this case.

The eigenstates of this Hamiltonian are determined in two steps. In the first step, the torsional Hamiltonian

$$\hat{H}^{\text{tors}} = F(\hat{p}_\gamma - \rho\hat{J}_z)^2 + V(\gamma) \tag{24}$$

is diagonalized for each value of K_a in a basis consisting of functions $\exp[i(3k+\sigma)\gamma]/\sqrt{2\pi}$, with k running from -10 to 10. The eigenfunctions from this first step are the torsional wave functions: $|(K_a)v_\tau\sigma\rangle$. In the second step, these torsional wave functions for all $2J+1$ values of K_a are included in the calculation of the rotational states for given J. They are multiplied with the symmetric rotor functions $|JMK_a\rangle = \sqrt{\frac{2J+1}{8\pi^2}}D^{(J)}_{MK_a}(\chi,\theta,\phi)^*$ that depend on the overall rotation angles (χ,θ,ϕ) to provide the basis in which the full torsion-rotation Hamiltonian is diagonalized. This procedure is implemented in the BELGI code.[22] The standard version of the code was modified and improved by Xu *et al.*[24] who fitted a set of 119 molecular parameters of methanol to a dataset of 25 000 measured spectral transitions and reproduced the lower torsion-rotation energy levels with an accuracy better than 100 kHz.[4] The resulting parameters are listed in Table 2 of Ref. 24.

B. Hyperfine levels

1. Hyperfine coupling tensors

Spin-rotation coupling tensors $\boldsymbol{M}_K(\gamma)$ can be obtained from *ab initio* electronic structure calculations with the program package CFOUR.[25] Calculations with CFOUR were carried out at the coupled-cluster level of theory including single and double excitations with perturbative addition of the triples contribution [CCSD(T)], in an augmented triple-zeta correlation-consistent (aug-cc-pVTZ) basis set.[33] The geometry of methanol was optimized at this level, which yields OH and CO bond lengths of 0.956 and 1.427 Å, respectively, a COH bond angle of 108.87° and a torsional HOCH angle of 180°. Averaging the equilibrium values to maintain C_{3v} symmetry of the rotating CH_3 group, we find CH bond lengths and OCH bond angles of 1.096 Å and 109.91°.

The electronic contributions to the spin-rotation coupling tensors $\boldsymbol{M}_K(\gamma)$ were calculated at the same level of theory for 13 equidistant values of the torsional angle γ by keeping the HOC fragment fixed and rotating the CH_3 group over these angles about the OC bond axis. The nuclear contributions to the tensors $\boldsymbol{M}_K(\gamma)$ were also given by CFOUR, but were also calculated directly from the nuclear coordinates. Also the magnetic dipole-dipole coupling tensors $\boldsymbol{D}_{KL}(\gamma)$ were calculated from the nuclear coordinates for the same 13 values of γ, as well as the nuclear contributions to the spin-torsion coupling vectors $\boldsymbol{d}_K(\gamma)$. For the latter, we used Eqs. (11) and (A17). Calculation of the electronic contribution to the spin-torsion vectors $\boldsymbol{d}_K(\gamma)$ is not implemented in CFOUR. We obtained it from a fit to measured hyperfine spectra described below. Results that we computed for other, rigid, molecules such as H_2O showed us that spin-rotation tensors $\boldsymbol{M}_K(\gamma)$ from electronic structure calculations at this level of theory are quite accurate, so we kept our *ab initio* values for these tensors. Still, in contrast with the work of Coudert *et al.*[8] who included these values in their fit, we could obtain a good fit of the experimental data by fitting only the spin-torsion vectors $\boldsymbol{d}_K(\gamma)$. All individual elements of the tensors $\boldsymbol{M}_K(\gamma)$ and $\boldsymbol{D}_{KL}(\gamma)$ and the vectors $\boldsymbol{d}_K(\gamma)$ were expanded in a Fourier series in γ. Some of the elements are symmetric with respect to a sign change of γ and were expanded in functions $\cos n\gamma$, others are antisymmetric and were expanded in functions $\sin n\gamma$.

2. Thomas precession corrections

In Sec. II B we recalled the result from the literature that the Thomas precession correction to the spin-rotation coupling vanishes for molecules at their equilibrium geometry. For molecules with a large amplitude internal rotation, such as methanol, we derived Eq. (18) for the Thomas correction $\boldsymbol{Q}_K$ to the spin-rotation coupling tensors and Eq. (19) for the Thomas correction $\boldsymbol{q}_K$ to the spin-torsion coupling vectors. The correction involves only the protons in the rotating CH_3 "top" and it requires knowledge of the torsional potential $V(\gamma)$. For methanol this potential can be written as

$$V(\gamma) = \sum_{n=1}^{3}\frac{V_{3n}}{2}(1-\cos 3n\gamma). \tag{25}$$

The parameters V_3, V_6, V_9 in this expression are known from the work by Xu *et al.*[24] The parameters V_6 and V_9 are very small, so they will be neglected here. The height of the threefold barrier, V_3, is 374 cm^{-1}.

3. Matrix elements and hyperfine levels

With the knowledge of all coupling tensors $\boldsymbol{D}_{KL}(\gamma)$, $\boldsymbol{M}_K(\gamma)$, and $\boldsymbol{d}_K(\gamma)$ in the hyperfine Hamiltonian, we can compute the hyperfine levels. The Hamiltonian is diagonalized in the basis $|\{(I_{123},I_4)I,J\}FM_F\rangle$ obtained by coupling the eigenfunctions of the torsion-rotation problem described in Sec. III A with the nuclear spin functions $|(I_{123},I_4)I\rangle$ defined in Sec. II C. Coupling the total nuclear spin I with the torsion-rotation angular momentum J yields the total angular momentum F and its projection M_F on the space-fixed z-axis. The torsion-rotation wave functions have quantum numbers v_τ, J, K_a and symmetry A or E, the nuclear spin basis of the same symmetry has $I_{123} = 3/2$ or $1/2$, see Sec. II C. The rotational quantum number K_a is only an approximate one, a rotational wave function with given J, K_a actually contains basis functions with all K_a ranging from $-J$ to J. Also the torsional and rotational quantum numbers v_τ and J are approximate ones, but the energy gaps between the torsion-rotation states are typically on the order of a few GHz, while the hyperfine coupling terms in methanol amount to about 10 kHz. Hence, the hyperfine Hamiltonian will hardly mix basis functions with different v_τ and J and we may restrict our basis to a

single value of these quantum numbers. With this assumption, the spin-rotation and spin-torsion Hamiltonian in Eq. (8) can be rewritten[12,34–36] as

$$\hat{H}_K^{\mathrm{SR}} + \hat{H}_K^{\mathrm{ST}} = \left(\hat{O}_K^{\mathrm{SR}} + \hat{O}_K^{\mathrm{ST}}\right)\left(\hat{\boldsymbol{I}}_K^{\mathrm{SF}} \cdot \hat{\boldsymbol{J}}^{\mathrm{SF}}\right). \quad (26)$$

The advantage of this factorization is that the scalar product operator $\hat{\boldsymbol{I}}_K \cdot \hat{\boldsymbol{J}}$ is invariant under rotation, which we used to express it in terms of the space-fixed (SF) components of the operators. Matrix elements over the SF basis $|\{(I_{123}, I_4)I, J\}FM_F\rangle$ are thus more easily evaluated. The operators

$$\hat{O}_K^{\mathrm{SR}} = \frac{1}{2J(J+1)}\hat{\boldsymbol{J}} \cdot \boldsymbol{M}_K(\gamma)\hat{\boldsymbol{J}} + \text{hermitian conjugate} \quad (27)$$

and

$$\hat{O}_K^{\mathrm{ST}} = \frac{1}{2J(J+1)} f\, \hat{\boldsymbol{J}} \cdot \boldsymbol{d}'_K(\gamma)\left(\hat{p}_\gamma - \boldsymbol{\rho} \cdot \hat{\boldsymbol{J}}\right) + \text{hermitian conjugate} \quad (28)$$

contain the body-fixed components of $\hat{\boldsymbol{J}}$ with respect to the MF frame, and also the tensors $\boldsymbol{M}_K(\gamma)$ and the vectors $\boldsymbol{d}'_K(\gamma)$ are given with respect to this frame. Matrix elements of the operators $\hat{O}_K^{\mathrm{SR}}$ and $\hat{O}_K^{\mathrm{ST}}$ over the torsion-rotation eigenfunctions are simply scalar values.

Also the dipole-dipole coupling Hamiltonian can be factorized into a part with body-fixed and a part with only space-fixed angular momentum operators

$$\hat{H}_{KL}^{\mathrm{DD}} = \hat{O}_{KL}^{\mathrm{DD}}\left[\frac{3}{2}(\hat{\boldsymbol{I}}_K^{\mathrm{SF}} + \hat{\boldsymbol{I}}_L^{\mathrm{SF}}) \cdot \hat{\boldsymbol{J}}^{\mathrm{SF}} - (\hat{\boldsymbol{I}}_K^{\mathrm{SF}} \cdot \hat{\boldsymbol{I}}_L^{\mathrm{SF}})(\hat{J}^{\mathrm{SF}})^2\right], \quad (29)$$

where

$$\hat{O}_{KL}^{\mathrm{DD}} = \frac{2}{J(J+1)(J-1)(2J+3)}\hat{\boldsymbol{J}} \cdot \boldsymbol{D}_{KL}(\gamma)\hat{\boldsymbol{J}}. \quad (30)$$

Also the matrix elements of $\hat{O}_{KL}^{\mathrm{DD}}$ are computed in the MF frame. Diagonalization of the matrix of the total hyperfine Hamiltonian in Eq. (1) for given v_τ and J yields a set of hyperfine levels labeled with the quantum number F.

4. Intensities

In order to compare our results with measured hyperfine spectra, we also computed the line strengths of the transitions between hyperfine levels. The dipole moment of methanol was calculated *ab initio* as a function of the internal rotation angle γ with the finite-field method at the same level of theory and with the same basis as the hyperfine coupling tensors. The spherical components of the dipole in the SF frame are related to the components calculated in the MF frame as $\mu_m^{\mathrm{SF}} = \sum_q D_{mq}^{(1)*}(\chi, \theta, \phi)\mu_q^{\mathrm{MF}}$, with (χ, θ, ϕ) being the overall rotation angles. Matrix elements of the SF dipole components μ_m over the coupled basis $|\{(I_{123}, I_4)I, J\}FM_F\rangle$ needed to compute rotational and hyperfine transition dipole moments were evaluated with the spherical tensor techniques explained in Appendix B.

IV. RESULTS

A. Calculated results

The *ab initio* calculated results for the spin-rotation coupling tensors $\boldsymbol{M}_K(\gamma)$ and the calculated and fitted results

TABLE I. Coefficients a_n in the Fourier expansion describing the γ dependence of the spin-rotation coupling tensors $\boldsymbol{M}_K(\gamma)$ calculated *ab initio*. The components of $\boldsymbol{M}_K$ are defined with respect to the principal axes *a*, *b*, and *c*. Terms in the Fourier series are $a_n \cos n\gamma$ or $a_n \sin n\gamma$, depending on whether a component is symmetric (+) or antisymmetric ( ) under the PI operation $(23)^*$ that involves a sign change of the torsional angle γ. The superscripts CH_3 and OH refer to the CH_3 protons (K = 1, 2, 3) and OH proton (K = 4), respectively. Results are given only for the CH_3 proton with K = 1, the values for K = 2, 3 correspond to a change of γ by 120° and 240°. All spin-rotation coupling expansion coefficients a_n and the coefficients a_n^{Th} of the Thomas precession corrections $\boldsymbol{Q}_K$ are given in kHz.

	Symmetry	a_0	a_1	a_2	a_3	a_4	a_5	a_6	$a_0^{\mathrm{Th}}(\approx a_6^{\mathrm{Th}})$
M_{aa}^{CH3}	+	12.486	0.741	−0.080	0.052	−0.005	$5.33 \cdot 10^{-4}$	$2.23 \cdot 10^{-4}$	$-1.40 \cdot 10^{-8}$
M_{bb}^{CH3}	+	0.579	−0.104	−1.660	−0.018	0.002	$-9.08 \cdot 10^{-4}$	$-1.45 \cdot 10^{-4}$	$1.3 \cdot 10^{-5}$
M_{cc}^{CH3}	+	0.688	−0.065	1.673	0.011	−0.003	0.001	$1.42 \cdot 10^{-4}$	$-1.2 \cdot 10^{-5}$
M_{ab}^{CH3}	+	0.731	−4.430	0.578	−0.131	0.022	−0.002	$-3.13 \cdot 10^{-4}$	$4.85 \cdot 10^{-8}$
M_{ba}^{CH3}	+	0.150	−1.325	0.083	−0.021	−0.002	$-4.36 \cdot 10^{-4}$	$-5.73 \cdot 10^{-5}$	$-3.6 \cdot 10^{-6}$
M_{ac}^{CH3}	−	0	4.690	−0.605	0.128	−0.024	0.002	$1.16 \cdot 10^{-4}$	0
M_{ca}^{CH3}	−	0	1.342	−0.086	0.019	0.003	$4.02 \cdot 10^{-4}$	$1.06 \cdot 10^{-4}$	0
M_{bc}^{CH3}	−	0	$5.38 \cdot 10^{-5}$	1.721	0.013	−0.002	0.001	0	0
M_{cb}^{CH3}	−	0	0.055	1.614	0.016	−0.003	0.001	$1.43 \cdot 10^{-4}$	0
M_{aa}^{OH}	+	13.305	0	0	−0.380	0	0	−0.001	0
M_{bb}^{OH}	+	0.659	0	0	0.004	0	0	$1.71 \cdot 10^{-4}$	0
M_{cc}^{OH}	+	2.935	0	0	−0.048	0	0	$-1.26 \cdot 10^{-4}$	0
M_{ab}^{OH}	+	6.139	0	0	−0.048	0	0	$-1.79 \cdot 10^{-4}$	0
M_{ba}^{OH}	+	1.461	0	0	−0.032	0	0	$-3.98 \cdot 10^{-4}$	0
M_{ac}^{OH}	−	0	0	0	0.002	0	0	$-4.03 \cdot 10^{-4}$	0
M_{ca}^{OH}	−	0	0	0	0.067	0	0	$5.24 \cdot 10^{-4}$	0
M_{bc}^{OH}	−	0	0	0	−0.049	0	0	$-2.45 \cdot 10^{-4}$	0
M_{cb}^{OH}	−	0	0	0	0.002	0	0	$4.72 \cdot 10^{-5}$	0

TABLE II. Coefficients a_n^{nuc} in the Fourier expansion describing the γ dependence of the nuclear contribution to the spin-torsion coupling vectors $\boldsymbol{d}_K(\gamma)$ calculated from the nuclear coordinates. The four coefficients a_0^{el} of the γ-independent electronic contribution, as well as one a_1^{el} coefficient, are obtained from a fit to measured hyperfine spectra, see text. The components of $\boldsymbol{d}_K$ are defined with respect to the principal axes a, b, and c. Their γ dependence is expanded in functions $\cos n\gamma$ terms or $\sin n\gamma$ for + and − symmetry, respectively. The superscripts CH_3 and OH refer to the CH_3 protons (K = 1, 2, 3) and OH proton (K = 4), respectively. Results are given only for the CH_3 proton with K = 1, the values for K = 2, 3 correspond to a change of γ by 120° and 240°. All spin-torsion coupling expansion coefficients a_n and the coefficients a_n^{Th} of the Thomas precession corrections $\boldsymbol{q}_K/I_\gamma$ are given in kHz.

	Symmetry	a_0^{nuc}	a_1^{nuc}	a_3^{nuc}	a_6^{nuc}	a_0^{el}	a_1^{el}	$a_0^{\text{Th}}(\approx a_6^{\text{Th}})$
d_a^{CH3}	+	80.00	0.319	$1.40 \cdot 10^{-5}$	0	−66.41	−2.76	$-1.13 \cdot 10^{-8}$
d_b^{CH3}	+	4.435	−9.549	0	0	−10.16	0	$-2.91 \cdot 10^{-6}$
d_c^{CH3}	−	0	0	−9.44	0	0	0	0
d_a^{OH}	+	11.66	0	$-6.79 \cdot 10^{-2}$	$-3.45 \cdot 10^{-4}$	−0.462	0	0
d_b^{OH}	+	21.48	0	$-9.49 \cdot 10^{-2}$	$4.78 \cdot 10^{-4}$	−53.99	0	0
d_c^{OH}	−	0	0	0.122	$6.06 \cdot 10^{-4}$	0	0	0

for the spin-torsion coupling vectors $\boldsymbol{d}_K(\gamma)$ are listed in Tables I and II, respectively. Also the values computed for the corresponding Thomas-precession corrections are given in these tables. We found that the Thomas corrections are several orders of magnitude smaller than the spin-rotation tensors and spin-torsion vectors, so they may be safely neglected. This is perhaps somewhat surprising because the internal rotation in methanol is a large-amplitude internal motion of the molecule far from equilibrium. One must realize, however, that also away from the equilibrium geometry the net force on the CH_3 protons due to the torsional potential is relatively small (the barrier is only 374 cm $^{-1}$ = 0.0017 hartree) in comparison with the Coulomb interactions between the individual nuclei and electrons. The *ab initio* calculated dipole moment vector is given in Table III. All tensor and vector components are defined in the principal axes frame MF.

B. Fit and comparison with experiment

The hyperfine structure in four rotational transitions of methanol was measured in 1973 by Heuvel and Dymanus.[11] Hyperfine spectra for the same and several other rotational transitions were recently reported by Coudert *et al.*[8] The spectra of Coudert *et al.*[8] were obtained by Fourier-transform microwave spectroscopy and they basically show the same spectrum twice. The two spectra should be nearly identical, in principle, but they are separated by a constant frequency due to the Doppler shift between the absorption of the microwave beams that propagate parallel and antiparallel to the molecular beam. Table I in Ref. 8 gives an overview of the measured transitions. All transitions refer to the torsional ground state (v_τ = 0) with σ = 0 and ±1 for levels of A and E symmetry, respectively. The quantum number K_c in the label of an A state with given J_{Ka} may adopt two values, which correspond to rotational levels of A_1 and A_2 symmetry or, in other words, to the parity of the torsion-rotation states under $(23)^*$, cf. Eq. (21).

TABLE III. Coefficients a_n in the Fourier expansion of the dipole vector, in units ea_0. Components are defined in the principal axis frame. Their γ dependence is expanded in functions $\cos n\gamma$ or $\sin n\gamma$ for + and − symmetry, respectively.

	Symmetry	a_0	a_3	a_6
μ_a	+	−0.3678	0.001 706	$5.392 \cdot 10^{-6}$
μ_b	+	−0.5635	−0.011 71	$2.665 \cdot 10^{-5}$
μ_c	−	0	0.011 13	$2.528 \cdot 10^{-5}$

In our calculations of the hyperfine spectra, we address the same transitions. We find that each rotational transition actually splits into many more hyperfine lines than resolved in the measured spectra. Hence, we could not fit our unknown spin-torsion coupling parameters directly to the measured spectra. The same problem was encountered in the fits of these spectra by Coudert *et al.*[8] who determined only the largest two components of the spin-rotation coupling and spin-torsion coupling tensors for the CH_3 and OH protons by fitting the gap between two broad peaks in the measured spectra, each corresponding to several hyperfine transitions. We follow the same procedure, but we kept all spin-rotation coupling parameters fixed at the *ab initio* calculated values, as well as the nuclear contributions to the spin-torsion coupling vectors, while we fitted the electronic contributions to the a and b components of these vectors for the CH_3 and OH protons. The spectra used in our fit correspond to the $5_{15}A_2 \leftarrow 6_{06}A_1$ and $3_2 \leftarrow 3_1E$ transitions, as they both are $\Delta K_a \neq 0$ transitions, which makes them sensitive to spin-torsion interaction. After exploratory investigations of the effects of the fit parameters on the calculated spectra, the torsion-independent contributions to the components $d_a^{\text{CH}_3}$, $d_b^{\text{CH}_3}$, d_a^{OH}, and d_b^{OH} of the electronic spin-torsion vectors were varied in the ranges of [77.5, 57.5], [34.05, 25.95], [6.3, 0], and [75, 50] kHz, respectively, and the $\cos(\gamma)$ dependent contribution to $d_a^{\text{CH}_3}$ in the range of [30, 30] kHz. In the fit of the $5_{15}A_2 \leftarrow 6_{06}A_1$ spectrum, we used the Doppler-shifted spectrum at lower frequency and in the fit of the $3_2 \leftarrow 3_1E$ spectrum the higher frequency spectrum. The Gaussian and Lorentzian line width parameters σ and γ were estimated from the experimental spectra and kept constant in the fits. The fit was performed in two steps. First we roughly determined the minimum in the absolute deviation between our calculated and the measured spectra by making 50 000 random searches in the parameter space defined by an equidistant grid in each of the ranges. Next, in order to refine

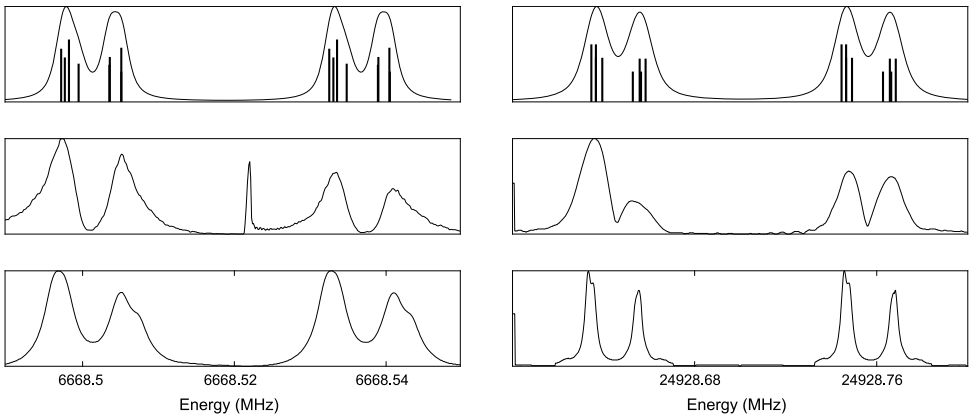

(a) $5_{15}\ A_2 \leftarrow 6_{06}\ A_1$ (b) $3_2\ E \leftarrow 3_1\ E$

FIG. 1. Comparison spectra calculated (upper) for the A and E levels with the measured spectra (middle)[8,11] and the fit by Coudert *et al.*[8] (bottom). The $5_{15}\ A_2 \leftarrow 6_{06}\ A_1$ and $3_2\ E \leftarrow 3_1\ E$ transitions are observed by Coudert *et al.*[8] with Doppler splittings of 35.37 kHz and 109.89 kHz, respectively. The narrow peak in the center of the measured spectrum for the $5_{15}\ A_2 \leftarrow 6_{06}\ A_1$ transition is an experimental artefact.[8] The blue bars indicate the individual hyperfine transitions with a length proportional to the intensity. The hyperfine transitions are convoluted using a Voigt profile with Gaussian width σ = 0.5 kHz and Lorentz width γ = 0.88 kHz for the $5_{15}\ A_2 \leftarrow 6_{06}\ A_1$ transition and σ = 2.5 kHz and γ = 4.0 kHz for the $3_2\ E \leftarrow 3_1\ E$ transition.

this minimum, we made 5000 search steps on a more restricted but finer grid around the minimum found in the first step.

The parameters for the electronic contributions to the spin-torsion interaction extracted from the fit are included in Table II. Figure 1 shows our fitted and measured spectra, as well as the spectra from the fit by Coudert *et al.*[8] The figures also show our calculated line spectra (blue bars) with the heights of the lines given by the calculated relative intensities. Our fitted spectra are generated by the convolution of these line spectra with a Voigt profile.

The general form of each of the two Doppler components in both spectra is well reproduced. For the $5_{15}\ A_2 \leftarrow 6_{06}\ A_1$ transition we find two peaks in each component, with the low-frequency peak being slightly stronger, separated in frequency by a similar amount as the two peaks in the experimental spectrum. For the $3_2\ E \leftarrow 3_1\ E$ transition we also find two peaks, with the low-frequency peak also being slightly stronger, and again a frequency separation similar to experiment. The fit of Coudert *et al.* predicts this as well, although, in their case the individual hyperfine transitions seem to be more closely spaced which produces narrower peaks. In both experimental spectra, the two components of the Doppler doublet are different in intensity, while in the spectrum for the $3_2\ E \leftarrow 3_1\ E$ transition also the relative intensity of the two peaks differs between the two Doppler components.

The parameters in Table II show that the electronic contributions to the spin-torsion coupling vectors, all have a sign that is opposite to the sign of the corresponding *ab initio* calculated nuclear contributions, so they partly cancel each other. This is what one would expect, but it was not found in the fit of Coudert *et al.*,[8] where the electronic contributions had the same sign as the corresponding nuclear contributions and about the same magnitude. Moreover, we recall that we kept our *ab initio* calculated values for the spin-rotation and magnetic dipole-dipole coupling tensors, i.e., we did not include those in our fit. Thus, we could fit all constant components of the electronic spin-torsion coupling vectors and part of their torsional dependence, whereas Coudert *et al.* fitted only the constant a-components of the coupling tensors. The fit values reveal interesting information, for instance, that the largest electronic contribution to the spin-torsion coupling vector $\boldsymbol{d}^{\mathrm{OH}}$ is the component along the b-axis. Table IV lists the expectation values of the operators $\hat{O}_K^{\mathrm{SR}}$, $\hat{O}_K^{\mathrm{ST}}$, and $\hat{O}_{KL}^{\mathrm{DD}}$ over the rotational states $J_{K_a K_c}^{v_\tau=0}$ of A symmetry computed with our *ab initio* calculated and fitted coupling parameters.

Spectra measured for other A and E symmetry transitions are simulated with the hyperfine levels and transition intensities computed with our *ab initio* calculated and fitted coupling parameters. Spectra for three A-symmetry transitions are shown in Fig. 2 and spectra for three of the E symmetry transitions in Fig. 3. More transitions analyzed are given in Fig. 4 and in the supplementary material. Note that the spectra for the A symmetry transitions in Fig. 2 were measured by Heuvel and Dymanus[11] and the figures show only a single spectrum, while the spectra for the E symmetry transitions in Fig. 3 were measured by microwave spectroscopy and the figures show the two Doppler-component spectra. In our discussion of the latter spectra, we refer only to the structure of a single Doppler component.

TABLE IV. Expectation values of the operators in Eqs. (27), (28), and (30) over torsion-rotation states of A symmetry. We used the *ab initio* data of Table I the fitted data from Table II and compute dipole-dipole interactions from the geometry. The subscripts CH_3 and OH of the dipole-dipole coupling operator denote the coupling between two CH_3 protons and the coupling between the OH proton and one of the CH_3 protons, respectively.

J_{KaKc}	$O_{1,2,3}^{\mathrm{SR}}$	$O_{1,2,3}^{\mathrm{ST}}$	O_4^{SR}	O_4^{ST}	$O_{\mathrm{CH_3}}^{\mathrm{DD}}$	$O_{\mathrm{OH}}^{\mathrm{DD}}$
1_{01}	0.632	−0.001	1.785	−0.006	−4.206	2.400
1_{11}	6.602	4.078	7.950	−7.960	2.094	−1.113
1_{10}	6.547	4.077	6.916	−7.967	2.112	−1.293
2_{12}	2.640	1.353	4.185	−2.693	−0.503	0.308
2_{11}	2.585	1.352	3.150	−2.700	−0.499	0.265
3_{13}	1.650	0.671	3.245	−1.376	−0.351	0.210
3_{12}	1.595	0.670	2.210	−1.383	−0.349	0.191
5_{15}	1.056	0.263	2.685	−0.585	−0.162	0.096
6_{06}	0.631	−0.001	1.763	−0.006	−0.127	0.073
6_{15}	0.943	0.185	2.580	−0.434	−0.119	0.070
6_{16}	0.888	0.184	1.546	−0.442	−0.118	0.065

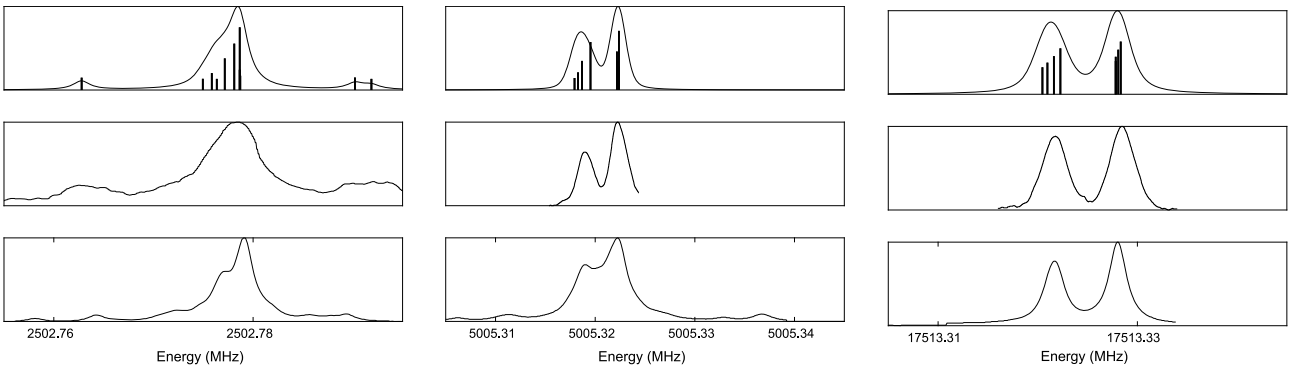

(a) $2_{11}\ A_2 \leftarrow 2_{12}\ A_1$ (b) $3_{12}\ A_2 \leftarrow 3_{13}\ A_1$ (c) $6_{15}\ A_2 \leftarrow\ 6_{16} A_1$

FIG. 2. Comparison of our hyperfine spectra calculated (upper) for the *A* levels with the measured spectra (middle)[11] and the fit by Coudert *et al.*[8] (bottom). The blue bars indicate the individual hyperfine transitions with a length proportional to the intensity. The hyperfine transitions are convoluted using a Voigt profile with $\sigma = 0.11$ kHz and $\gamma = 1.0$ kHz for the $2_{11}\ A_2 \leftarrow 2_{12}\ A_1$ transition, $\sigma = 0.63$ kHz and $\gamma = 0.3$ kHz for the $3_{12}\ A_2 \leftarrow 3_{13}\ A_1$ transition, and $\sigma = 0.767$ kHz and $\gamma = 0.9$ kHz for the $6_{15}\ A_2 \leftarrow 6_{16}\ A_1$ transition.

For all of the hyperfine transitions of *A* symmetry, we observe good agreement between the calculated and measured hyperfine spectra. In the $2_{11}\ A_2 \leftarrow 2_{12}\ A_1$ spectrum, we even reproduce the satellite peaks at the correct frequencies, and also find an asymmetric central peak. Also Coudert *et al.* reproduce these transitions very well in their fits. For the $3_{12}\ A_2 \leftarrow 3_{13}\ A_1$ transition our results seem to be slightly better because the two peaks are more separated, just as in the experimental spectrum.

For the transitions of *E* symmetry the agreement is slightly worse, but the resolution in the experimental spectra seems to be lower for these transitions. In the $2_1\ E \leftarrow 3_0\ E$ spectrum, the experiment shows a single peak with a satellite on the high-frequency side. Coudert *et al.* find a single peak in their simulated spectrum, while we find a satellite peak at higher frequency, although much stronger than seen in experiment. For the $4_2\ E \leftarrow 4_1\ E$ transition, the measured spectrum shows a strong peak with a side peak at about 40% of the intensity. Coudert *et al.* theoretically predict two equally strong peaks with similar intensity. We find a spread-out group of hyperfine lines, about as wide as the experimental spectrum. The experimental $5_2\ E \leftarrow 5_1\ E$ spectrum shows much noise and only a single peak could be resolved. In our simulations, we find the hyperfine transitions to be tightly grouped around the rotational frequency, which is compatible with the structure in the experimental spectrum. Coudert *et al.* compute two peaks within the width of the experimental peak.

In Fig. 4 we show some further *E* symmetry transitions for which microwave spectra were measured both in Lille and in Hannover.[8] The middle figures give both experimental spectra, with the spectra from Hannover and Lille depicted in red and blue, respectively. Since the spectra look different, we also simulated two spectra for each transition. In the two simulations, we used the same line frequencies and intensities calculated directly from our coupling parameters, but we applied a different Doppler shift in accordance with the measured shifts, and we used different parameters for the Voigt profile used in the convolution of our line spectra.

Comparing the measured spectra for the $2_0\ E \leftarrow 3_{-1}\ E$ transition, we observe that the Lille experiments show only a single peak with a small dip in the top, whereas the Hannover experiments show two peaks with the high frequency peak

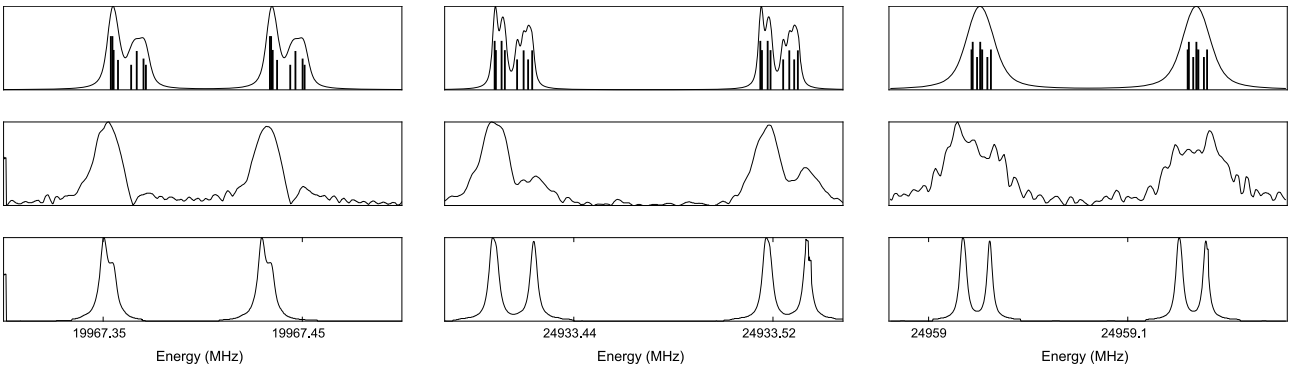

(a) $2_1\ E \leftarrow 3_0\ E$ (b) $4_2\ E \leftarrow 4_1\ E$ (c) $5_2\ E \leftarrow 5_1\ E$

FIG. 3. Comparison of our hyperfine spectra calculated (upper) for the *E* levels with the measured spectra (middle)[8] and the fit by Coudert *et al.*[8] (bottom). The $2_1\ E - 3_0\ E$, $4_2\ E \leftarrow 4_1\ E$, and $8_{-2}\ E \leftarrow 9_{-1}\ E$ transitions are observed by Coudert *et al.*[8] and have a Doppler splitting of 79.78 kHz, 106.81 kHz, and 108.57 kHz. The blue bars indicate the individual hyperfine transitions with a length proportional to the intensity. The hyperfine transitions are convoluted using a Voigt profile with $\sigma = 1.5$ kHz and $\gamma = 1.88$ kHz for the $2_1\ E \leftarrow 3_0\ E$ transition, $\sigma = 0.5$ kHz and $\gamma = 0.88$ kHz for the $4_2\ E \leftarrow 4_1\ E$ transition, and $\sigma = 3.5$ kHz and $\gamma = 4.25$ kHz for the $5_2\ E \leftarrow 5_1\ E$ transition.

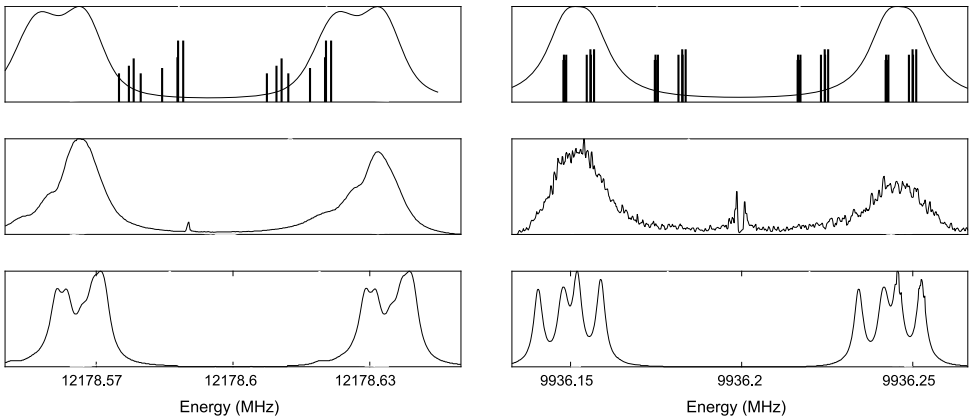

(a) $2_0\ E \leftarrow 3_{-1}\ E$ (b) $9_{-1}\ E \leftarrow 8_{-2}\ E$

FIG. 4. Comparison of our hyperfine spectra calculated (upper) for the *E* levels with the measured spectra (middle)[8] and the fit by Coudert *et al.*[8] (bottom). The spectra were observed in Hannover (red) and Lille[8] (blue). The blue bars indicate the individual hyperfine transitions with a length proportional to the intensity; for clarity they are only given for the $2_0\ E - 3_{-1}\ E$ transition in our simulations of the Hannover spectrum. The Hannover spectra for the $2_0\ E \leftarrow 3_{-1}\ E$ and $9_{-1}\ E \leftarrow 8_{-2}\ E$ transitions are simulated by using a Voigt profile of $\sigma = 0.5$ kHz and $\gamma = 0.88$ and 2.88 kHz and by using a Doppler splitting of 32.4 and 41.67 kHz. The Lille spectra for the $2_0\ E \leftarrow 3_{-1}\ E$ and $9_{-1}\ E \leftarrow 8_{-2}\ E$ transitions are simulated by using a Voigt profile with $\sigma = 4.5$ and 0.5 kHz and $\gamma = 3.88$ and 6.50 kHz and by using a Doppler splitting of 65.44 and 94.11 kHz.

being weaker. Comparing the two experimental spectra for the $9_{-1}\ E \leftarrow 8_{-2}\ E$ transition, we observe multiple peaks in the seemingly better resolved spectrum from Hannover, and only a single broad peak in the spectrum from Lille. However, the multiple peaks in the Hannover spectrum cover a wider range of frequencies than the single peak in the Lille spectrum, and there is a marked difference between the two Doppler components that should be nearly identical. This difference is most pronounced in the Hannover spectrum. So, it seems that there were some experimental problems in recording these spectra. Given these uncertainties in the experimental spectra, a detailed comparison with our calculated spectra is not very meaningful. All we can say is that the structure in our calculated spectra is probably compatible with the measured results.

In a recent paper of Belov *et al.*[21] on Lamb-dip submillimeter-wave spectra of high-*J* torsion-rotation transitions of *E*-symmetry in methanol, they found unexpectedly large doublet splittings in the spectra due to hyperfine coupling. They could explain these doublet splittings by a theoretical model that includes only the spin-rotation coupling within the CH_3 subunit, with operators that depend on the torsion angle. The separation between the doublet peaks was observed for transitions between the rotational levels with *J* ranging from 13 to 34. Extrapolation of the results to lower *J* values with the aid of their model would yield a doublet separation of 17 kHz in the $9_{-1}\ E \leftarrow 8_{-2}\ E$ spectrum.[37] The middle panel of Fig. 4(b) shows, however, that such a doublet structure was not observed in the microwave spectra taken in Hannover and Lille. As shown in the upper panel of Fig. 4(b), our calculations with the full hyperfine coupling Hamiltonian including torsion-angle dependent spin-rotation, spin-torsion, and spin-spin interactions predict two sets of closely spaced lines. These lines, when not individually resolved, do give rise to a doublet structure, with a separation of about 7.5 kHz between the two peaks.

A complete set of tables with our calculated transition frequencies and Einstein *A*-coefficients of all hyperfine transitions associated with the different rotational transitions discussed in the paper is given in the supplementary material. Inspection of these tables shows clearly that for each rotational transition with given $\Delta J = 0$ or ± 1 only the hyperfine transitions with $\Delta F = \Delta J$ have substantial intensities, while the other hyperfine components are weaker by about an order of magnitude. So, the spectra are strongly dominated by these particular hyperfine transitions, which are shown as the line spectra in our figures.

Concluding this section, we note that with most of the dipole-dipole, spin-rotation, and spin-torsion coupling parameters from *ab initio* calculations and only the electronic contribution to the dominant spin-torsion parameters obtained from a fit to two experimental spectra—one for an *A* symmetry transition and one for an *E* symmetry transition—we obtain good agreement with these spectra, as well as with another set of measured spectra not used in the fit. One should realize, however, that the individual hyperfine transitions were not resolved in the measured spectra, which limits the amount of experimental data that we could use in our fit. There may be a relatively large uncertainty in the fitted spin-torsion coupling parameters, which can only be reduced when more of the detailed hyperfine structure in the spectra that we predict will actually be resolved.

V. DISCUSSION

In order to understand the structure in the hyperfine spectra, it is useful to consider the nature of the hyperfine splittings of the torsion-rotation levels. Figures 5(a) and 5(b) illustrate these splittings for two torsion-rotation levels, one of *A* symmetry and one of *E* symmetry. The hyperfine levels were computed with the parameters listed in Tables I and II. The middle column in these figures shows the effect of the couplings involving the CH_3 protons, the righthand column shows the additional splittings when also the interactions with the OH proton are included. The intermediate quantum number F_1 is obtained by coupling the overall rotation angular momentum *J* with the collective nuclear spin I_{123} of the three CH_3 protons. We mentioned above that $I_{123} = 3/2$ for *A* symmetry states,

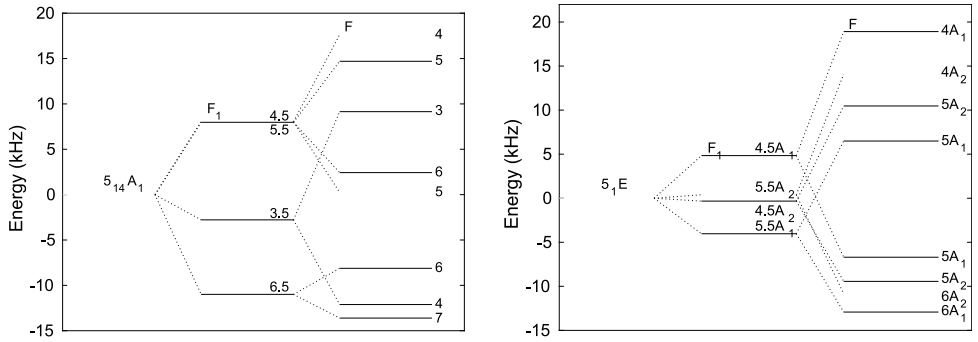

(a) Splitting of torsion-rotation level 5_{14} A_1. (b) Splitting of torsion-rotation level 5_1 E.

FIG. 5. Hyperfine splitting of torsion-rotation A and E levels. The middle column shows the effects of the interactions involving the CH_3-protons, with the intermediate quantum number F_1 explained in the text, the righthand column the final hyperfine levels labeled with the quantum number F.

so that for $J \geq 2$ we obtain four different F_1 values ranging from J 3/2 to J + 3/2. The additional coupling with the spin $I_4 = 1/2$ of the OH proton then yields five different F values ranging from J 2 to $J + 2$, with the intermediate values of F occurring twice and the largest and smallest F value only once. For states of E symmetry $I_{123} = 1/2$, so that only two different values of F_1 are obtained. Additional coupling with $I_4 = 1/2$ then yields three F values: J 1, J, $J + 1$, with two hyperfine states for $F = J$ and only a single one for $F = J \pm 1$. However, the irrep E carries two spatial and two nuclear spin wave functions which may be combined to a total wave function of A_1 or A_2 symmetry, see Eq. (23) in Sec. II C. Each angular momentum coupling scheme then yields two Pauli-allowed states.

Since the distance between the OH proton and each of the CH_3 protons is much larger than the distance between the protons within the CH_3 group, one might expect that the largest splitting between the hyperfine levels originates from the interactions within the CH_3 group, and that the coupling with the OH proton only causes further small splittings. The actual picture is more subtle, however. The magnetic dipole-dipole interactions are indeed stronger between the CH_3 protons than between the OH proton and the CH_3 protons. Tables I and IV show that the spin-rotation interactions are of the same magnitude for CH_3 and OH protons. However, the spin-torsion interactions are stronger for the OH proton than for the CH_3 protons, and they counteract the spin-rotation interactions. As a result we find for states of A symmetry that the hyperfine splitting due to the CH_3-protons is of the same magnitude as the additional splittings caused by the OH proton. For states of E symmetry the interactions involving the OH proton dominate the hyperfine splittings.

An additional important factor that determines the structure of the hyperfine spectra is the transition line strengths. Transitions are allowed for $\Delta F = 0, \pm 1$, but we find, in agreement with the experience from the experimental data, that the hyperfine components of a given rotational transition ΔJ are considerably stronger for transitions with $\Delta F = \Delta J$ than for the other allowed transitions. Only those lines will be visible in the measured hyperfine spectra, which yield a considerable simplification of these spectra.

The expressions that we derived for the spin-rotation coupling tensors $\boldsymbol{M}_K$ and spin-torsion coupling tensors $\boldsymbol{d}_K$ differ from the expressions presented by Heuvel *et al.*[10] and used also by Coudert *et al.*[8] The main difference is that in the formulas of Heuvel *et al.* for these tensors a Thomas precession factor appears in the relative velocity vectors of the interacting particles. Furthermore, we found a sign difference in one of the terms in the hyperfine Hamiltonian. We checked the importance of such a Thomas correction factor in the calculations of the nuclear contributions to the coupling tensors and conclude that it has a substantial effect on the calculated results. Even more so, since the Thomas correction factor was written by Heuvel *et al.* as $\gamma_K = Z_K M_p/(g_K M_K)$ (for protons ≈ 0.18), instead of $\gamma_K = 1 - Z_K M_p/(g_K M_K)$ (for protons ≈ 0.82), as it should be.[15] Explicit derivations[15,19,20] have shown, however, that the Thomas precession correction vanishes completely for molecules at equilibrium, and that it should be included in a different manner for molecules that deviate from their equilibrium geometry. In the present paper, we use $\gamma_K = 1$ and obtain the Thomas correction to both the spin-rotation and spin-torsion coupling tensors with formulas that we derived specifically for molecules with large amplitude internal rotation, such as methanol. Application of these formulas shows that the Thomas corrections are negligibly small, so that also our numerical results differ substantially from those of Coudert *et al.*[8]

VI. CONCLUSION

Expressions for the spin-rotation and spin-torsion coupling terms in the hyperfine Hamiltonian for molecules with internal rotation are derived from first principles. The spin-rotation coupling Hamiltonian contains not only the usual term with the rotational angular momentum operator $\hat{\boldsymbol{J}}$—which is the spin-rotation coupling term in the hyperfine Hamiltonian for semi-rigid molecules—but also a term that contains the torsional angular momentum operator $\hat{p}_\gamma$. Vice-versa, the spin-torsion coupling Hamiltonian—present only for molecules with internal rotation—contains not only a term with $\hat{p}_\gamma$ but also a term with $\hat{\boldsymbol{J}}$. This hyperfine Hamiltonian was derived previously by Heuvel and Dymanus,[10] but our result is essentially different from theirs especially in the way to treat the relativistic Thomas precession correction. In the Hamiltonian of Heuvel and Dymanus this correction was taken into account by putting a scaling factor into the relative velocity vectors of the interacting particles, which has a substantial effect on the

calculated results. However, it was shown in a paper by Flygare[15] that the Thomas correction actually vanishes for the molecules at equilibrium and in some later papers on diatomic molecules[18–20] that it is very small for the molecules that vibrate about their equilibrium geometry. Here, we derive a formula for the Thomas correction to the spin-rotation and spin-torsion coupling in molecules with internal rotation. Application of this formula shows that also for methanol the Thomas correction is negligibly small, even though the molecule exerts an internal rotation far from equilibrium.

Most of the coupling parameters in the hyperfine Hamiltonian for methanol could be obtained from *ab initio* electronic structure calculations at the CCSD(T) level with the program CFOUR.[25] The electronic contribution to the spin-torsion coupling parameters could not be obtained in this manner, however. So we fitted the missing spin-torsion parameters by computations of the hyperfine levels and transition intensities for the $5_{15}\,A_2 \leftarrow 6_{06}\,A_1$ and $3_2\,E \leftarrow 3_1\,E$ rotational transitions in methanol and compared with the measured spectra[8] in which the hyperfine structure in the spectrum is partly resolved. With the obtained hyperfine parameters, we calculated the hyperfine structure in the spectra for several other rotational transitions between the torsional states of both *A* and *E* symmetry, and find that also they agree well with the measured spectra of Heuvel and Dymanus[11] and Coudert *et al.*[8] In contrast with the work of Coudert *et al.*[8] where the dominant spin-rotation coupling parameters were included in the fit and were found to deviate substantially from the *ab initio* calculated values, we kept the *ab initio* values and did not include these parameters in our fit. Another difference between our work and Ref. 8 is that in our case the fitted electronic contributions to the spin-torsion coupling parameters partly cancel the nuclear contributions, i.e., they have opposite signs as expected, whereas it was found in Ref. 8 that these contributions are about equal in magnitude and have the same sign, which seems unphysical.

Currently we are using our results obtained for the hyperfine Hamiltonian of methanol in calculations of the Zeeman splittings of the hyperfine transitions by external magnetic fields. Quantitative information on these magnetic field effects is relevant for the analysis of astrophysical data, such as the methanol maser spectra from star-forming regions. This work will be reported in a forthcoming publication.

SUPPLEMENTARY MATERIAL

See supplementary material for figures of other spectra analyzed and tables with all calculated hyperfine transition frequencies and intensities.

ACKNOWLEDGMENTS

We thank Li-Hong Xu for providing the source code of her extended version of the program BELGI, and Laurent Coudert and Jens-Uwe Grabow for making available their results prior to publication. We are grateful to Jon Hougen for reading our manuscript and for valuable comments. We acknowledge useful discussions with Huib Jan van Langevelde, Wouter Vlemmings, and Gabriele Surcis. This work was partially supported by the Swedish Research Council (VR).

APPENDIX A: THEORY

1. Kinetic energy operator

As usual for molecules with internal rotation, we distinguish two parts in the molecule that are internally rigid. The "frame" part consists of those nuclei that remain fixed in the molecule-fixed (MF) principal axis frame, in the case of methanol the OH fragment. The origin of the MF frame is the center of mass of the CH_3OH molecule and its orientation with respect to a space-fixed (SF) frame is defined by three *zyz*-Euler angles (χ, θ, ϕ). The "top" part is fixed with respect to a frame TF that rotates with respect to the MF frame about a single (fixed) axis $\boldsymbol{\lambda}$ over an angle γ. This "top" is considered to be a symmetric rotor, such as the CH_3 group in methanol. The coordinates of the nuclei in the "frame" and "top" with respect to the SF frame are given by

$$\begin{aligned} \boldsymbol{r}_K^{\text{frame,SF}} &= \boldsymbol{R}^{-1}(\chi,\theta,\phi)\boldsymbol{r}_K^{\text{frame,MF}}, \\ \boldsymbol{r}_K^{\text{top,SF}} &= \boldsymbol{R}^{-1}(\chi,\theta,\phi)\boldsymbol{R}^{-1}(\boldsymbol{\lambda},\gamma)\boldsymbol{r}_K^{\text{top,TF}}, \end{aligned} \tag{A1}$$

where $\boldsymbol{R}(\chi,\theta,\phi)$ is a rotation over the *zyz*-Euler angles and $\boldsymbol{R}(\boldsymbol{\lambda},\gamma)$ is a rotation over γ about the axis $\boldsymbol{\lambda}$, and the nuclear coordinates $\boldsymbol{r}_K^{\text{frame,MF}}$ and $\boldsymbol{r}_K^{\text{top,TF}}$ are fixed with respect to their respective frames. The time-derivatives of the SF nuclear positions are related to the time-independent MF and TF atomic coordinates

$$\begin{aligned} \dot{\boldsymbol{r}}_K^{\text{frame,SF}} &= \dot{\boldsymbol{R}}^{-1}(\chi,\theta,\phi)\boldsymbol{r}_K^{\text{frame,MF}}, \\ \dot{\boldsymbol{r}}_K^{\text{top,SF}} &= \dot{\boldsymbol{R}}^{-1}(\chi,\theta,\phi)\boldsymbol{R}^{-1}(\boldsymbol{\lambda},\gamma)\boldsymbol{r}_K^{\text{top,TF}} \\ &\quad + \boldsymbol{R}^{-1}(\chi,\theta,\phi)\dot{\boldsymbol{R}}^{-1}(\boldsymbol{\lambda},\gamma)\boldsymbol{r}_K^{\text{top,TF}}. \end{aligned} \tag{A2}$$

The SF derivatives, transformed to the MF frame for the nuclei in the "frame" and to the TF frame for the nuclei in the "top," can also be expressed as

$$\begin{aligned} \boldsymbol{R}(\chi,\theta,\phi)\dot{\boldsymbol{r}}_K^{\text{frame,SF}} &= \boldsymbol{\omega}\times\boldsymbol{r}_K^{\text{frame,MF}}, \\ \boldsymbol{R}(\boldsymbol{\lambda},\gamma)\boldsymbol{R}(\chi,\theta,\phi)\dot{\boldsymbol{r}}_K^{\text{top,SF}} &= \boldsymbol{\omega}'\times\boldsymbol{r}_K^{\text{top,TF}} + \dot{\gamma}\boldsymbol{\lambda}\times\boldsymbol{r}_K^{\text{top,TF}}, \end{aligned} \tag{A3}$$

in terms of the angular velocities $\boldsymbol{\omega}$, $\dot{\gamma}$, and $\boldsymbol{\omega}' = \boldsymbol{R}(\boldsymbol{\lambda},\gamma)\boldsymbol{\omega}$. The Lagrangian form of the classical kinetic energy in terms of the atomic masses m_K and velocities $\dot{\boldsymbol{r}}_K^{\text{SF}}$ can then be rewritten as

$$2T = \boldsymbol{\omega}^T\boldsymbol{I}\boldsymbol{\omega} + \dot{\gamma}\boldsymbol{\lambda}^T\boldsymbol{I}^{\text{top}}\boldsymbol{\omega} + \dot{\gamma}\boldsymbol{\omega}^T\boldsymbol{I}^{\text{top}}\boldsymbol{\lambda} + I_\gamma\dot{\gamma}^2, \tag{A4}$$

in which $\boldsymbol{I} = \boldsymbol{I}^{\text{frame}} + \boldsymbol{I}^{\text{top}}$ is the overall inertia tensor and $I_\gamma = \boldsymbol{\lambda}^T\boldsymbol{I}^{\text{top}}\boldsymbol{\lambda}$ is the moment of inertia of the top about the internal rotation axis $\boldsymbol{\lambda}$. Since the "top" is a symmetric rotor, its inertia tensor is not changed by the internal rotation, $\boldsymbol{I}^{\text{top}} = \boldsymbol{R}^{-1}(\boldsymbol{\lambda},\gamma)\boldsymbol{I}^{\text{top}}\boldsymbol{R}(\boldsymbol{\lambda},\gamma)$. Also the overall inertia tensor $\boldsymbol{I}$, diagonal in the principal axes frame MF, is therefore invariant under the internal rotation. In Eq. (A4) the components of the vectors $\boldsymbol{\omega}$ and $\boldsymbol{\lambda}$ and of the inertia tensors $\boldsymbol{I}$ and $\boldsymbol{I}^{\text{top}}$ are given relative to the MF frame.

This equation can be written in matrix form as

$$2T = \begin{pmatrix}\boldsymbol{\omega}\\ \dot{\gamma}\end{pmatrix}^T \begin{pmatrix}\boldsymbol{I} & \boldsymbol{I}^{\text{top}}\boldsymbol{\lambda}\\ \boldsymbol{\lambda}^T\boldsymbol{I}^{\text{top}} & I_\gamma\end{pmatrix}\begin{pmatrix}\boldsymbol{\omega}\\ \dot{\gamma}\end{pmatrix}. \tag{A5}$$

In order to derive the quantum mechanical expression for T, one has to convert the Lagrangian in Eq. (A5) into the

corresponding classical Hamiltonian with the angular momenta $\boldsymbol{J}$ and p_γ conjugate to the angular velocities $\boldsymbol{\omega}$ and $\dot{\gamma}$ given by

$$\begin{aligned} \boldsymbol{J} &= \tfrac{\partial T}{\partial \boldsymbol{\omega}} = \boldsymbol{I}\boldsymbol{\omega} + \boldsymbol{I}^{\text{top}}\boldsymbol{\lambda}\dot{\gamma} \\ p_\gamma &= \tfrac{\partial T}{\partial \dot{\gamma}} = \boldsymbol{\omega}\cdot\boldsymbol{I}^{\text{top}}\boldsymbol{\lambda} + I_\gamma\dot{\gamma}. \end{aligned} \tag{A6}$$

After inversion of the 4×4 matrix in Eq. (A5) with the use of a formula in Ref. 38, the angular velocities are expressed in terms of their conjugate momenta

$$\begin{aligned} \boldsymbol{\omega} &= \boldsymbol{I}^{-1}\boldsymbol{J} - 2F\left(p_\gamma - \boldsymbol{\rho}\cdot\boldsymbol{J}\right)\boldsymbol{\rho}, \\ \dot{\gamma} &= 2F\left(p_\gamma - \boldsymbol{\rho}\cdot\boldsymbol{J}\right), \end{aligned} \tag{A7}$$

with

$$F = \frac{1}{2}\left(I_\gamma - \boldsymbol{\rho}^T\boldsymbol{I}\boldsymbol{\rho}\right)^{-1} \qquad \text{and} \qquad \boldsymbol{\rho} = \boldsymbol{I}^{-1}\boldsymbol{I}^{\text{top}}\boldsymbol{\lambda}. \tag{A8}$$

When these results are substituted into Eq. (A5), the Hamiltonian kinetic energy becomes

$$T = \frac{1}{2}\,\boldsymbol{J}\cdot\boldsymbol{I}^{-1}\boldsymbol{J} + F\left(p_\gamma - \boldsymbol{\rho}\cdot\boldsymbol{J}\right)^2. \tag{A9}$$

The quantum mechanical equivalent of this result, given by Hougen *et al.*,[22] is obtained by replacing the total angular momentum $\boldsymbol{J}$ by the operator $\hat{\boldsymbol{J}}$[26] and p_γ by $(\hbar/i)\partial/\partial\gamma$. The components of $\hat{\boldsymbol{J}}$ are defined relative to the MF frame and obey the anomalous commutation relations that hold for body-fixed angular momentum operators.[26]

2. Spin-rotation and spin-torsion interactions

The magnetic field produced at position $\boldsymbol{r}_K$ by a set of moving particles i (nuclei and electrons) with charges $Z_i e$ is given by

$$\boldsymbol{B}_K = \sum_i \frac{Z_i e}{c} r_{Ki}^{-3}\boldsymbol{r}_{Ki}\times\boldsymbol{v}_{Ki}. \tag{A10}$$

The vectors $\boldsymbol{r}_{Ki} = \boldsymbol{r}_i - \boldsymbol{r}_K$ are the relative position vectors of the particles, r_{Ki} is the length of $\boldsymbol{r}_{Ki}$, and $\boldsymbol{v}_{Ki} = \dot{\boldsymbol{r}}_{Ki}$ are their relative velocities. The magnetic moment of nucleus K is $\boldsymbol{\mu}_K = g_K\mu_N\boldsymbol{I}_K$, with $\boldsymbol{I}_K$ denoting the nuclear spin, $\mu_N = e/(2M_p c)$ the nuclear magneton with the proton mass M_p and the speed of light c, and g_K the gyromagnetic factor of nucleus K. Its energy in the field $\boldsymbol{B}_K$ is[17]

$$H_K = -\boldsymbol{B}_K\cdot\boldsymbol{\mu}_K = -\sum_i \frac{Z_i e g_K\mu_N}{c} r_{Ki}^{-3}\left[\boldsymbol{r}_{Ki}\times\boldsymbol{v}_{Ki}\right]\cdot\boldsymbol{I}_K. \tag{A11}$$

In several papers[10,14–16] one takes into account the Thomas precession factor γ_K and replaces the vector $\boldsymbol{v}_{Ki} = \boldsymbol{v}_i - \boldsymbol{v}_K$ by $\boldsymbol{v}_i - \gamma_K\boldsymbol{v}_K$. The correct expression for this factor is[15]

$$\gamma_K = 1 - \frac{Z_K M_p}{g_K M_K}, \tag{A12}$$

but different expressions occur in Refs. 10 and 14. Flygare[15] has shown that for the nuclear spin-rotation coupling in molecules at their equilibrium geometry, the Thomas precession correction vanishes. We omit this correction by using Eq. (A11) without any correction, i.e., by setting $\gamma_K = 1$. In Sec. II B we have shown how it actually has to be dealt with in molecules with internal rotation such as methanol.

The positions of the nuclei in the "frame" and "top" of the molecule are fixed with respect to the MF and TF frame, respectively. Their positions with respect to the SF frame are given by Eq. (A1), and in Eq. (A3) their velocities are expressed in terms of the angular velocity $\boldsymbol{\omega}$ of the whole molecule and the velocity $\dot{\gamma}$ of rotation of the "top" about the axis $\boldsymbol{\lambda}$ relative to the "frame." Substitution of these expressions into Eq. (A11) yields

$$H_K^{\text{frame}} = -\boldsymbol{I}_K\cdot\boldsymbol{W}_K^{\text{frame}}\boldsymbol{\omega} \tag{A13}$$

for the particles i in the "frame," with

$$\boldsymbol{W}_K^{\text{frame}} = \sum_i^{\text{frame}} \frac{Z_i e g_K\mu_N}{c} r_{Ki}^{-3}\left[\left(\boldsymbol{r}_{Ki}^{\text{MF}}\cdot\boldsymbol{r}_{Ki}^{\text{MF}}\right)\mathbf{1} - \boldsymbol{r}_{Ki}^{\text{MF}}\otimes\boldsymbol{r}_{Ki}^{\text{MF}}\right]. \tag{A14}$$

For the particles in the "top" we get

$$H_K^{\text{top}} = -\boldsymbol{I}_K\cdot\boldsymbol{W}_K^{\text{top}}\boldsymbol{\omega}' - \boldsymbol{I}_K\cdot\boldsymbol{w}_K\dot{\gamma}, \tag{A15}$$

with

$$\boldsymbol{W}_K^{\text{top}} = \sum_i^{\text{top}} \frac{Z_i e g_K\mu_N}{c} r_{Ki}^{-3}\left[\left(\boldsymbol{r}_{Ki}^{\text{TF}}\cdot\boldsymbol{r}_{Ki}^{\text{TF}}\right)\mathbf{1} - \boldsymbol{r}_{Ki}^{\text{TF}}\otimes\boldsymbol{r}_{Ki}^{\text{TF}}\right] \tag{A16}$$

and

$$\boldsymbol{w}_K = \sum_i^{\text{top}} \frac{Z_i e g_K\mu_N}{c} r_{Ki}^{-3}\left[\left(\boldsymbol{r}_{Ki}^{\text{TF}}\cdot\boldsymbol{r}_{Ki}^{\text{TF}}\right)\mathbf{1} - \boldsymbol{r}_{Ki}^{\text{TF}}\otimes\boldsymbol{r}_{Ki}^{\text{TF}}\right]\boldsymbol{\lambda}. \tag{A17}$$

All tensor and vector components in Eqs. (A15)–(A17) are defined in the TF frame, while Eqs. (A13) and (A14) are written in the MF frame. We prefer to write all equations in the MF frame, i.e., the principal axes frame of the whole molecule. This can be achieved by transformation to the γ dependent coupling tensor $\boldsymbol{W}_K^{\text{top}}(\gamma) = \boldsymbol{R}(\boldsymbol{\lambda},\gamma)^{-1}\boldsymbol{W}_K^{\text{top}}\boldsymbol{R}(\boldsymbol{\lambda},\gamma)$ and coupling vector $\boldsymbol{w}_K(\gamma) = \boldsymbol{R}(\boldsymbol{\lambda},\gamma)^{-1}\boldsymbol{w}_K$. Equation (A15) then becomes

$$H_K^{\text{top}} = -\boldsymbol{I}_K\cdot\boldsymbol{W}_K^{\text{top}}(\gamma)\boldsymbol{\omega} - \boldsymbol{I}_K\cdot\boldsymbol{w}_K(\gamma)\dot{\gamma}, \tag{A18}$$

in which also the components of $\boldsymbol{I}_K$ and $\boldsymbol{\omega}$ are given in the MF frame. If nucleus K is in the "top," the position vector $\boldsymbol{r}_K$ depends on γ, and so does the coupling tensor $\boldsymbol{W}_K^{\text{frame}}$. Since all tensors and vectors are now given in the MF frame, we may add Eqs. (A13) and (A18) to obtain

$$H_K = -\boldsymbol{I}_K\cdot\boldsymbol{W}_K(\gamma)\boldsymbol{\omega} - \boldsymbol{I}_K\cdot\boldsymbol{w}_K(\gamma)\dot{\gamma}, \tag{A19}$$

with

$$\begin{aligned} \boldsymbol{W}_K(\gamma) &= \boldsymbol{W}_K^{\text{frame}} + \boldsymbol{W}_K^{\text{top}}(\gamma) \\ &= \sum_i \frac{Z_i e g_K\mu_N}{c} r_{Ki}^{-3}\left[\left(\boldsymbol{r}_{Ki}^{\text{MF}}\cdot\boldsymbol{r}_{Ki}^{\text{MF}}\right)\mathbf{1} - \boldsymbol{r}_{Ki}^{\text{MF}}\otimes\boldsymbol{r}_{Ki}^{\text{MF}}\right], \end{aligned} \tag{A20}$$

where we note that the sum over particles i now runs over all electrons and all nuclei other than K in the whole molecule.

Next we replace the angular velocities $\boldsymbol{\omega}$ and $\dot{\gamma}$ in Eq. (A20) by their conjugate angular momenta $\boldsymbol{J}$ and p_γ, with the use of Eq. (A7). With the vector $\boldsymbol{\rho}$ given by Eq. (A8) and replacing the angular momenta $\boldsymbol{J}$, p_γ, and $\boldsymbol{I}_K$ by the corresponding operators, this yields the spin-rotation coupling Hamiltonian in Eq. (3) and the spin-torsion coupling Hamiltonian in Eq. (4).

Finally we note that the coupling tensors given in Eqs. (A17) and (A20) depend on the coordinates of both nuclei

and electrons. The contributions that contain the nuclear coordinates can be directly calculated, since the positions of the nuclei are fixed with respect to the MF frame (for the nuclei in the "frame") or depend only on the torsion angle γ (for the nuclei in the "top"). For the spin-rotation coupling tensors $\boldsymbol{M}_K$, it was shown that the electronic contributions can be obtained from second order perturbation theory[15] with matrix elements over the molecule's ground state and excited electronic wave functions. Calculation of these spin-rotation coupling tensors has been implemented in the electronic structure program package CFOUR,[25] and they can thus be computed as a function of γ. No such implementation yet exists, however, for the spin-torsion coupling tensors $\boldsymbol{w}_K$. Just as in the recent paper of Coudert *et al.*,[8] we calculate the nuclear contributions to the tensors $\boldsymbol{w}_K$ and estimate the electronic contributions from a fit to experimental hyperfine spectra. The notations $\boldsymbol{M}_K$ and $\boldsymbol{w}_K$ for these tensors are used in the main body of this paper for the total nuclear and electronic contributions, unless we specify explicitly the contribution that is meant.

APPENDIX B: ANGULAR MOMENTUM ALGEBRA OF HYPERFINE COUPLING TERMS

A vast amount of literature, summarized by Eshbach and Strandberg[39] and Bowater *et al.*,[40] exists on the matrix elements of hyperfine and Zeeman interactions. In these papers the rotational matrix elements are given in terms of rather cumbersome matrix elements of direction cosines and rotational angular momentum operators. A more general formalism, exemplified here for the angular momentum algebra of the magnetic dipole-dipole and nuclear-spin rotation coupling operators, can be written with spherical tensor operators. The nuclear-spin rotation interaction Hamiltonian for a molecule with nuclei α can be written in SF spherical components as the sum over terms

$$-\hat{\boldsymbol{I}}_\alpha \cdot \boldsymbol{M}_\alpha \hat{\boldsymbol{J}} = \sum_{mm'} (-1)^m (\hat{\boldsymbol{I}}_\alpha)^{\mathrm{SF}}_{-m} (\boldsymbol{M}_\alpha)^{\mathrm{SF}}_{mm'} \hat{J}^{\mathrm{SF}}_{m'}. \tag{B1}$$

The coupling tensor $\boldsymbol{M}_\alpha$ is calculated in the molecular-axes frame MF and can be transformed to the SF frame by the rotation

$$(\boldsymbol{M}_\alpha)^{\mathrm{SF}}_{mm'} = \sum_{kk'} D^{(1)*}_{mk}(\chi,\theta,\phi)(\boldsymbol{M}_\alpha)^{\mathrm{MF}}_{kk'} D^{(1)}_{m'k'}(\chi,\theta,\phi). \tag{B2}$$

We expand the product of the two Wigner D-matrix elements in irreducible components $D^{(L)*}_{PQ}(\chi,\theta,\phi)$, with L adopting the values 0, 1, 2, and $Q = -L, \ldots, L$,

$$\begin{aligned}-\hat{\boldsymbol{I}}_\alpha \cdot \boldsymbol{M}_\alpha \hat{\boldsymbol{J}} = \sum_{LPQ} (-1)^{P+L} \sum_{mm'} (\hat{\boldsymbol{I}}_\alpha)^{\mathrm{SF}}_{-m} \hat{J}^{\mathrm{SF}}_{m'} \\ \times \langle 1\ -m\ 1\ m' | L\ -P\rangle D^{(L)*}_{PQ}(\chi,\theta,\phi) \\ \times \sum_{kk'} (-1)^{1-k'} (\boldsymbol{M}_\alpha)_{kk'} \langle 1\ k\ 1\ -k' | L\ Q\rangle,\end{aligned} \tag{B3}$$

and define the rank-L irreducible components of the coupling tensor as

$$(\boldsymbol{M}_\alpha)_{LQ} = \sum_{kk'} (-1)^{1-k'} (\boldsymbol{M}_\alpha)_{kk'} \langle 1\ k\ 1\ -k' | L\ Q\rangle. \tag{B4}$$

The quantity between angular brackets is a Clebsch-Gordan coefficient.

By evaluating the matrix element $\langle (k_1) j_1 m_1 | D^{(L)*}_{PQ}(\chi,\theta,\phi) | (k_2) j_2 m_2\rangle$ and using the completeness relation[41] twice, we may express the Wigner D-matrix element as

$$\begin{aligned}D^{(L)*}_{PQ}(\chi,\theta,\phi) = \sum_{k_1 j_1 k_2 j_2} \frac{[j_1]^{1/2}[j_2]^{1/2}}{[L]^{1/2}} (-1)^{j_1-k_1} \\ \times \begin{pmatrix} j_1 & L & j_2 \\ -k_1 & Q & k_2 \end{pmatrix} \hat{T}^{(L)}_P(k_1 j_1; k_2 j_2),\end{aligned} \tag{B5}$$

with the rank-L irreducible spherical tensor operator $\hat{\boldsymbol{T}}^{(L)}(j_1; j_2)$ defined by its components[41]

$$\hat{T}^{(L)}_P(j_1; j_2) = \sum_{m_1 m_2} |j_1 m_1\rangle\langle j_2 m_2| (-1)^{j_1-m_1} [L]^{1/2} \begin{pmatrix} j_1 & L & j_2 \\ -m_1 & P & m_2 \end{pmatrix}. \tag{B6}$$

The quantities in round brackets are Wigner 3j symbols and the square brackets are shorthand for $[j] = 2j + 1$. Next we couple the two irreducible tensor operators $\hat{\boldsymbol{I}}_\alpha$ and $\hat{\boldsymbol{J}}$ with the use of the general relation[42]

$$\left[\hat{\boldsymbol{A}}^{(\ell_1)} \otimes \hat{\boldsymbol{B}}^{(\ell_2)}\right]^{(\ell)}_q = \sum_{m_1=-\ell_1}^{\ell_1} \sum_{m_2=-\ell_2}^{\ell_2} \hat{A}_{\ell_1 m_1} \hat{B}_{\ell_2 m_2} \langle \ell_1 m_1 \ell_2 m_2 | \ell q\rangle, \tag{B7}$$

and couple the unit spherical tensor operator in the Wigner D-matrix element to the coupled operator $[\hat{\boldsymbol{I}}_\alpha \otimes \hat{\boldsymbol{J}}]^{(L)}$ to find

$$\begin{aligned}-\hat{\boldsymbol{I}}_\alpha \cdot \boldsymbol{M}_\alpha \hat{\boldsymbol{J}} = \sum_{j_1 j_2 k_1 k_2} (-1)^{j_1-k_1} [j_1]^{1/2}[j_2]^{1/2} \\ \times \sum_L \left[\hat{\boldsymbol{T}}^{(L)}(j_1; j_2) \otimes [\hat{\boldsymbol{I}}_\alpha \otimes \hat{\boldsymbol{J}}]^{(L)}\right]^{(0)}_0 \\ \times \sum_Q \begin{pmatrix} j_1 & L & j_2 \\ -k_1 & Q & k_2 \end{pmatrix} (\boldsymbol{M}_\alpha)_{LQ}.\end{aligned} \tag{B8}$$

Analogously, we obtain for the magnetic dipole-dipole interaction

$$\begin{aligned}\hat{\boldsymbol{I}}_\alpha \cdot \boldsymbol{D}_{\alpha\beta} \hat{\boldsymbol{I}}_\beta = -\sum_{j_1 j_2 k_1 k_2} (-1)^{j_1-k_1} [j_1]^{1/2}[j_2]^{1/2} \\ \times \sum_L \left[\hat{\boldsymbol{T}}^{(L)}(j_1; j_2) \otimes [\hat{\boldsymbol{I}}_\alpha \otimes \hat{\boldsymbol{I}}_\beta]^{(L)}\right]^{(0)}_0 \\ \times \sum_Q \begin{pmatrix} j_1 & L & j_2 \\ -k_1 & Q & k_2 \end{pmatrix} (\boldsymbol{D}_{\alpha\beta})_{LQ}.\end{aligned} \tag{B9}$$

The rotational and nuclear spin angular momentum operators can be written in terms of irreducible spherical tensor operators as

$$\hat{J}_q = \sum_j \sqrt{\frac{[j] j (j+1)}{3}} \hat{T}_{1q}(j, j),$$

$$(\hat{\boldsymbol{I}}_\alpha)_q = \sum_{i_\alpha} \sqrt{\frac{[i_\alpha] i_\alpha (i_\alpha + 1)}{3}} \hat{T}_{1q}(i_\alpha, i_\alpha).$$

Finally, as an example, we evaluate the matrix elements of the operator in Eq. (B9) with $\alpha = 1$ and $\beta = 2$ between coupled basis functions $|[([\{I_1 I_2\} I_{12} I_3] I_{123} I_4) IJ] F\ M_F\rangle$ and $|[([\{I'_1 I'_2\} I'_{12} I'_3] I'_{123} I'_4) I' J'] F\ M_F\rangle$ to find

$$\left\langle [([\{I_1I_2\}I'_{12}I_3]I'_{123}I_4)I'J']F\ M_F \left| \left[\hat{\boldsymbol{T}}^{(L)}(j_1;j_2)\otimes\left[\hat{\boldsymbol{I}}_1\otimes\hat{\boldsymbol{I}}_2\right]^{(L)}\right]_0^{(0)} \right| [([\{I_1I_2\}I_{12}I_3]I_{123}I_4)IJ]F\ M_F \right\rangle$$
$$= (I_1(I_1+1)I_2(I_2+1))^{1/2}[I_1]^{1/2}[I_2]^{1/2}[L]^{1/2}[I'_{12}]^{1/2}[I_{12}]^{1/2}[I'_{123}]^{1/2}[I_{123}]^{1/2}[I']^{1/2}[I]^{1/2}(-1)^{I'_{12}+I_3+I_4+J+F+I_{123}+I'_{123}+I'+I+L}$$
$$\times \begin{Bmatrix} I_1 & I_1 & 1 \\ I_2 & I_2 & 1 \\ I'_{12} & I_{12} & L \end{Bmatrix} \begin{Bmatrix} I_{12} & I'_{12} & L \\ I'_{123} & I_{123} & I_3 \end{Bmatrix} \begin{Bmatrix} I_{123} & I'_{123} & L \\ I' & I & I_4 \end{Bmatrix} \begin{Bmatrix} J' & J & L \\ I & I' & F \end{Bmatrix},$$

where the quantities between the curly brackets are Wigner 9*j* and 6*j* symbols. Matrix elements of the spin-rotation coupling and other dipole-dipole coupling terms can be found analogously.

[1] W. H. T. Vlemmings, Astron. Astrophys. **484**, 773 (2008).
[2] G. Surcis, W. H. T. Vlemmings, H. J. van Langevelde, B. Hutawarakorn Kramer, and L. H. Quiroga-Nuñez, Astron. Astrophys. **556**, A73 (2013).
[3] G. Surcis, W. H. T. Vlemmings, H. J. van Langevelde, and B. Hutawarakorn Kramer, Astron. Astrophys. **541**, A47 (2012).
[4] P. Jansen, L.-H. Xu, I. Kleiner, W. Ubachs, and H. L. Bethlem, Phys. Rev. Lett. **106**, 100801 (2011).
[5] J. Bagdonaite, P. Jansen, C. Henkel, H. L. Bethlem, K. M. Menten, and W. Ubachs, Science **339**, 46 (2013).
[6] J. Bagdonaite, M. Daprà, P. Jansen, H. L. Bethlem, W. Ubachs, S. Muller, C. Henkel, and K. M. Menten, Phys. Rev. Lett. **111**, 231101 (2013).
[7] N. Kanekar, W. Ubachs, K. M. Menten, J. Bagdonaite, A. Brunthaler, C. Henkel, S. Muller, H. L. Bethlem, and M. Daprà, Mon. Not. R. Astron. Soc.: Lett. **448**, L104 (2015).
[8] L. Coudert, C. Gutlé, T. Huet, J.-U. Grabow, and S. Levshakov, J. Chem. Phys. **143**, 044304 (2015).
[9] J. E. M. Heuvel, "Hyperfine structure in internal rotor molecules," Ph.D. thesis, Katholieke Universiteit Nijmegen, 1972.
[10] J. Heuvel and A. Dymanus, J. Mol. Spectrosc. **47**, 363 (1973).
[11] J. Heuvel and A. Dymanus, J. Mol. Spectrosc. **45**, 282 (1973).
[12] J. T. Hougen, W. L. Meerts, and I. Ozier, J. Mol. Spectrosc. **146**, 8 (1991).
[13] L. H. Thomas, Philos. Mag. **3**, 1 (1927).
[14] G. R. Gunther-Mohr, C. H. Townes, and J. A. van Vleck, Phys. Rev. **94**, 1191 (1954).
[15] W. H. Flygare, J. Chem. Phys. **41**, 793 (1964).
[16] P. Thaddeus, L. Krisher, and J. Loubser, J. Chem. Phys. **40**, 257 (1964).
[17] W. Flygare, *Molecular Structure and Dynamics* (Prentice-Hall, Englewood Cliffs, 1978).
[18] J. Gauss and D. Sundholm, Mol. Phys. **91**, 449 (1997).
[19] R. V. Reid and A. H.-M. Chu, Phys. Rev. A **9**, 609 (1974).
[20] T. K. Rebane and M. I. Volodicheva, Vestn. Leningr. Univ. **22**, 55 (1974).
[21] S. P. Belov, G. Y. Golubiatnikov, A. V. Lapinov, E. A. Ilyushin, V. V. Alekseev, A. A. Mescheryakov, J. T. Hougen, and L.-H. Xu, J. Chem. Phys. **145**, 024307 (2016).
[22] J. Hougen, I. Kleiner, and M. Godefroid, J. Mol. Spectrosc. **163**, 559 (1994).
[23] C. C. Lin and J. D. Swalen, Rev. Mod. Phys. **31**, 841 (1959).
[24] L.-H. Xu, J. Fisher, R. M. Lees, H. Y. Shi, J. T. Hougen, J. C. Pearson, B. J. Drouin, G. A. Blake, and R. Braakman, J. Mol. Spectrosc. **251**, 305 (2008).
[25] J. Stanton, J. Gauss, M. E. Harding, and P. Szalay, CFOUR, coupled-cluster techniques for computational chemistry, http://www.cfour.de.
[26] D. M. Brink and G. R. Satchler, *Angular Momentum*, 3rd ed. (Clarendon, Oxford, 1993).
[27] J. D. Jackson, *Classical Electrodynamics*, 3rd ed. (Wiley, New York, 1998).
[28] H. Longuet-Higgins, Mol. Phys. **6**, 445 (1963).
[29] P. R. Bunker and P. Jensen, *Molecular Symmetry and Spectroscopy* (NRC Research Press, 1998).
[30] B. Kirtman, J. Chem. Phys. **37**, 2516 (1962).
[31] R. M. Lees and J. G. Baker, J. Chem. Phys. **48**, 5299 (1968).
[32] E. Herbst, J. Messer, F. C. D. Lucia, and P. Helminger, J. Mol. Spectrosc. **108**, 42 (1984).
[33] T. H. Dunning, Jr., J. Chem. Phys. **90**, 1007 (1989).
[34] J. T. Hougen, J. Chem. Phys. **57**, 4207 (1972).
[35] L. H. Coudert, W. Caminati, M. Schnell, and J.-U. Grabow, J. Mol. Spectrosc. **242**, 118 (2007).
[36] M. Tudorie, L. H. Coudert, T. R. Huet, D. Jegouso, and G. Sedes, J. Chem. Phys. **134**, 074314 (2011).
[37] J. T. Hougen, private communication (2016).
[38] D. S. Bernstein, *Matrix Mathematics: Theory, Facts, and Formulas* (Princeton University Press, 2009).
[39] J. R. Eshbach and M. W. P. Strandberg, Phys. Rev. **85**, 24 (1952).
[40] I. C. Bowater, J. M. Brown, and A. Carrington, Proc. R. Soc. A **333**, 265 (1973).
[41] K. Blum, *Density Matrix Theory and Applications, Physics of Atoms and Molecules* (Plenum, New York, 1981).
[42] L. C. Biedenharn, J. D. Louck, and P. A. Carruthers, *Angular Momentum in Quantum Physics: Theory and Application* (Addison-Wesley Reading, MA, 1981).

nature astronomy

LETTERS

https://doi.org/10.1038/s41550-017-0341-8

Characterization of methanol as a magnetic field tracer in star-forming regions

Boy Lankhaar[1*], Wouter Vlemmings[1], Gabriele Surcis[2,3], Huib Jan van Langevelde[2,4], Gerrit C. Groenenboom[5] and Ad van der Avoird[5]

Magnetic fields play an important role during star formation[1]. Direct magnetic field strength observations have proven particularly challenging in the extremely dynamic protostellar phase[2–4]. Because of their occurrence in the densest parts of star-forming regions, masers, through polarization observations, are the main source of magnetic field strength and morphology measurements around protostars[2]. Of all maser species, methanol is one of the strongest and most abundant tracers of gas around high-mass protostellar disks and in outflows. However, as experimental determination of the magnetic characteristics of methanol has remained largely unsuccessful[5], a robust magnetic field strength analysis of these regions could hitherto not be performed. Here, we report a quantitative theoretical model of the magnetic properties of methanol, including the complicated hyperfine structure that results from its internal rotation[6]. We show that the large range in values of the Landé *g* factors of the hyperfine components of each maser line lead to conclusions that differ substantially from the current interpretation based on a single effective *g* factor. These conclusions are more consistent with other observations[7,8] and confirm the presence of dynamically important magnetic fields around protostars. Additionally, our calculations show that (nonlinear) Zeeman effects must be taken into account to further enhance the accuracy of cosmological electron-to-proton mass ratio determinations using methanol[9–12].

The presence of a magnetic field within an astrophysical maser produces partially polarized radiation. Linear polarization provides information on the magnetic field direction, while the magnetic field strength can be determined by comparing the field-induced frequency shifts between left- and right-circularly polarized maser emission. Extraction of the relevant information from polarized maser spectra requires knowledge of the Zeeman parameters that describe the response of the maser molecule/atom to a magnetic field. These Zeeman parameters are known for maser molecules such as hydroxide (OH), water and silicon monoxide, but not for methanol (CH_3OH).

Various torsion–rotation transitions of methanol have been observed as astrophysical masers. It has long been known that these transitions have a hyperfine structure, but only recently has an accurate model of this structure been presented[6]. It was shown that the so-called torsional motion of methanol about the carbon–oxygen (C–O) bond drastically complicates the hyperfine interactions and that 'spin–torsion' terms occur in addition to the usual 'spin–rotation' and spin–spin coupling terms. The magnetic moments that produce the hyperfine structure also interact with an external magnetic field, that is, a Zeeman effect. Here, we extend the model of methanol's hyperfine structure with the Zeeman interactions. We quantitatively determine all of the relevant coupling parameters, including effects from the torsional motion, by quantum chemical ab initio calculations and an estimate of the torsional Zeeman effect based on experimental results[13]. With this model, we can determine the Zeeman splitting of the hyperfine states within all the known methanol maser transitions. Zeeman interactions are usually described in a first-order approximation by the Landé *g* factor. In methanol, each torsion–rotation transition is actually split into a number of transitions between individual hyperfine levels of the upper and lower torsion–rotation states (Fig. 1). The Landé *g* factors calculated for the different hyperfine transitions differ strongly, and although these transitions cannot be individually resolved in the observed maser spectra, we show that this is important for the interpretation of the measured polarization effects. Furthermore, we find that, in several cases, the energy gaps between hyperfine levels are so small that hyperfine states with different total angular momenta *F* get mixed even by a weak magnetic field. In such cases, the first-order approximation for the Zeeman interactions breaks down, and the Zeeman splittings depend nonlinearly on the magnetic field strength (Fig. 2). Also, the Einstein *A* coefficients of transitions between two hyperfine levels become magnetic-field-dependent quantities in these cases (Supplementary Fig. 2). This behaviour has not previously been seen in Zeeman interactions for non-paramagnetic molecules, and is therefore not accounted for in current maser polarization theory[14,15].

To apply our results to maser polarization measurements, we must consider hyperfine-specific effects in the maser action. The individual hyperfine lines are not spectrally resolved, but the maser action can favour specific hyperfine transitions by the following mechanisms: (1) varying radiative rates for stimulated emission (see the Einstein coefficients of the various hyperfine components within a torsion–rotation line (Supplementary Information)); (2) kinematic effects, when there are two maser clouds along the line of sight with different velocities, such that a hyperfine transition in the foreground cloud amplifies emission from a different hyperfine transition in the background cloud[16]; (3) population inversion of the levels involved in maser action is preceded by collisional and radiative de-excitation of higher torsion–rotation levels[17], with rate coefficients that are hyperfine-state specific[18]. The last effect has been overlooked in current maser excitation models[17], and thus no quantitative information is available. To obtain a qualitative understanding, we consider the relative hyperfine-specific collisional and

[1]Department of Space, Earth and Environment, Onsala Space Observatory, Chalmers University of Technology, Onsala, Sweden. [2]Joint Institute for VLBI ERIC, Dwingeloo, Netherlands. [3]INAF, Osservatorio Astronomico di Cagliari, Selargius, Italy. [4]Sterrewacht Leiden, Leiden University, Leiden, Netherlands. [5]Theoretical Chemistry, Institute for Molecules and Materials, Radboud University, Nijmegen, Netherlands. *e-mail: boy.lankhaar@chalmers.se

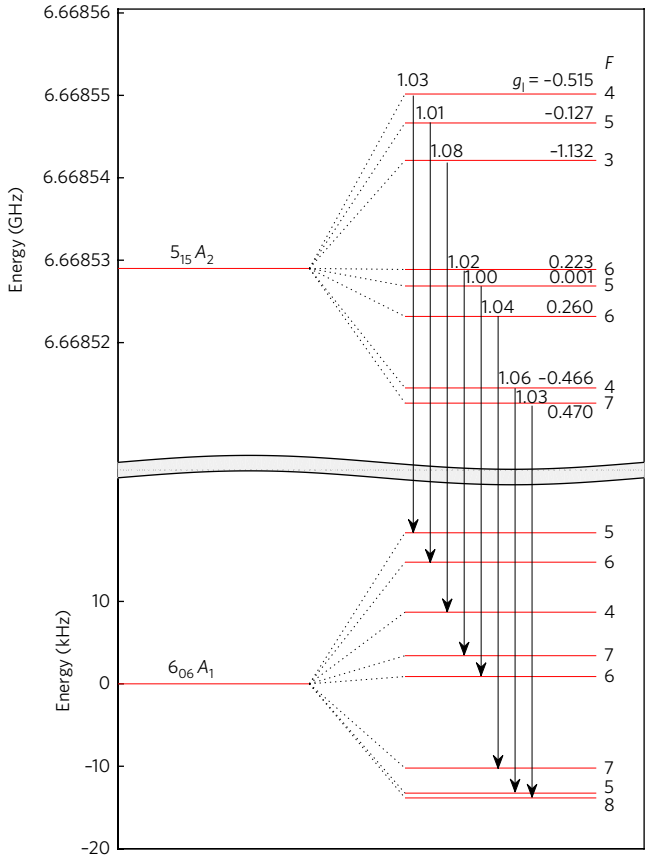

Fig. 1 | Hyperfine structure of the torsion–rotation levels in the 6.7 GHz ($5_{15}A_2 \rightarrow 6_{06}A_1$) transition. The energy of the $6_{06}A_1$ torsion–rotation level is set to zero. Because hyperfine interactions (~10 kHz) are much smaller than the torsion–rotation energy difference (~10 GHz), we have broken the *y* axis. Torsion–rotation states of *A* symmetry have nuclear spin quantum numbers $I=1$ and 2, so that for rotational states with $J \geq 2$ there are six levels with $F=J$, $J\pm1$ and two levels with $F=J\pm2$, each $2F+1$ -fold degenerate. Hence, the $F=J$, $J\pm1$ states contain both $I=1$ and $I=2$ components, which are mixed[6]. The hyperfine structure of the torsion–rotation levels is ~30 kHz wide. Arrows indicate the strongest hyperfine transitions with $\Delta F=\Delta J=1$, with the Einstein *A* coefficients (in 10^{-9} s^{-1}) indicated above. Landé *g* factors, g_I, of the transitions in a magnetic field of 10 mG are given at the right-hand side of the upper energy levels. The rightmost numbers are the *F* quantum numbers of the hyperfine states.

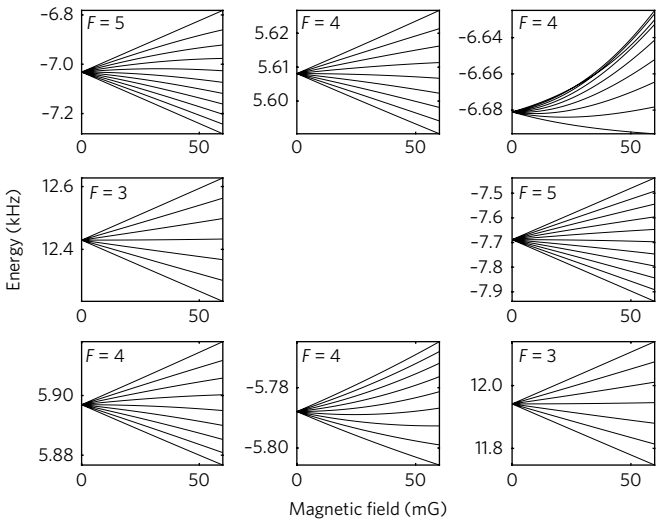

Fig. 2 | Splitting of the eight hyperfine levels of the torsion–rotation $4_{-1}E$ state as a function of the magnetic field strength. The quantum number *F* of each hyperfine level is given in the upper left-hand corner. In a magnetic field, each hyperfine level splits into $2F+1$ magnetic substates. The energy on the vertical axis is defined relative to the energy of the corresponding torsion–rotation state $4_{-1}E$.

radiative rates within a torsion–rotation transition. We find for de-excitation collisions of methanol with helium atoms (equation (8)) and for radiative emission (equation (12)) that the hyperfine levels with the highest *F* quantum number have the largest relative de-excitation rate coefficients.

Until now, methanol maser circular-polarization observations have been made for the 6.7 GHz ($5_{15}A_2 \rightarrow 6_{06}A_1$)[2,19], 44 GHz ($7_{07}A_2 \rightarrow 6_{16}A_1$)[4,20] and 36 GHz ($4_{-1}E \rightarrow 3_0E$)[3] torsion–rotation transitions. Because the magnetic characteristics of methanol were not known, (hyperfine-unspecific) estimates of the Zeeman parameters were used. In the following, we re-analyse some of the observations, using our calculated Zeeman parameters (Table 1). We take into account that within a torsion–rotation transition the various hyperfine transitions have different Landé *g* factors (Supplementary Tables 1–18) and that the maser action can be hyperfine-state specific.

We begin with the circular-polarization observations of class II methanol masers at 6.7 GHz, occurring in protostellar disks. We assume that the transition with the largest Einstein coefficient for stimulated emission, the $F=3\rightarrow4$ transition (see Fig. 1 and Supplementary Table 3), will be favoured and that the maser action is limited to this transition. Then, the Zeeman-splitting coefficient α_Z (related to the Landé *g* factor g_I as $\alpha_Z=\mu_N g_I$, with μ_N being the nuclear magneton) of the maser transition will be $\alpha_Z=-1.135\,\mathrm{Hz\,mG^{-1}}$, which is ten times larger than the value currently used for magnetic field estimates[2,5]. In the methanol maser regions probed by these class II masers, with an H_2 number density of $n_{H_2}\approx10^8\,\mathrm{cm^{-3}}$ (ref. [17]), application of our new results to a large sample of maser observations[2] indicates an average field strength $\langle|B|\rangle\approx12\,\mathrm{mG}$. If, instead of by the $F=3\rightarrow4$ hyperfine transition, the polarization is caused by a combination of hyperfine components or by any of the other components, the derived magnetic field strength would be higher. Including all hyperfine components would result in an average $\alpha_Z\approx0.17\,\mathrm{Hz\,mG^{-1}}$ and an average $\langle|B|\rangle\approx80\,\mathrm{mG}$. This is considerably larger than expected based on OH masers observed at similar densities[7,8]. The results based on the $F=3\rightarrow4$ transition are in good agreement with OH maser polarization observations[7,8] as well as with the extrapolated magnetic field versus density relation $B\propto n^{1/2}$ (refs [21,22]). This indicates, as already suggested by linear polarization studies[19,23], that methanol masers probe the large-scale magnetic field around massive protostars. Reversely, extending the magnetic field versus density relation by almost two orders of magnitude in density provides important constraints on the theory of massive star formation, because it implies that the magnetic energy density remains important up to densities of $n_{H_2}\approx10^9\,\mathrm{cm^{-3}}$. The conclusions are also supported by a more specific study of Cepheus A HW2 (ref. [23] and Fig. 3), where our reinterpretation confirms a slightly supercritical maser region, giving rise to magnetically regulated accretion towards the disk of Cepheus A HW2.

Polarization observations of class I methanol masers in the outflows of massive star-forming regions have been made for the 36 GHz and 44 GHz torsion–rotation transitions. In both lines, the individual hyperfine transitions are clustered in two groups, giving rise to a doublet structure in the spectra[6]. Considering kinematic effects favouring one of the two peaks, and selecting from this peak the transition with the largest coefficient for stimulated emission, we assume that

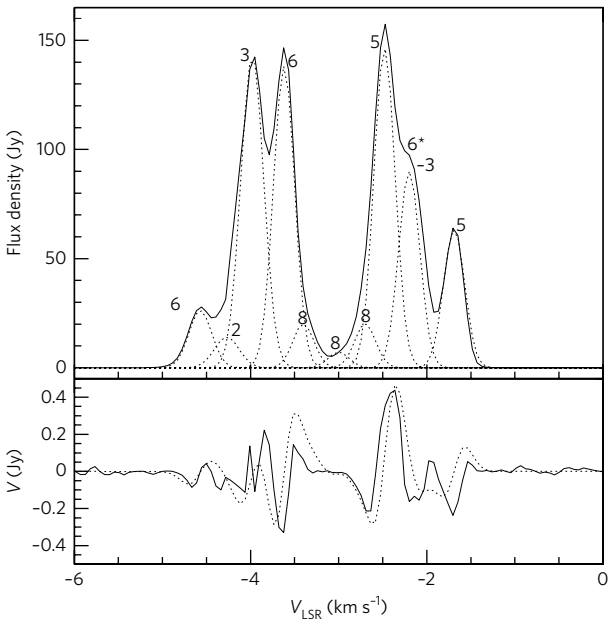

Fig. 3 | Total intensity and circular-polarization (*V*) spectra of the 6.7 GHz ($5_{15}A_2 \rightarrow 6_{06}A_1$) methanol masers around the disk of the high-mass protostar Cepheus A HW2[23]. Total intensity is flux density in Jy = 10^{-26} W m^{-2} Hz^{-1}. The velocity is defined with respect to the local standard of rest, V_{LSR}. The spectra (solid) were observed with the Effelsberg 100 m telescope. They originate from methanol masers with different velocities along the same line of sight and can be approximated by ten Gaussian peaks (dashed, total intensity). If we assume that a single hyperfine component is dominant, our calculations (dashed, circular polarization) imply an average line-of-sight magnetic field strength $B_{||} = 7.7 \pm 1.0$ mG. The field strengths (in mG) extracted from the individual components, with errors of ~20% s.d., are indicated in the figure for each Gaussian. These correspond to a total magnetic field strength of $|B| = 26$ mG. In one of the peaks, the maser radiation is oppositely polarized with respect to the other peaks, which suggests a reverse magnetic field. However, this could be due to pumping of a different hyperfine component with a different Landé *g* factor. If this argument holds, the magnetic field (denoted by the asterisk) extracted from this component has the same direction and is of similar magnitude as the fields from the other maser components. Using information on the masing gas and the mass of the region where the magnetic field is probed[23], the recalculated ratio between the thermal and magnetic energy, $\beta = 0.2$, shows the dominance of the magnetic field. The recalculated mass to magnetic flux ratio compared with the critical ratio is 1.5.

the $F = 3 \rightarrow 2$ (36 GHz) and $F = 5 \rightarrow 4$ (44 GHz) hyperfine lines are favoured and that the maser action is limited to these transitions. Then, the Zeeman-splitting coefficients of the maser transitions will be $\alpha_Z = -0.704$ Hz mG^{-1} for the 36 GHz line and $\alpha_Z = -0.920$ Hz mG^{-1} for the 44 GHz line (Supplementary Tables 10 and 4). The observed class I methanol masers are expected to occur in shocked regions of the outflows at densities of an order of magnitude lower than class II masers[24]. The Zeeman splitting of the 36 GHz and 44 GHz lines was found to be of the order of several tens of hertz[3,4,20]. Using our analysis, this would indicate magnetic field strengths of 20–75 mG. Because class I masers are shock excited, shock compression is expected to increase the magnetic field strength. For the outflow velocities in the class I maser regions, a preshock magnetic field as observed in the OH maser regions (~5 mG) will be amplified to >20 mG, consistent with the observations. We thus suggest that class I methanol maser polarization observations provide important information on the shock conditions of protostellar outflows.

Our results also suggest an explanation for a surprising feature observed in both class II (6.7 GHz) and class I (44 GHz) masers. Observations have shown reversals in the sign of polarization over areas of small angular extent in the sky (fig. 3 (6.7 GHz) and fig. 2 (44 GHz) in ref. [20]). Such reversals have usually been interpreted as a change in field direction. However, reversals on AU-scales would be surprising if one considers the agreement between the fields probed by methanol masers and dust emission[25]. A more plausible explanation favoured by our results is that in the masers with opposite signs of polarization, the masing process itself is due to the dominance of different hyperfine transitions. If we assume for the 6.7 GHz spectrum that for the oppositely polarized maser the $F = 7 \rightarrow 8$ hyperfine transition is favoured by kinematic effects, instead of the $F = 3 \rightarrow 4$ transition for the other masers, we find a magnetic field comparable to the result from other masers along the line of sight (Fig. 3). For the 44 GHz maser, if we assume the $F = 8 \rightarrow 7$ transition to be favoured for the oppositely polarized maser instead of the $F = 5 \rightarrow 4$ transition for the other maser, we also get Zeeman-splitting coefficients with opposite signs, and we find similar magnetic fields of ~50 mG from both masers composing the signal. We thus find that an alternative preferred hyperfine transition in the maser action is able to explain opposite circular polarization along the line of sight, and we obtain magnetic fields comparable to the results from other masers that trace similar areas around the protostar.

Our model is also important for the study of methanol maser absorption in red-shifted cosmological sources. Methanol's high sensitivity to variation of the electron-to-proton mass ratio in the torsion–rotational structure is enhanced by its torsional motion[11]. Extragalactic absorption measurements of the $3{-}1E \rightarrow 20E$ (12.2 GHz) transition have been used to provide the strongest constraints on the time variation of the electron-to-proton mass ratio[9,10]. Recently, measurements with a high spatial resolution have been able to selectively observe methanol absorption in an extragalactic cold core[26]. Hyperfine effects shift the centre of torsion–rotation lines, which is an effect not accounted for in the current torsion–rotation fitting Hamiltonian[27] from which the parameters are used in determination of the sensitivity coefficients[11,28]. Also, in cold extragalactic regions, temperature broadening effects are smaller than the hyperfine splittings, which could be resolved with a sufficiently high spectral resolution. Furthermore, in regions with strong magnetic fields (>30 mG), this structure will be affected by Zeeman effects. These effects should be included in the error-accounting of the constraints to the time variation of the electron-to-proton mass ratio[12].

Theoretical modelling of (nonlinear) Zeeman effects for other molecular species such as hydrogen cyanide (HCN) and formaldehyde (H_2CO) can also be done according to the theory presented here. The same care should be taken in the assessment of Zeeman effects in radical species, where the magnetic field can mix fine-structure states, which is analogous to hyperfine mixing. This will be particularly important for thioxoethenylidene (CCS)[29,30], for which the Zeeman characteristics are still poorly known, but which will be one of the prime molecules for Zeeman studies with the Square Kilometre Array.

Methods

We theoretically modelled the response of methanol to weak magnetic fields by the addition of magnetic field (Zeeman) interactions to the model for methanol's hyperfine structure from Lankhaar et al.[6]. Here, we briefly revisit methanol's hyperfine structure and describe the relevant Zeeman interactions. Next, we detail the computational methods used to obtain the molecule-specific coupling parameters. Finally, we describe the methods used to compute the magnetic-field-dependent spectrum of methanol.

Hyperfine structure. The elucidation of methanol's hyperfine structure has been a challenge. The CH_3 group in methanol can easily rotate with respect to the OH group, which leads to an extension of the usual rigid-rotor hyperfine Hamiltonian with nuclear spin–torsion interactions[31]. In contrast with the nuclear spin–rotation

Table 1 | Zeeman-splitting parameters α_z for the strongest $\Delta F = \Delta J$ transitions of the investigated maser lines

Transition	α_z (Hz mG^{-1})							
	$F=J-2$	$F=J-1$		$F=J$		$F=J+1$		$F=J+2$
$5_{15}A_2 \rightarrow 6_{06}A_1$ (6.7 GHz)	−1.135	−0.516	−0.467	−0.127	0.002	0.224	0.261	0.472
$7_{07}A_2 \rightarrow 6_{16}A_1$ (44 GHz)	−0.920	−0.436	−0.403	−0.016	−0.108	0.207	0.203	0.413
$4_{-1}E \rightarrow 3_0E$ (36 GHz)		−0.704		−0.075	0.056	0.424		
		−0.729		−0.274	0.174	0.486		

The ranges of the quantum number F for states of A symmetry are explained in the caption of Fig. 1. Torsion–rotation states of the E symmetry state have nuclear spin $I=0$ and 1, so that for $J \geq 1$ there are hyperfine states with $F=J$ and $F=J\pm1$. Each torsion–rotation function of E symmetry yields two sets of hyperfine states of overall symmetry A_1 and A_2 (ref. [6]). The hyperfine lines for each $J \rightarrow J'$ torsion–rotation transition are indicated by their initial F value, relative to the corresponding J value. For A symmetry, a single transition is associated with each $F=J\pm2$ and two transitions with each $F=J$, $J\pm1$. For E symmetry, two transitions $A_1 \rightarrow A_2$ and $A_2 \rightarrow A_1$ are associated with each $F=J\pm1$ and four transitions with $F=J$.

coupling parameters, for which the ab initio calculated values have recently been experimentally confirmed[32], the torsional hyperfine coupling parameters cannot be obtained from quantum chemical ab initio calculations[6,33]. Experiments probing the hyperfine structure of methanol have proven difficult to interpret, because the hyperfine transitions cannot be individually resolved. Lankhaar et al.[6] revised the derivation of a Hamiltonian that includes the torsional hyperfine interactions, and obtained the coupling parameters in this Hamiltonian from both ab initio calculations and experimental data[31,33]. The hyperfine spectra of methanol calculated from this Hamiltonian agree well with the spectra observed for several torsion–rotation states of both A symmetry and E symmetry. In our present calculations of the Zeeman interactions of methanol in external magnetic fields, we start from this hyperfine Hamiltonian. For a detailed description, see Lankhaar et al.[6].

Zeeman Hamiltonian. Zeeman interactions are governed by the same magnetic moments that determine the hyperfine structure, interacting with an external magnetic field $\mathbf{B}$. For a closed-shell diamagnetic molecule such as methanol, three contributions are important: the overall rotation term, the internal rotation term or torsional term and the nuclear spin term. The most abundant ^{12}C and ^{16}O nuclei have spin zero, so the nuclear spin of methanol (CH_3OH) comes from the three protons in the CH_3 group and the proton in the OH group. As derived in appendix A of Lankhaar et al.[6] for the corresponding hyperfine Hamiltonian, the rotational Zeeman Hamiltonian

$$\hat{H}_{\mathrm{BR}} = -\frac{\mu_{\mathrm{N}}}{\hbar}\mathbf{B}\cdot\mathbf{g}(\gamma)\hat{\mathbf{J}} + \frac{\mu_{\mathrm{N}}}{\hbar}f\mathbf{B}\cdot\mathbf{g}(\gamma)\boldsymbol{\lambda}\,(\hat{p}_\gamma - \boldsymbol{\rho}\cdot\hat{\mathbf{J}}) \tag{1}$$

depends not only on the overall rotation angular momentum $\hat{\mathbf{J}}$, but also on the torsional angular momentum $\hat{p}_\gamma = (\hbar/i)\partial/\partial\gamma$, where $\hbar$ is Planck's constant divided by 2π and i is the imaginary number. The coupling tensor $\mathbf{g}$ has the same form as for rigid molecules, but for molecules with internal rotation, it depends on the torsional angle γ. The unit vector $\boldsymbol{\lambda}$ describes the direction of the internal rotation axis in the principal-axes frame of the molecule, and $\boldsymbol{\rho} = \mathbf{I}^{-1}\mathbf{I}^{\mathrm{CH_3}}\boldsymbol{\lambda}$, where $\mathbf{I}$ is the total inertia tensor and $\mathbf{I}^{\mathrm{CH_3}}$ is the inertia tensor of the CH_3 group. The dimensionless factor f depends on the ratio of the moments of inertia of the OH frame and the rotating CH_3 top about the torsional axis[6].

In addition, we must account for torsional Zeeman effects. Similarly to the torsional hyperfine Hamiltonian $\hat{H}_{\mathrm{ST}}$ in Lankhaar et al.[6], the torsional Zeeman Hamiltonian

$$\hat{H}_{\mathrm{BT}} = -\frac{\mu_{\mathrm{N}}}{\hbar}f\mathbf{B}\cdot\mathbf{b}(\gamma)\,(\hat{p}_\gamma - \boldsymbol{\rho}\cdot\hat{\mathbf{J}}) \tag{2}$$

with the coupling vector $\mathbf{b}(\gamma)$, not only contains the torsional angular momentum operator $\hat{p}_\gamma$, but also the total angular momentum $\hat{\mathbf{J}}$. By absorbing the second term of equation (1) into equation (2), the remaining rotational Zeeman Hamiltonian obtains the usual form it has for a rigid molecule, and we obtain an effective $\hat{H}_{\mathrm{BT}}$, with $\mathbf{b}(\gamma)$ replaced by

$$\mathbf{b}'(\gamma) = \mathbf{b}(\gamma) - \mathbf{g}(\gamma)\boldsymbol{\lambda} \tag{3}$$

Finally, the intrinsic magnetic moments of the protons $K=1,2,3$ in the CH_3 group and proton $K=4$ in the OH group interact with the magnetic field as

$$\hat{H}_{\mathrm{BS}} = -\frac{\mu_{\mathrm{N}}}{\hbar}g_{\mathrm{p}}\sum_K \mathbf{B}\cdot\hat{\mathbf{I}}_K \tag{4}$$

where g_{p} is the proton g factor. The total Zeeman Hamiltonian is a sum of the rotational, torsional and nuclear spin Zeeman terms

$$\hat{H}_{\mathrm{Zeeman}} = \hat{H}_{\mathrm{BR}} + \hat{H}_{\mathrm{BT}} + \hat{H}_{\mathrm{BS}} \tag{5}$$

Coupling tensors. The response of methanol to magnetic fields is theoretically modelled by including the coupling of the relevant angular momenta—the rotational angular momentum, the torsional momentum and the nuclear spin angular momentum—to the magnetic field vector. The couplings between these angular momentum operators and the magnetic field involve a rank-2 coupling tensor and a coupling vector. This coupling tensor and vector are specific for methanol. The derivation of the hyperfine coupling tensors is given in Lankhaar et al.[6], and that of the Zeeman coupling tensors is in the Supplementary Information. In the following, we describe the methods used to evaluate all coupling parameters.

Rotational g tensor. Rotational Zeeman effects are represented by the molecule-specific g tensor, which for rigid non-paramagnetic molecules has been extensively studied experimentally for its valuable information on the electronic structure[34–37]. Nowadays, quantum chemical calculations[38,39] are able to reproduce these experiments with high accuracy. The rotational g tensor $\mathbf{g}(\gamma)$ can be obtained from ab initio electronic structure calculations with the program package CFOUR[40]. We carried out calculations with CFOUR at the coupled-cluster level of theory including single and double excitations with perturbative addition of the triples contribution (CCSD(T)), in an augmented triple-zeta correlation-consistent (aug-cc-pVTZ) basis set[41]. The geometry of methanol was optimized at this level, which yields OH, CO and CH bond lengths of 0.956 Å, 1.427 Å and 1.096 Å, respectively, COH and OCH bond angles of 108.87° and 109.91°, respectively, and an HOCH torsional angle of 180°. The electronic contributions to $\mathbf{g}(\gamma)$ were calculated at the same level of theory for 13 equidistant values of γ by fixing the HOC fragment and rotating the CH_3 group over these angles about the OC bond axis. The nuclear contribution to $\mathbf{g}(\gamma)$ was also given by CFOUR, but was also calculated directly from the nuclear coordinates. Because of methanol's symmetry, we could fit our ab initio calculated values for the rotational $\mathbf{g}(\gamma)$-tensor elements to either $\sum_n a_{3n}cos(3n\gamma)$ or $\sum_n a_{3n}sin(3n\gamma)$ functions of the internal rotation angle. The expansion coefficients, a_{3n}, are listed in Supplementary Table 1.

Torsional b-vector. Torsional Zeeman interactions are represented by the molecule-specific b-vector (Supplementary equations (16) and (21)). The calculation of the electronic contribution to the b-vector has not been implemented in the available quantum chemical program packages. To estimate the torsional Zeeman effects in methanol, we compare its internally rotating CH_3 group with the CH_3 groups of nitromethane and methyl-boron-difluoride, of which the torsional Zeeman effect has been investigated experimentally[13,42].

The torsional Zeeman coupling vectors of nitromethane and methyl-boron-difluoride were determined to be $\mathbf{b} = g_\gamma\boldsymbol{\lambda}$, with $g_\gamma = 0.347$ and 0.3415, respectively. In these molecules, the unit vector $\boldsymbol{\lambda}$ that defines the direction of the internal rotation axis lies along the main principal axis. The small difference in the g values of these two molecules is explained by the electron drainage from the CH_3 groups by the attached functional group (see Supplementary Information). This electron drainage can be estimated from the partial atomic charges given by a Mulliken population analysis[43]. We calculated Mulliken populations, P, of the CH_3 groups of nitromethane and methyl-boron-difluoride at the CCSD(T) level in an augmented double-zeta correlation consistent (aug-cc-pVDZ) basis, at their ab initio optimized geometries, and found these to be $P_{\mathrm{CH_3(-NO_2)}} = 8.714$ and $P_{\mathrm{CH_3(-BF_2)}} = 9.232$, respectively. We computed the Mulliken population of the CH_3 group in methanol at the same level and found this to be $P_{\mathrm{CH_3(-OH)}} = 8.737$. Then, we obtained the b-vector of methanol by interpolation as $\mathbf{b} = g_\gamma\boldsymbol{\lambda}$, with $g_\gamma = 0.3468$ (see Supplementary Table 1). In this estimate of $\mathbf{b}$, we have assumed that it is independent of the torsional angle γ and is parallel to $\boldsymbol{\lambda}$. The latter assumption holds only when $\boldsymbol{\lambda}$ is directed along one of the principal axes, which is almost the case for methanol[6,27].

Matrix elements and spectrum. With the knowledge of the coupling tensors $\mathbf{g}(\gamma)$ and $\mathbf{b}(\gamma)$ in the Zeeman Hamiltonian of equation (5) and the use of the hyperfine Hamiltonian from Lankhaar et al.[6], we computed the magnetic field dependence of the hyperfine levels. The total Hamiltonian is diagonalized in the basis $|\{(I_{123}, I_4)I, J\}FM_F\rangle$, obtained by coupling the eigenfunctions of the torsion–rotation Hamiltonian[27] with the nuclear spin functions $|(I_{123}, I_4)I\rangle$ of the appropriate symmetry, defined in section IIC of Lankhaar et al.[6]. The hyperfine interactions couple the total nuclear spin I with the torsion–rotation angular momentum J to a total (hyperfine) angular momentum F, with projection M_F on the space-fixed z axis chosen along the magnetic field direction. When the external magnetic field is included, only M_F remains a good quantum number. Hyperfine states with different F may get mixed, which occurs to a substantial extent when there is a small energy gap between the hyperfine levels.

The torsion–rotation wave functions[27] have symmetry A or E and quantum numbers v_τ, J and K_a, where v_τ is the torsional quantum number and K_a the projection of $\mathbf{J}$ on the principal a-axis. For symmetries A and E, the nuclear spin basis has $I_{123} = 3/2$ and $1/2$, respectively (see section IIC in Lankhaar et al.[6]). The energy gaps between torsion–rotation states are typically of the order of a few gigahertz, whereas the hyperfine and Zeeman interactions in methanol (for fields $B < 10$ G) amount to about 10 kHz. Hence, we may restrict our basis to a single value of v_τ and J and derive an effective Zeeman Hamiltonian of which the matrix elements are more easily evaluated (Supplementary Information).

The matrix of the total Zeeman plus hyperfine Hamiltonian over the hyperfine basis with quantum numbers F and M_F was evaluated and diagonalized. This yielded the splitting of the hyperfine levels into $2F+1$ sublevels, with M_F as the only good quantum number. Intensities and Einstein A coefficients for transitions between the individual hyperfine levels were obtained with the procedures described in Lankhaar et al.[6].

Hyperfine-state resolved de-excitation. We emphasize in this letter that the Landé g factors of the different hyperfine components of each torsion–rotation transition vary over a large range of values. It is therefore important to know the populations of the individual hyperfine levels of the torsion–rotation states involved in the methanol maser action. This maser action is preceded by collisional and radiative de-excitation of higher torsion–rotation levels. Here, we derive formulas to estimate relative hyperfine-state-specific collisional and radiational de-excitation rate coefficients.

Hyperfine-state resolved collisional rate coefficients. Hyperfine splittings are negligible with respect to the collision energy, so to an excellent approximation the collision dynamics depends only on the scattering conditions and on the torsion–rotation structure of the molecule, and is not affected by hyperfine effects[18,44]. As a consequence, obtaining hyperfine-state-specific $F \rightarrow F'$ transition rate coefficients from the usual rate coefficients for rotationally inelastic $J \rightarrow J'$ collisions requires only the use of an appropriate basis in which the angular momentum J is coupled with the total nuclear spin I to total angular momentum F (refs [18,45]).

Davis[46] analysed the collision dynamics of a structureless atom (such as helium) and a molecule with one internal rotation (such as methanol), using a simple torsion–rotation model and neglecting the molecule's vibrational modes. The presence of the torsional modes leads to additional inelastic scattering processes, but the angular momentum algebra in the expressions for the scattering amplitudes and cross-sections are similar for collisions with methanol and with diatomic molecules. The methanol symmetric rotor quantum number K_a and torsional quantum numbers v_τ and σ play only a spectator role with regard to the angular momentum (re-)coupling[46].

Performing coupled-channel calculations for collisions of methanol with helium in a hyperfine basis would exceed the scope of this letter. Rather, we want to get an idea of the general trends of the hyperfine inelastic scattering rates with respect to the corresponding rotational rates. To this end, we use a formalism that relates the torsion–rotation inelastic scattering cross-sections to hyperfine-state-specific cross-sections. This is most conveniently done by representing the cross-sections in terms of tensor opacities[44,46]

$$\sigma_{(K_a\sigma v_\tau)J\rightarrow(K_a'\sigma' v_\tau')J'} = \frac{\pi}{[J]k^2_{(K_a\sigma v_\tau)J}} \sum_L P^{(L)}((K_a\sigma v_\tau)J \rightarrow (K_a'\sigma' v_\tau')J') \tag{6}$$

for a transition from initial state $|(K_a\sigma v_\tau)J\rangle$ to a final state $|(K_a'\sigma' v_\tau')J'\rangle$, where $k_{(K_a\sigma v_\tau)J}$ is the wave vector dependent on the collision energy and the torsion–rotation energy of the initial state, L is the rank of the tensor opacity $P^{(L)}$, and the square bracket notation designates $[J] = 2J+1$. Recoupling the nuclear-spin-free opacity to the hyperfine-state-specific opacity yields[44]

$$\begin{aligned} &P^{(L)}((K_a\sigma v_\tau)[JI]F \rightarrow (K_a'\sigma' v_\tau')[J'I]F') \\ &= [F][F'] \begin{Bmatrix} J & J' & L \\ F' & F & I \end{Bmatrix}^2 P^{(L)}((K_a\sigma v_\tau)J \rightarrow (K_a'\sigma' v_\tau')J') \end{aligned} \tag{7}$$

The expression in curly brackets is a 6j-symbol. Substitution of this result into equation (6) yields the hyperfine-state-specific collisional cross-sections

$$\begin{aligned} \sigma_{(K_a\sigma v_\tau)[JI]F\rightarrow(K_a'\sigma' v_\tau')(J'I)F'} &= \frac{\pi}{k^2_{(K_a\sigma v_\tau)J}[F]} \times \\ &\sum_L P^{(L)}((K_a\sigma v_\tau)[JI]F \rightarrow (K_a'\sigma' v_\tau')[J'I]F') \\ &= \frac{\pi[F']}{k^2_{(K_a\sigma v_\tau)J}} \times \\ &\sum_L \begin{Bmatrix} J & J' & L \\ F' & F & I \end{Bmatrix}^2 P^{(L)}((K_a\sigma v_\tau)J \rightarrow (K_a'\sigma' v_\tau')J') \end{aligned}$$

The triangular condition imposes the constraint $|J-J'| \le L \le J+J'$. Each of these values of L contributes to the total hyperfine-state-specific collisional rates. Except for very low collision energies where resonances may occur, which are not important under the methanol maser conditions, the largest contribution comes from $L = |\Delta J|$. Considering this contribution only would directly relate the hyperfine-state-specific rate with the rotational rate[45]

$$\sigma_{(K_a\sigma v_\tau)[JI]F\rightarrow(K_a'\sigma' v_\tau')[J'I]F'} = [J][F'] \begin{Bmatrix} J' & J & |\Delta J| \\ F & F' & I \end{Bmatrix}^2 \sigma_{(K_a\sigma v_\tau)J\rightarrow(K_a'\sigma' v_\tau')J'} \tag{9}$$

To analyse which final hyperfine levels, F', are mostly populated by (de-) excitation, we must sum equation (9) over all initial hyperfine states F. Then, we find, for example, for the collisional de-excitation $J = 6 \rightarrow J' = 5$ that the $F' = J'+2$ state has a 14% higher propensity to be populated than the $F' = J'-2$ state. The other hyperfine states with $F' = J'$ and $J' \pm 1$ are linear combinations of two nuclear spin states, and have population propensities lower than the $F' = J'+2$ state and higher than the $F' = J'-2$ state.

Actually, one can also analyse the ratio between hyperfine rates including all L channels with equation (8), and find that hyperfine-state-specific collision propensities for the $F' = J'+2$ state are even higher for the other L channels. We can therefore say that the hyperfine collisional de-excitation propensity is over 14% higher for the $F' = J'+2$ state than for the $F' = J'-2$ state. Hyperfine-state-specific collision rate propensities of intermediate F' states are somewhere between the two extremes. More generally, we find consistently that in collisional (de-)excitation, for $\Delta J < 0$ transitions, high F' states have a higher propensity for every L channel. In $\Delta J = 0$ transitions, there is no hyperfine preference, and in $\Delta J > 0$ transitions, low F' hyperfine states have the highest probability to be populated.

Hyperfine-state resolved radiative rates. To investigate which hyperfine transitions are favoured by radiative de-excitation, we recouple the line strength of a torsion–rotation transition to a hyperfine basis. From the line strength, one can easily compute the Einstein coefficient.

The line strength of a transition between torsion–rotation states $(K_a\sigma v_\tau)J$ and $(K_a'\sigma' v_\tau')J'$ is

$$S_{(K_a\sigma v_\tau)J\rightarrow(K_a'\sigma' v_\tau')J'} = \sum_{MM'} |\langle (K_a\sigma v_\tau)JM| \, \mathbf{d} \, |(K_a'\sigma' v_\tau')J'M'\rangle|^2 \tag{10}$$

where $\mathbf{d}$ stands for the total dipole moment vector of all charged particles, electrons and nuclei. In recoupling the rotational line strength to hyperfine-state-specific line strengths, we recognize that the line strength transforms as a rank-1 tensor opacity, and we use equation (7) to obtain

$$S_{(K_a\sigma v_\tau)[JI]F\rightarrow(K_a'\sigma' v_\tau')[J'I]F'} = [F][F'] \begin{Bmatrix} J' & J & 1 \\ F & F' & I \end{Bmatrix}^2 S_{(K_a\sigma v_\tau)J\rightarrow(K_a'\sigma' v_\tau')J'} \tag{11}$$

The Einstein A coefficient is related to the line strength by

$$A_{(K_a\sigma v_\tau)[JI]F\rightarrow(K_a'\sigma' v_\tau')[J'I]F'} = \frac{2\omega^3}{3\varepsilon_0 hc^3[F]} S_{(K_a\sigma v_\tau)[JI]F\rightarrow(K_a'\sigma' v_\tau')[J'I]F'} \tag{12}$$

where ε_0, h and c are the vacuum permittivity, Planck's constant and the speed of light, respectively; ω is the transition frequency, which to a very good approximation does not depend on the hyperfine splittings of the rotational states.

To analyse which final hyperfine levels F' are mostly populated by (de-) excitation, we must sum equation (9) over all initial hyperfine states F: $A_{(K_a\sigma v_\tau)J\rightarrow(K_a'\sigma' v_\tau')[J'I]F'}$. Then, we find for a $J = 6 \rightarrow J' = 5$ emission, for example, that the ratio between the Einstein coefficients for de-excitation to the final hyperfine states with $F' = J'+2$ and $F' = J'-2$ is

$$\frac{A_{(K_a\sigma v_\tau)6\rightarrow(K_a'\sigma' v_\tau')[5I]7}}{A_{(K_a\sigma v_\tau)6\rightarrow(K_a'\sigma' v_\tau')[5I]3}} = 1.14 \tag{13}$$

The intermediate hyperfine states with $F' = J'$ and $J' \pm 1$ are linear combinations of two nuclear spin states, and have population propensities lower than the $F' = J' + 2$ state and higher than the $F' = J' - 2$ state. The ratio calculated in equation (13) increases exponentially for lower J. For rotational states with higher J, it decreases to 1.

Data availability. The data that support the plots within this paper and other findings of this study are available from the corresponding author upon reasonable request.

Received: 8 June 2017; Accepted: 13 November 2017;
Published online: 29 January 2018

References

1. Crutcher, R. M. Magnetic fields in molecular clouds. *Annu. Rev. Astron. Astrophys.* **50**, 29–63 (2012).
2. Vlemmings, W. H. T., Torres, R. M. & Dodson, R. Zeeman splitting of 6.7 GHz methanol masers. *Astron. Astrophys.* **529**, A95 (2011).
3. Sarma, A. & Momjian, E. Detection of the Zeeman effect in the 36 GHz class I CH_3OH maser line with the EVLA. *Astrophys. J. Lett.* **705**, L176 (2009).
4. Sarma, A. & Momjian, E. Discovery of the Zeeman effect in the 44 GHz class I methanol (CH_3OH) maser line. *Astrophys. J. Lett.* **730**, L5 (2011).
5. Jen, C. K. Rotational magnetic moments in polyatomic molecules. *Phys. Rev.* **81**, 197–203 (1951).
6. Lankhaar, B., Groenenboom, G. C. & van der Avoird, A. Hyperfine interactions and internal rotation in methanol. *J. Chem. Phys.* **145**, 244301 (2016).
7. Baudry, A. & Diamond, P. VLBA polarization observations of the J = 7/2, 13.44 GHz OH maser in W3 (OH). *Astron. Astrophys.* **331**, 697–708 (1998).
8. Wright, M. M., Gray, M. D. & Diamond, P. J. The OH ground-state masers in W3(OH) II. Polarization and multifrequency results. *Mon. Not. R. Astron. Soc.* **350**, 1272–1287 (2004).
9. Bagdonaite, J. et al. A stringent limit on a drifting proton-to-electron mass ratio from alcohol in the early universe. *Science* **339**, 46–48 (2013).
10. Kanekar, N. et al. Constraints on changes in the proton-electron mass ratio using methanol lines. *Mon. Not. R. Astron. Soc.* **448**, L104–L108 (2015).
11. Jansen, P., Xu, L.-H., Kleiner, I., Ubachs, W. & Bethlem, H. L. Methanol as a sensitive probe for spatial and temporal variations of the proton-to-electron mass ratio. *Phys. Rev. Lett.* **106**, 100801 (2011).
12. Daprà, M. et al. Testing the variability of the proton-to-electron mass ratio from observations of methanol in the dark cloud core L1498. *Mon. Not. R. Astron. Soc.* **472**, 4434–4443 (2017).
13. Engelbrecht, L. *Der Rotations-Zeemaneffekt bei Molekülen mit schwach behinderter interner Rotation*. PhD thesis, Univ. Kiel (1975).
14. Deguchi, S. & Watson, W. D. Linearly polarized radiation from astrophysical masers due to magnetic fields when the rate for stimulated emission exceeds the Zeeman frequency. *Astrophys. J.* **354**, 649–659 (1990).
15. Vlemmings, W. H. T., Diamond, P. J., van Langevelde, H. J. & Torrelles, J. M. The magnetic field in the star-forming region Cepheus A. from H_2O maser polarization observations. *Astron. Astrophys.* **448**, 597–611 (2006).
16. Walker, R. H_2O in W49N. II-Statistical studies of hyperfine structure, clustering, and velocity distributions. *Astrophys. J.* **280**, 618–628 (1984).
17. Cragg, D., Sobolev, A. & Godfrey, P. Models of class II methanol masers based on improved molecular data. *Mon. Not. R. Astron. Soc.* **360**, 533–545 (2005).
18. Corey, G. & McCourt, F. R. Inelastic differential and integral cross sections for $^{2S+1}\sigma$ linear molecule-^{1}S atom scattering: the use of Hund's case b representation. *J. Phys. Chem.* **87**, 2723–2730 (1983).
19. Surcis, G., Vlemmings, W. H. T., van Langevelde, H. J. & Hutawarakorn Kramer, B. EVN observations of 6.7 GHz methanol maser polarization in massive star-forming regions. *Astron. Astrophys.* **541**, A47 (2012).
20. Momjian, E. & Sarma, A. The Zeeman effect in the 44 GHz class I methanol maser line toward DR21 (OH). *Astrophys. J.* **834**, 168 (2017).
21. Crutcher, R. M. Magnetic fields in molecular clouds: observations confront theory. *Astrophys. J.* **520**, 706–713 (1999).
22. Vlemmings, W. H. T. A new probe of magnetic fields during high-mass star formation. *Astron. Astrophys.* **484**, 773–781 (2008).
23. Vlemmings, W., Surcis, G., Torstensson, K. & Van Langevelde, H. Magnetic field regulated infall on the disc around the massive protostar Cepheus A HW2. *Mon. Not. R. Astron. Soc.* **404**, 134–143 (2010).
24. Voronkov, M. A. et al. Class I methanol masers in the outflow of IRAS 16 547–4247. *Mon. Not. R. Astron. Soc.* **373**, 411–424 (2006).
25. Dall'Olio, D. et al. Methanol masers reveal the magnetic field of the high-mass protostar IRAS 18089-1732. *Astron. Astrophys.* **607**, A111 (2017).
26. Marshall, M. A. et al. Methanol absorption in PKS B1830-211 at milliarcsecond scales. *Mon. Not. R. Astron. Soc.* **466**, 2450–2457 (2017).
27. Xu, L.-H. et al. Torsion–rotation global analysis of the first three torsional states (v_t = 0, 1, 2) and terahertz database for methanol. *J. Mol. Spectr.* **251**, 305–313 (2008).
28. Jansen, P., Kleiner, I., Xu, L.-H., Ubachs, W. & Bethlem, H. L. Sensitivity of transitions in internal rotor molecules to a possible variation of the proton-to-electron mass ratio. *Phys. Rev. A.* **84**, 062505 (2011).
29. Shinnaga, H. & Yamamoto, S. Zeeman effect on the rotational levels of CCS and SO in the $^3\sigma$-ground state. *Astrophys. J.* **544**, 330 (2000).
30. Ramos, A. A. & Bueno, J. T. Theory and modeling of the Zeeman and Paschen-Back effects in molecular lines. *Astrophys. J.* **636**, 548–563 (2006).
31. Heuvel, J. & Dymanus, A. Hyperfine structure of CH_3OH. *J. Mol. Spectrosc.* **45**, 282–292 (1973).
32. Belov, S. P. et al. Torsionally mediated spin-rotation hyperfine splittings at moderate to high J values in methanol. *J. Chem. Phys.* **145**, 024307 (2016).
33. Coudert, L., Gutlé, C., Huet, T., Grabow, J.-U. & Levshakov, S. Spin-torsion effects in the hyperfine structure of methanol. *J. Chem. Phys.* **143**, 044304 (2015).
34. Eshbach, J. R. & Strandberg, M. W. P. Rotational magnetic moments of closed shell molecules. *Phys. Rev.* **85**, 24–34 (1952).
35. Flygare, W. & Benson, R. The molecular Zeeman effect in diamagnetic molecules and the determination of molecular magnetic moments (g values), magnetic susceptibilities, and molecular quadrupole moments. *Mol. Phys.* **20**, 225–250 (1971).
36. Sutter, D. & Flygare, W. in *Bonding Structure* Vol. 63 (eds Craig, D. et al.) 89–196 (Topics in Current Chemistry series, Springer, Berlin, 1976).
37. Flygare, W. Magnetic interactions in molecules and an analysis of molecular electronic charge distribution from magnetic parameters. *Chem. Rev.* **74**, 653–687 (1974).
38. Gauss, J., Ruud, K. & Helgaker, T. Perturbation-dependent atomic orbitals for the calculation of spin-rotation constants and rotational g-tensors. *J. Chem. Phys.* **105**, 2804–2812 (1996).
39. Lutnaes, O. B. et al. Benchmarking density-functional-theory calculations of rotational g tensors and magnetizabilities using accurate coupled-cluster calculations. *J. Chem. Phys.* **131**, 144104 (2009).
40. Stanton, J., Gauss, J., M.E., Harding & Szalay, P. *CFOUR, Coupled-Cluster Techniques for Computational Chemistry*; http://www.cfour.de.
41. Dunning, T. H. Jr Gaussian basis sets for use in correlated molecular calculations. I. The atoms boron through neon and hydrogen. *J. Chem. Phys.* **90**, 1007–1023 (1989).
42. Engelbrecht, L., Sutter, D. & Dreizier, H. Zeeman effect of molecules with low methyl barriers. I. Nitromethane. *Z. Naturforsch. A* **28**, 709–713 (1973).
43. Mulliken, R. S. Electronic population analysis on LCAO-MO molecular wave functions. I. *J. Chem. Phys.* **23**, 1833–1840 (1955).
44. Alexander, M. H. & Dagdigian, P. J. Collision-induced transitions between molecular hyperfine levels: quantum formalism, propensity rules, and experimental study of CaBr ($X\ ^2\sigma_+$) + Ar. *J. Chem. Phys.* **83**, 2191–2200 (1985).
45. Neufeld, D. A. & Green, S. Excitation of interstellar hydrogen chloride. *Astrophys. J.* **432**, 158–166 (1994).
46. Davis, S. L. Torsionally inelastic collisions between a near-symmetric top molecule and a structureless atom. *J. Chem. Phys.* **95**, 7219–7225 (1991).

Acknowledgements

Support for this work was provided by the Swedish Research Council (VR), and by the European Research Council under the European Union's Seventh Framework Programme (FP7/2007-2013), through the European Research Council consolidator grant agreement no. 614264.

Author contributions

B.L., A.v.d.A. and W.V. wrote the paper. B.L., A.v.d.A. and G.C.G. modelled the Zeeman effect in methanol. B.L. and W.V. performed the analysis of the astrophysical maser spectra, based on methanol's Zeeman model. W.V., H.J.v.L. and G.S. provided expertise on maser polarization in astrophysics and initiated the project. All authors discussed the results and commented on the manuscript.

Competing interests

The authors declare no competing financial interests.

Additional information

Supplementary information is available for this paper at https://doi.org/10.1038/s41550-017-0341-8.

Reprints and permissions information is available at www.nature.com/reprints.

Correspondence and requests for materials should be addressed to B.L.

Publisher's note: Springer Nature remains neutral with regard to jurisdictional claims in published maps and institutional affiliations.

nature astronomy

SUPPLEMENTARY INFORMATION

https://doi.org/10.1038/s41550-017-0341-8

In the format provided by the authors and unedited.

Characterization of methanol as a magnetic field tracer in star-forming regions

Boy Lankhaar[1]*, Wouter Vlemmings[1], Gabriele Surcis[2,3], Huib Jan van Langevelde[2,4], Gerrit C. Groenenboom[5] and Ad van der Avoird[5]

[1]Department of Space, Earth and Environment, Onsala Space Observatory, Chalmers University of Technology, Onsala, Sweden. [2]Joint Institute for VLBI ERIC, Dwingeloo, Netherlands. [3]INAF, Osservatorio Astronomico di Cagliari, Selargius, Italy. [4]Sterrewacht Leiden, Leiden University, Leiden, Netherlands. [5]Theoretical Chemistry, Institute for Molecules and Materials, Radboud University, Nijmegen, Netherlands. *e-mail: boy.lankhaar@chalmers.se

Supplementary: Characterization of methanol as a magnetic field tracer in star-forming regions

Boy Lankhaar and Wouter Vlemmings

Department of Space, Earth and Environment,

Chalmers University of Technology,

*Onsala Space Observatory, 439 92 Onsala, Sweden**

Gabriele Surcis

Joint Institute for VLBI ERIC, Postbus 2,

7990 AA Dwingeloo, The Netherlands and

INAF, Osservatorio Astronomico di Cagliari Via della Scienza 5, I-09047 Selargius, Italy

Huib Jan van Langevelde

Joint Institute for VLBI ERIC, Postbus 2,

7990 AA Dwingeloo, The Netherlands and

Sterrewacht Leiden, Leiden University,

Postbus 9513, 2330 RA Leiden, the Netherlands

Gerrit C. Groenenboom and Ad van der Avoird

Theoretical Chemistry, Institute for Molecules and Materials,

Radboud University, Heyendaalseweg 135,

6525 AJ Nijmegen, The Netherlands

(Dated: October 25, 2017)

* lankhaar@chalmers.se

NON-LINEAR ZEEMAN EFFECTS

Figure 2 in the paper shows the non-linear Zeeman effects in methanol that prevail already at low magnetic fields. Here, we will discuss the origins of these non-linear effects and their consequences for the description of the Zeeman parameters of methanol.

The Zeeman shift of a maser line emitted in a magnetic field B is defined as half the difference between the energies where the right- and left-circularly polarized radiation have their maximum intensities: $\Delta E(B) = [E_{\rm rcp}(B) - E_{\rm lcp}(B)]/2$, and the g-factor is

$$g(B) = -\frac{\Delta E(B)}{\mu_N B}, \tag{1}$$

where μ_N is the nuclear magneton. Usually the Zeeman shifts depend linearly on B and the Landé g-factors are constant. Supplementary Figure 1 shows the g-factors of the different hyperfine components of the 6.7 GHz (5_{15} $A_2 \rightarrow 6_{06}$ A_1) and 36 GHz (4_{-1} $E \rightarrow 3_0$ E) methanol maser transitions over a magnetic field range from 0 to 60 mG. It is clear from this figure that for several hyperfine-state resolved transitions the g-factors are not constant. Especially for the 36 GHz transition in panel (b) of the figure, we observe a strong magnetic field dependence of the g-factors for two of the hyperfine lines: for one of them it varies by more than a factor of three. We also observe in this figure that there is a large variation among the g-values of different hyperfine transitions, with both positive and negative signs occurring.

These non-linear Zeeman shifts are caused by mixing of the hyperfine states. This happens in particular when the energy gap between hyperfine levels is of the same order of magnitude as their Zeeman shifts in the external magnetic field. The most striking case, which produces the strongest magnetic field dependence of the g-values in panel (b) of Supplementary Figure 1, is a mixing of the $F = 4$ and $F = 5$ levels of the 4_{-1} E state, which are only 0.34 kHz apart. Also in other cases the energy gaps between hyperfine levels are as small as about 2 kHz and there is substantial mixing of hyperfine levels with $\Delta F = 1$. It will be clear that F is no longer a good quantum number in such cases.

Since particular hyperfine levels are mixed by the external magnetic field, the nature of the transition between such levels changes with the magnetic field as well. Supplementary Figure 2 illustrates the influence of the magnetic field on the Einstein A-coefficients of the 6.7 GHz (5_{15} $A_2 \rightarrow 6_{06}$ A_1) and 36 GHz (4_{-1} $E \rightarrow 3_0$ E) transitions. For all hyperfine

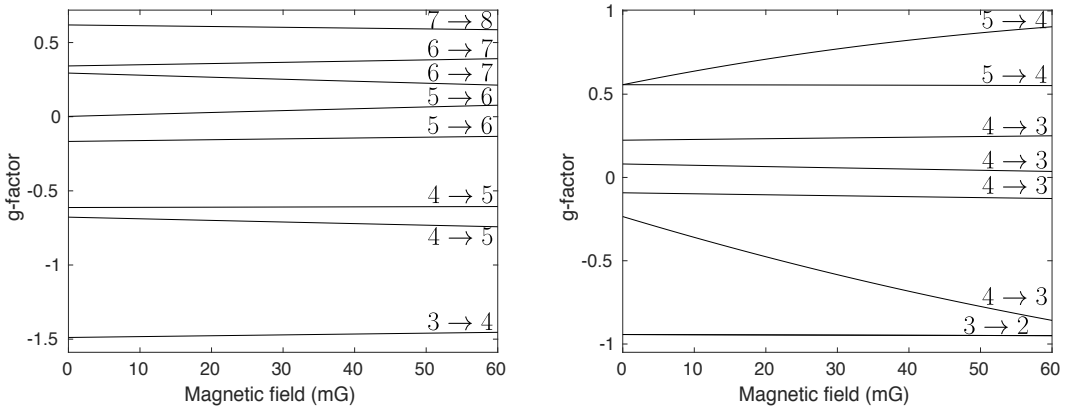

(a) (b)

Supplementary Figure 1: Magnetic field dependence of the g-factors of the strongest hyperfine transitions within the 6.7 GHz ($5_{15}\ A_2 \rightarrow 6_{06}\ A_1$) (a) and 36 GHz ($4_{-1}\ E \rightarrow 3_0\ E$) (b) methanol maser lines. The different components are labeled $F \rightarrow F'$ with their initial and final F values, which are good quantum numbers for $B = 0$.

components of both torsion-rotation transitions, we observe a significant magnetic field dependence of the A-coefficients.

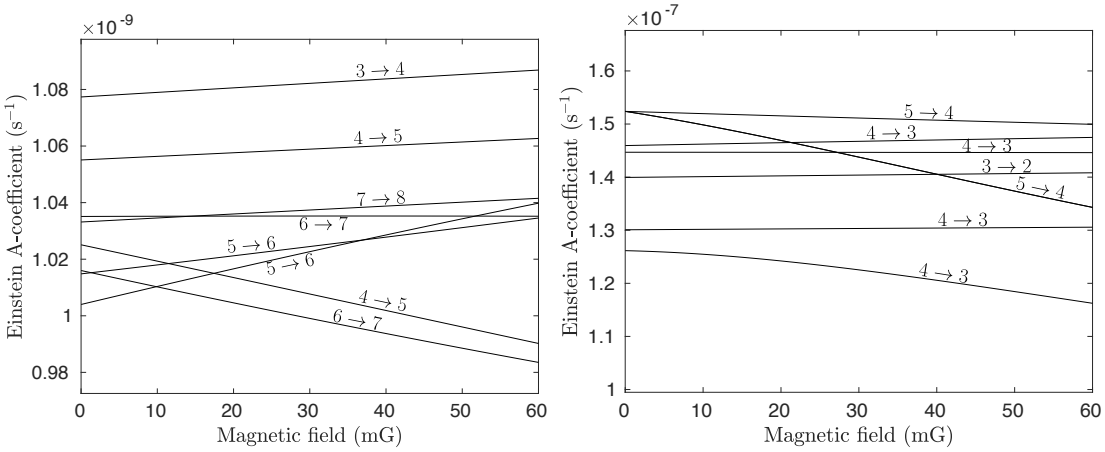

(a) (b)

Supplementary Figure 2: Magnetic field dependence of the Einstein A-coefficients of the strongest hyperfine transitions within the 6.7 GHz ($5_{15}\ A_2 \rightarrow 6_{06}\ A_1$) (a) and 36 GHz ($4_{-1}\ E \rightarrow 3_0\ E$) (b) methanol maser lines

ROTATIONAL AND TORSIONAL ZEEMAN EFFECTS

The method section of the paper describes the formalism that we used to compute the Zeeman effects in methanol. Here, we present a rigorous derivation of this formalism.

Molecules consist of charged particles, nuclei and electrons, and their rotation produces a magnetic dipole moment. For molecules with internal rotation, such as methanol, an additional magnetic dipole moment originates from their torsional motion. These magnetic moments, interacting with the nuclear spins, are involved in the molecules' hyperfine structure. The derivation of the appropriate hyperfine Hamiltonian was described by Lankhaar *et al.*[1]. Here, we derive the corresponding Zeeman Hamiltonian for the interaction of the rotational and torsional magnetic moments with external magnetic fields. We refer to Appendix A of Ref. [1] for most of the theoretical background.

As usual for molecules with internal rotation, we distinguish two parts of the molecule that are internally rigid. The "frame" part consists of those atoms that remain fixed in the molecule-fixed (MF) principal axis frame, in the case of methanol the OH fragment. The origin of the MF frame is the center of mass of the CH_3OH molecule and its orientation with respect to a space-fixed (SF) frame is defined by three Euler angles (χ, θ, ϕ). The "top" part is fixed with respect to a frame TF that rotates with respect to the MF frame about

a single (fixed) axis $\boldsymbol{\lambda}$ over an angle γ. This "top" is considered to be a symmetric rotor, such as the CH_3 group in methanol.

The magnetic moment of methanol, $\boldsymbol{m}$, is determined by all the moving charged particles[2]

$$\boldsymbol{m} = \frac{1}{2}\sum_i Q_i(\boldsymbol{r}_i \times \boldsymbol{v}_i), \tag{2}$$

where $\boldsymbol{r}_i$, Q_i and $\boldsymbol{v}_i$ are the position, charge, and velocity of particle i. Electrons have $Q_i = -e$ and nuclei have charge $Z_i e$ with Z_i given by their atomic number. The energy of this magnetic moment in a (homogeneous) external magnetic field $\boldsymbol{B}$ is

$$H = -\boldsymbol{B}\cdot\boldsymbol{m} = -\sum_i \frac{Q_i}{2}\boldsymbol{B}\cdot(\boldsymbol{r}_i \times \boldsymbol{v}_i), \tag{3}$$

In this summation we can distinguish between particles in the "frame" and particles in the "top", of which the positions are fixed with respect to the MF and TF frame, respectively. Their positions with respect to the SF frame are given by equation (A1) of Ref. [1], and in equation (A3) of Ref. [1] their velocities are expressed in terms of the angular velocity $\boldsymbol{\omega}$ of the whole molecule and the velocity $\dot{\gamma}$ of rotation of the "top" about the axis $\boldsymbol{\lambda}$ relative to the "frame". Substitution of these expressions into Supplementary equation (3) yields

$$H^{\text{frame}} = -\boldsymbol{B}\cdot\boldsymbol{V}^{\text{frame}}\boldsymbol{\omega}, \tag{4}$$

for particles in the "frame", with

$$\boldsymbol{V}^{\text{frame}} = \sum_i^{\text{frame}} \frac{Q_i}{2}[(\boldsymbol{r}_i^{\text{MF}}\cdot\boldsymbol{r}_i^{\text{MF}})\mathbf{1} - \boldsymbol{r}_i^{\text{MF}}\otimes\boldsymbol{r}_i^{\text{MF}}] \tag{5}$$

For particles in the "top" we obtain

$$H^{\text{top}} = -\boldsymbol{B}\cdot\boldsymbol{V}^{\text{top}}\boldsymbol{\omega}' - \boldsymbol{B}\cdot\boldsymbol{v}\dot{\gamma}, \tag{6}$$

with

$$\boldsymbol{V}^{\text{top}} = \sum_i^{\text{top}} \frac{Q_i}{2}[(\boldsymbol{r}_i^{\text{TF}}\cdot\boldsymbol{r}_i^{\text{TF}})\mathbf{1} - \boldsymbol{r}_i^{\text{TF}}\otimes\boldsymbol{r}_i^{\text{TF}}], \tag{7}$$

and

$$\boldsymbol{v} = \sum_i^{\text{top}} \frac{Q_i}{2}[(\boldsymbol{r}_i^{\text{TF}}\cdot\boldsymbol{r}_i^{\text{TF}})\mathbf{1} - \boldsymbol{r}_i^{\text{TF}}\otimes\boldsymbol{r}_i^{\text{TF}}]\boldsymbol{\lambda}. \tag{8}$$

The angular velocity $\boldsymbol{\omega}'$ with respect to the TF frame is related to $\boldsymbol{\omega}$ defined in the MF frame as $\boldsymbol{\omega}' = \boldsymbol{R}(\boldsymbol{\lambda},\gamma)\boldsymbol{\omega}$, where $\boldsymbol{R}(\boldsymbol{\lambda},\gamma)$ represents the rotation over γ about axis $\boldsymbol{\lambda}$. All

tensor and vector components in Supplementary equations (6), (7), and (8) are defined in the TF frame, while Supplementary equations (4) and (5) are written in the MF frame. We prefer to write all equations in the MF frame, i.e., the principal axes frame of the whole molecule. This can be achieved by transformation to the γ dependent coupling tensor $\boldsymbol{V}^{\mathrm{top}}(\gamma) = \boldsymbol{R}(\boldsymbol{\lambda},\gamma)^{-1}\boldsymbol{V}^{\mathrm{top}}\boldsymbol{R}(\boldsymbol{\lambda},\gamma)$ and coupling vector $\boldsymbol{v}(\gamma) = \boldsymbol{R}(\boldsymbol{\lambda},\gamma)^{-1}\boldsymbol{v}$. Supplementary equation (6) then becomes

$$H^{\mathrm{top}} = -\boldsymbol{B}\cdot\boldsymbol{V}^{\mathrm{top}}(\gamma)\boldsymbol{\omega} - \boldsymbol{B}\cdot\boldsymbol{v}(\gamma)\dot{\gamma}, \tag{9}$$

in which also the components of $\boldsymbol{B}$ and $\boldsymbol{\omega}$ are given in the MF frame. Since all tensors and vectors are now given in the MF frame, we may add Supplementary equations (4) and (9) to obtain

$$H = -\boldsymbol{B}\cdot\boldsymbol{V}(\gamma)\boldsymbol{\omega} - \boldsymbol{B}\cdot\boldsymbol{v}(\gamma)\dot{\gamma}, \tag{10}$$

with

$$\begin{aligned}\boldsymbol{V}(\gamma) &= \boldsymbol{V}^{\mathrm{frame}} + \boldsymbol{V}^{\mathrm{top}}(\gamma)\\ &= \sum_i \frac{Q_i}{2}\left[(\boldsymbol{r}_i^{\mathrm{MF}}\cdot\boldsymbol{r}_i^{\mathrm{MF}})\mathbf{1} - \boldsymbol{r}_i^{\mathrm{MF}}\otimes\boldsymbol{r}_i^{\mathrm{MF}}\right],\end{aligned} \tag{11}$$

where the sum over particles i now runs over all electrons and nuclei in the whole molecule. We note that the positions $\boldsymbol{r}_i^{\mathrm{MF}}$ of particles in the top depend on the internal rotation angle γ.

Next we replace the angular velocities $\boldsymbol{\omega}$ and $\dot{\gamma}$ in Supplementary equation (10) by their conjugate angular momenta $\boldsymbol{J}$ and p_γ, with the use of equation (A7) from Ref. [1]. The quantum mechanical equivalent is then obtained by replacing the angular momenta $\boldsymbol{J}$ and p_γ by the corresponding operators $\hat{\boldsymbol{J}}$ and $(\hbar/i)\partial/\partial\gamma$. This yields $H \to \hat{H} = \hat{H}_{\mathrm{BR}} + \hat{H}_{\mathrm{BT}}$, with the rotational and torsional Zeeman Hamiltonians $\hat{H}_{\mathrm{BR}}$ and $\hat{H}_{\mathrm{BT}}$ given in equations (1) and (2) in the Methods section of the paper. The coupling tensors are defined as

$$\boldsymbol{g}(\gamma) = \frac{\hbar}{\mu_N}\boldsymbol{V}(\gamma)\boldsymbol{I}^{-1} \tag{12}$$

and

$$\boldsymbol{b}(\gamma) = \frac{\hbar}{\mu_N}\boldsymbol{v}(\gamma)I_\gamma^{-1}, \tag{13}$$

where I_γ is the moment of inertia of the "top" about the rotation axis $\boldsymbol{\lambda}$ and $\boldsymbol{I}$ the inertia tensor of the whole molecule, which is diagonal in the principal axes frame MF.

Finally we note that the coupling tensors given in Supplementary equations (8) and (11) depend on the coordinates of both nuclei and electrons. The contributions that contain the nuclear coordinates can be directly calculated, since the positions of the nuclei are fixed with respect to the MF frame (for the nuclei in the "frame") or depend only on the torsion angle γ (for the nuclei in the "top"). For the rotational Zeeman coupling tensor $\boldsymbol{g}$ it was shown that the electronic contributions can be obtained by second order perturbation theory [3] with matrix elements over the molecule's ground state and excited electronic wave functions. Calculation of this rotational Zeeman tensor has been implemented in the electronic structure program package CFOUR[4], and it can thus be computed as a function of γ. No such implementation yet exists, however, for the torsional Zeeman coupling vector $\boldsymbol{b}$. A procedure to estimate this b-vector with the use of experimental data[5] is described in the paper.

Supplementary Table 1: Coefficients a_n in the Fourier expansion describing the torsional angle γ dependence of the rotational g-tensor calculated *ab initio*. The (γ-independent) components of the torsion-magnetic field coupling vector $\boldsymbol{b}(\gamma)$ have been estimated from experimental data, see text. The components of $\boldsymbol{g}(\gamma)$ and $\boldsymbol{b}(\gamma)$ are defined with respect to the principal axes $\boldsymbol{a}$, $\boldsymbol{b}$, and $\boldsymbol{c}$ of methanol. Terms in the Fourier series are $\cos n\gamma$ or $\sin n\gamma$, depending on whether a component is symmetric (+) or antisymmetric (−) with respect to a sign change of γ.

	Symmetry	a_0	a_3	a_6
g_{aa}	+	0.325	0.0165	4.86×10^{-5}
g_{bb}	+	−0.056	−0.0014	1.04×10^{-5}
g_{cc}	+	−0.033	-1.25×10^{-3}	7.0×10^{-6}
g_{ab}	+	0.139	−0.019	2.04×10^{-5}
g_{ba}	+	0.027	-3.65×10^{-3}	4.0×10^{-6}
g_{ac}	−	0	0.014	3.15×10^{-5}
g_{ca}	−	0	2.69×10^{-3}	5.8×10^{-6}
g_{bc}	−	0	2.97×10^{-4}	-7.0×10^{-6}
g_{cb}	−	0	2.87×10^{-4}	-6.8×10^{-6}
b_a	+	0.346	0	0
b_b	+	0.019	0	0
b_c	−	0	0	0

EFFECTIVE ZEEMAN HAMILTONIAN

It is mentioned in the paper that in order to obtain the magnetic field dependent spectrum of methanol we needed to compute the matrix elements of the Zeeman Hamiltonian. The evaluation of these matrix elements can be considerably simplified by the use of an *effective* Zeeman Hamiltonian similar to the effective hyperfine Hamiltonian in Ref. [1]. Since in methanol the energy gaps between torsion-rotation states are typically larger than the hyperfine and Zeeman splittings by several orders of magnitude, we may restrict the basis to a single value of the torsional and rotational quantum numbers v_τ and J. In analogy with the expressions for the hyperfine interactions in Section III.B.3 of Ref. [1] and basing

ourselves on the literature[6–9], we can then derive an effective Zeeman Hamiltonian that gives exactly the same matrix elements as the Zeeman Hamiltonian in equation (5) of the paper. This effective Zeeman Hamiltonian reads

$$\hat{H}_{\text{Zeeman}} = -\frac{\mu_N}{\hbar} g_p \sum_K \boldsymbol{B} \cdot \hat{\boldsymbol{I}}_K - \frac{\mu_N}{\hbar} \left(\hat{g}_{\text{BR}} + \hat{g}_{\text{BT}}\right) (\boldsymbol{B} \cdot \hat{\boldsymbol{J}}). \tag{14}$$

The advantage of this factorization is that the scalar product operators $\hat{\boldsymbol{B}} \cdot \hat{\boldsymbol{I}}_K$ and $\hat{\boldsymbol{B}} \cdot \hat{\boldsymbol{J}}$ are invariant under rotation, which we used to express them in terms of the space-fixed (SF) components of the operators. Matrix elements over the SF basis $|\{(I_{123}, I_4)I, J\}FM_F\rangle$ are thus more easily evaluated. The operators

$$\hat{g}_{\text{BR}} = \frac{1}{2J(J+1)} \hat{\boldsymbol{J}} \cdot \boldsymbol{g}(\gamma) \hat{\boldsymbol{J}} + \text{hermitian conjugate}$$

$$\hat{g}_{\text{BT}} = \frac{f}{2J(J+1)} \hat{\boldsymbol{J}} \cdot \boldsymbol{b}'(\gamma) \left(\hat{p}_\gamma - \boldsymbol{\rho} \cdot \hat{\boldsymbol{J}}\right) + \text{hermitian conjugate}, \tag{15}$$

contain the body-fixed components of $\hat{\boldsymbol{J}}$ with respect to the MF frame[1], and also the tensors $\boldsymbol{g}(\gamma)$ and $\boldsymbol{b}'(\gamma)$ are given with respect to this frame. Matrix elements of the operators $\hat{g}_{\text{BR}}$ and $\hat{g}_{\text{BT}}$ over the torsion-rotation eigenfunctions are simply scalar values: the g-factors belonging to a certain torsion-rotation level.

CHARACTERISTICS OF METHANOL'S MASER TRANSITIONS

In the following Supplementary Tables 2-18 below we summarize the relevant parameters for the individual hyperfine transitions in all known methanol maser lines. For the strongest hyperfine components with $\Delta F = F_{\rm down} - F_{\rm up} = \Delta J$, we list the following parameters: the hyperfine frequency shift ΔE relative to the frequency of the corresponding torsion-rotation transition, the Landé g-factors g_l at 10 mG which are dimensionless, and the Zeeman-splitting coefficients, $\alpha_Z = \mu_N g_l$ in Hz mG^{-1} and in m s^{-1}G^{-1} ($c\alpha_Z/f$). The constants μ_N, c, and f are the nuclear magneton, the speed of light (in m/s), and the frequency of the transition (in Hz). In the last column we report the Einstein A-coefficients of the hyperfine transitions in zero magnetic field.

Supplementary Table 2: 107 GHz (3_{13} $A_2 \rightarrow 4_{04}$ A_1)

$F_{\rm up}$	$F_{\rm down}$	ΔE (kHz)	g_l	α_Z(Hz mG^{-1})	α_Z(m s^{-1}G^{-1})	A (10^{-8} s^{-1})
5	6	3.059	0.844	0.644	1.803	380.097
4	5	−6.620	0.727	0.554	1.553	351.726
4	5	5.151	0.218	0.166	0.465	327.388
3	4	−2.873	−0.297	−0.226	−0.633	357.762
3	4	3.639	0.125	0.095	0.267	350.923
2	3	−0.999	−0.903	−0.688	−1.929	391.419
2	3	−2.968	−1.140	−0.869	−2.434	361.512
1	2	−6.894	−2.893	−2.205	−6.177	413.509

Supplementary Table 3: 6.7 GHz (5_{15} $A_2 \rightarrow 6_{06}$ A_1)

$F_{\rm up}$	$F_{\rm down}$	ΔE (kHz)	g_l	α_Z(Hz mG^{-1})	α_Z(m s^{-1}G^{-1})	A (10^{-8} s^{-1})
7	8	2.500	0.619	0.472	21.176	0.103
6	7	−4.397	0.342	0.261	11.716	0.104
6	7	3.541	0.294	0.224	10.067	0.102
5	6	−2.889	−0.167	−0.127	−5.712	0.101
5	6	3.015	0.002	0.002	0.070	0.100
4	5	1.240	−0.612	−0.467	−20.963	0.106
4	5	−2.835	−0.677	−0.516	−23.187	0.103
3	4	−4.417	−1.489	−1.135	−50.955	0.108

Supplementary Table 4: 44 GHz (7_{07} $A_2 \rightarrow 6_{16}$ A_1)

$F_{\rm up}$	$F_{\rm down}$	ΔE (kHz)	g_l	α_Z(Hz mG^{-1})	α_Z(m s^{-1}G^{-1})	A (10^{-8} s^{-1})
9	8	−2.444	0.542	0.413	2.811	27.449
8	7	3.934	0.267	0.203	1.383	27.116
8	7	−3.216	0.272	0.207	1.409	26.796
7	6	2.897	−0.142	−0.108	−0.736	26.285
7	6	−2.897	−0.022	−0.016	−0.112	26.078
6	5	−1.684	−0.529	−0.403	−2.745	26.407
6	5	2.863	−0.572	−0.436	−2.966	25.874
5	4	3.998	−1.207	−0.920	−6.260	25.913

Supplementary Table 5: 95 GHz ($8_{08}\ A_1 \rightarrow 7_{17}\ A_2$)

$F_{\rm up}$	$F_{\rm down}$	ΔE (kHz)	g_l	α_Z(Hz mG^{-1})	α_Z(m s^{-1}G^{-1})	A (10^{-8} s^{-1})
10	9	−2.464	0.480	0.366	1.153	286.937
9	8	3.666	0.207	0.158	0.497	283.586
9	8	−3.047	0.254	0.194	0.611	281.444
8	7	2.941	−0.126	−0.096	−0.304	277.656
8	7	−2.864	−0.037	−0.028	−0.088	276.014
7	6	−2.002	−0.468	−0.357	−1.125	278.775
7	6	2.929	−0.499	−0.380	−1.197	274.546
6	5	3.788	−1.019	−0.777	−2.448	275.165

Supplementary Table 6: 104 GHz ($11_{-1}\ E \rightarrow 10_{-2}\ E$)

$F_{\rm up}$	$F_{\rm down}$	ΔE (kHz)	g_l	α_Z(Hz mG^{-1})	α_Z(m s^{-1}G^{-1})	A (10^{-8} s^{-1})
12	11	−1.879	0.154	0.117	0.338	134.346
11	10	3.181	−0.087	−0.066	−0.190	133.740
11	10	−1.246	−0.073	−0.055	−0.159	133.680
10	9	1.859	−0.360	−0.275	−0.790	133.128
12	11	−3.047	0.158	0.120	0.345	134.346
11	10	1.915	−0.086	−0.065	−0.188	133.761
11	10	−1.246	−0.077	−0.059	−0.169	133.679
10	9	3.244	−0.361	−0.275	−0.792	133.128

Supplementary Table 7: 12.2 GHz ($2_0\ E \rightarrow 3_{-1}\ E$)

$F_{\rm up}$	$F_{\rm down}$	ΔE (kHz)	g_l	α_Z(Hz mG^{-1})	α_Z(m s^{-1}G^{-1})	A (10^{-8} s^{-1})
3	4	−4.965	0.714	0.544	13.401	0.737
2	3	−4.802	0.144	0.110	2.706	0.752
2	3	−1.475	−0.117	−0.089	−2.193	0.732
1	2	7.978	−1.433	−1.093	−26.897	0.803
3	4	−6.106	0.614	0.468	11.516	0.737
2	3	5.847	0.385	0.294	7.230	0.610
2	3	−1.475	−0.218	−0.166	−4.092	0.571
1	2	3.263	−1.397	−1.065	−26.221	0.803

Supplementary Table 8: 24.934 GHz ($2_2\ E \rightarrow 2_1\ E$)

$F_{\rm up}$	$F_{\rm down}$	ΔE (kHz)	g_l	α_Z(Hz mG^{-1})	α_Z(m s^{-1}G^{-1})	A (10^{-8} s^{-1})
3	3	16.247	2.072	1.579	18.987	3.553
2	2	9.941	0.261	0.199	2.390	3.479
2	2	−23.440	0.549	0.418	5.029	3.209
1	1	−18.416	−2.530	−1.929	−23.188	2.998
3	3	14.961	1.914	1.459	17.539	3.553
2	2	11.751	0.443	0.337	4.057	3.498
2	2	−23.440	0.576	0.439	5.281	3.205
1	1	−15.427	−2.556	−1.948	−23.421	2.998

Supplementary Table 9: 24.929 GHz ($3_2\ E \rightarrow 3_1\ E$)

$F_{\rm up}$	$F_{\rm down}$	ΔE (kHz)	g_l	α_Z(Hz mG^{-1})	α_Z(m s^{-1}G^{-1})	A (10^{-8} s^{-1})
4	4	8.336	1.410	1.075	12.926	4.699
3	3	8.365	0.226	0.172	2.067	4.641
3	3	−10.893	0.293	0.224	2.690	4.543
2	2	−7.813	−1.844	−1.405	−16.898	4.456
4	4	10.388	1.460	1.113	13.377	4.699
3	3	5.704	0.172	0.131	1.576	4.630
3	3	−10.893	0.280	0.213	2.565	4.541
2	2	−11.434	−1.830	−1.395	−16.776	4.456

Supplementary Table 10: 36 GHz ($4_{-1}\ E \rightarrow 3_0\ E$)

$F_{\rm up}$	$F_{\rm down}$	ΔE (kHz)	g_l	α_Z(Hz mG^{-1})	α_Z(m s^{-1}G^{-1})	A (10^{-8} s^{-1})
5	4	5.402	0.638	0.486	4.032	15.238
4	3	−4.791	0.228	0.174	1.442	13.009
4	3	−3.395	−0.359	−0.274	−2.270	12.615
3	2	−3.032	−0.944	−0.720	−5.965	13.994
5	4	4.042	0.556	0.424	3.514	15.238
4	3	4.303	0.073	0.056	0.461	14.595
4	3	−3.395	−0.098	−0.075	−0.619	14.469
3	2	−6.802	−0.924	−0.704	−5.836	13.995

Supplementary Table 11: 24.933 GHz ($4_2\ E \rightarrow 4_1\ E$)

$F_{\rm up}$	$F_{\rm down}$	ΔE (kHz)	g_l	α_Z(Hz mG^{-1})	α_Z(m s^{-1}G^{-1})	A (10^{-8} s^{-1})
5	5	6.560	1.157	0.882	10.603	5.266
4	4	2.449	0.077	0.059	0.706	5.216
4	4	−8.496	0.139	0.106	1.269	5.189
3	3	−6.955	−1.397	−1.065	−12.797	5.142
5	5	3.679	1.118	0.852	10.245	5.266
4	4	5.997	0.120	0.091	1.098	5.220
4	4	−8.496	0.150	0.114	1.371	5.190
3	3	−2.567	−1.409	−1.074	−12.908	5.142

Supplementary Table 12: 85 GHz ($5_{-1}\ E \rightarrow 4_0\ E$)

$F_{\rm up}$	$F_{\rm down}$	ΔE (kHz)	g_l	α_Z(Hz mG^{-1})	α_Z(m s^{-1}G^{-1})	A (10^{-8} s^{-1})
6	5	3.452	0.457	0.348	1.235	87.938
5	4	3.930	0.043	0.033	0.117	85.226
5	4	1.095	−0.081	−0.062	−0.220	84.935
4	3	−6.089	−0.703	−0.536	−1.902	83.595
6	5	4.919	0.514	0.392	1.389	87.937
5	4	−4.236	0.139	0.106	0.376	79.686
5	4	1.095	−0.242	−0.185	−0.655	78.343
4	3	−2.630	−0.717	−0.547	−1.939	83.595

Supplementary Table 13: 24.959 GHz ($5_2\ E \rightarrow 5_1\ E$)

$F_{\rm up}$	$F_{\rm down}$	ΔE (kHz)	g_l	α_Z(Hz mG^{-1})	α_Z(m s^{-1}G^{-1})	A (10^{-8} s^{-1})
6	6	−0.026	0.929	0.708	8.495	5.570
5	5	4.223	0.059	0.045	0.541	5.538
5	5	−1.070	0.082	0.062	0.750	5.533
4	4	1.462	−1.145	−0.873	−10.473	5.500
6	6	3.754	0.961	0.732	8.788	5.570
5	5	−0.271	0.024	0.018	0.222	5.537
5	5	−1.070	0.071	0.054	0.652	5.532
4	4	−3.784	−1.133	−0.864	−10.364	5.500

Supplementary Table 14: 25.018 GHz ($6_2\ E \rightarrow 6_1\ E$)

$F_{\rm up}$	$F_{\rm down}$	ΔE (kHz)	g_l	α_Z(Hz mG^{-1})	α_Z(m s^{-1}G^{-1})	A (10^{-8} s^{-1})
7	7	1.562	0.820	0.625	7.485	5.887
6	6	2.035	0.034	0.026	0.308	5.869
6	6	2.840	−0.006	−0.005	−0.057	5.865
5	5	−1.375	−0.955	−0.728	−8.712	5.843
7	7	−3.193	0.796	0.607	7.261	5.887
6	6	−3.232	0.045	0.034	0.407	5.869
6	6	2.840	0.020	0.015	0.184	5.865
5	5	4.817	−0.967	−0.737	−8.821	5.843

Supplementary Table 15: 25.125 GHz ($7_2\ E \rightarrow 7_1\ E$)

$F_{\rm up}$	$F_{\rm down}$	ΔE (kHz)	g_l	α_Z(Hz mG^{-1})	α_Z(m s^{-1}G^{-1})	A (10^{-8} s^{-1})
8	8	−6.018	0.698	0.532	6.343	6.085
7	7	−1.648	0.022	0.017	0.200	6.075
7	7	−4.870	−0.007	−0.005	−0.065	6.068
6	6	7.756	−0.839	−0.639	−7.618	6.055
8	8	−0.203	0.715	0.545	6.489	6.085
7	7	4.646	0.011	0.008	0.096	6.075
7	7	−4.870	−0.024	−0.019	−0.220	6.068
6	6	0.524	−0.827	−0.630	−7.507	6.055

Supplementary Table 16: 25.294 GHz ($8_2\ E \rightarrow 8_1\ E$)

$F_{\rm up}$	$F_{\rm down}$	ΔE (kHz)	g_l	α_Z(Hz mG^{-1})	α_Z(m s^{-1}G^{-1})	A (10^{-8} s^{-1})
9	9	−1.631	0.632	0.482	5.695	6.455
8	8	6.946	−0.005	−0.004	−0.044	6.448
8	8	0.893	−0.035	−0.027	−0.319	6.438
7	7	2.029	−0.730	−0.556	−6.580	6.433
9	9	−8.594	0.625	0.477	5.637	6.455
8	8	−0.466	0.007	0.006	0.065	6.448
8	8	0.893	−0.029	−0.022	−0.259	6.440
7	7	10.402	−0.743	−0.566	−6.694	6.433

Supplementary Table 17: 9.91 GHz ($9_{-1}\ E \rightarrow 8_{-2}\ E$)

$F_{\rm up}$	$F_{\rm down}$	ΔE (kHz)	g_l	α_Z(Hz mG^{-1})	α_Z(m s^{-1}G^{-1})	A (10^{-8} s^{-1})
10	9	−3.418	0.187	0.143	4.319	0.113
9	8	4.343	−0.105	−0.080	−2.416	0.112
9	8	−2.360	−0.084	−0.064	−1.933	0.112
8	7	3.809	−0.445	−0.339	−10.261	0.112
10	9	−4.433	0.193	0.147	4.452	0.113
9	8	3.679	−0.109	−0.083	−2.514	0.112
9	8	−2.360	−0.086	−0.065	−1.981	0.112
8	7	4.509	−0.445	−0.340	−10.271	0.112

Supplementary Table 18: 25.541 GHz ($9_2\ E \rightarrow 9_1\ E$)

$F_{\rm up}$	$F_{\rm down}$	ΔE (kHz)	g_l	α_Z(Hz mG^{-1})	α_Z(m s^{-1}G^{-1})	A (10^{-8} s^{-1})
10	10	−10.965	0.571	0.435	5.091	6.705
9	9	0.398	−0.003	−0.002	−0.025	6.699
9	9	−8.830	−0.049	−0.037	−0.434	6.691
8	8	12.815	−0.667	−0.509	−5.955	6.689
10	10	−2.762	0.565	0.431	5.042	6.705
9	9	9.022	−0.016	−0.012	−0.139	6.695
9	9	−8.830	−0.042	−0.032	−0.378	6.685
8	8	3.197	−0.654	−0.499	−5.838	6.689

[1] Lankhaar, B., Groenenboom, G. C. & van der Avoird, A. Hyperfine interactions and internal rotation in methanol. *J. Chem. Phys.* **145**, 244301 (2016).

[2] Jackson, J. D. *Classical electrodynamics* (Wiley, New York, 1998), third edn.

[3] Flygare, W. H. Spin-rotation interaction and magnetic shielding in molecules. *J. Chem. Phys.* **41**, 793–800 (1964).

[4] Stanton, J., Gauss, J., M.E., H. & Szalay, P. CFOUR, Coupled-Cluster techniques for Computational Chemistry. Http://www.cfour.de.

[5] Engelbrecht, L. & Sutter, D. The rotational Zeeman effect of molecules with low barrier internal rotation. II. Derivation of the effective rotorsional hamiltonian. *Z. Naturforsch. A* **33**, 1525–1545 (1978).

[6] Hougen, J. T. Reinterpretation of molecular beam hyperfine data for $^{14}NH_3$ and $^{15}NH_3$. *J. Chem. Phys.* **57**, 4207–4217 (1972).

[7] Hougen, J. T., Meerts, W. L. & Ozier, I. The use of extended permutation-inversion groups in constructing hyperfine hamiltonians for symmetric-top internal rotor molecules like H_3CSiH_3. *J. Mol. Spectrosc.* **146**, 8–48 (1991).

[8] Coudert, L. H., Caminati, W., Schnell, M. & Grabow, J.-U. Hyperfine coupling and large amplitude motions interaction in the water dimer. *J. Mol. Spectrosc.* **242**, 118–128 (2007).

[9] Tudorie, M., Coudert, L. H., Huet, T. R., Jegouso, D. & Sedes, G. Magnetic hyperfine coupling of a methyl group undergoing internal rotation: A case study of methyl formate. *J. Chem. Phys.* **134**, 074314 (2011).